Modulation of Hippocampal-Prefrontal Circuitry During Spatial Working Memory

Timothy Spellman

Submitted in partial fulfillment of the

requirements for the degree of

Doctor of Philosophy

under the Executive Committee

of the Graduate School of Arts and Sciences

COLUMBIA UNIVERSITY

2015

ABSTRACT

Modulation of Hippocampal-Prefrontal Circuitry During Spatial Working Memory

Timothy Spellman

Spatial working memory (SWM) is an essential feature of goal-directed action. Locating a resource, a threat, or even oneself within a dynamic or unfamiliar environment requires a cached representation of relevant spatial features that must be continuously updated, preserved, and applied as needed to the execution of appropriate behaviors (Baddeley and Hitch 1974).

SWM is disrupted in schizophrenia, as well as in multiple animal models of the disease. Patients with schizophrenia show impairment on tasks with both verbal and spatial working memory demands (Park and Holzman 1992, Conklin, Curtis et al. 2000) and exhibit abnormalities in neurophysiological signals that are associated with normal cognitive performance. More specifically, convergent data from diverse studies suggests that disruption of long-range functional connectivity may underlie diverse cognitive and physiological symptoms of the schizophrenia. It is therefore imperative that pathways of long-range functional connectivity that support the cognitive processes impaired in schizophrenia be identified and

characterized, so that effective interventions can be targeted to the appropriate neural structures and pathways.

Despite long-standing interest in the neurobiological underpinnings of working memory, its multiple cognitive components, distributed anatomical constituents, and distinct temporal phases have rendered its investigation elusive (Logie 1995, Miyake and Shah 1999, Andrade 2001, de Zubicaray, McMahon et al. 2001, Baddeley 2003, Klauer and Zhao 2004). Despite these challenges, an extensive body of work supports the idea that the prefrontal cortex (PFC) plays a central role in the successful execution of tasks requiring spatial working memory (Curtis and D'Esposito 2004). Moreover, the joint contribution of medial prefrontal cortex (mPFC) and hippocampus (HPC) supports successful spatial working memory in rodents (Lee and Kesner 2003, Jones and Wilson 2005, Wang and Cai 2006, Hyman, Zilli et al. 2010, Sigurdsson, Stark et al. 2010). It remains unclear, however, which phase(s) of SWM (encoding, maintenance, and/or retrieval) require the joint participation of HPC and mPFC, what behaviorally relevant information is conveyed between the two structures, and by what anatomical pathway(s) they interact.

Although HPC and mPFC share multiple second-degree anatomical connections, including via striatum, amygdala, entorhinal cortex, and midline thalamic nuclei, direct connectivity between the two structures is confined to a unidirectional projection from the Ca1/subiculum of the ventral hippocampus

(vHPC) to prelimbic (PL) and infralimbic (IL) regions of the mPFC (Jay and Witter 1991, Hoover and Vertes 2007, Oh 2014).

Cells of both vHPC and mPFC exhibit location-specific firing that could function to encode spatial cues critical to SWM (Jung, Wiener et al. 1994, Poucet, Thinus-Blanc et al. 1994, Jung, Qin et al. 1998, Hok, Save et al. 2005, Kjelstrup, Solstad et al. 2008, Burton, Hok et al. 2009, Royer, Sirota et al. 2010, Keinath, Wang et al. 2014). Moreover, damage to the vHPC disrupts representations of salient locations in mPFC (Burton, Hok et al. 2009), suggesting that the vHPC-mPFC projection may transmit SWM critical location information.

We therefore tested the role of vHPC-mPFC afferents in spatial working memory using an a projection silencing approach that afforded anatomical and temporal precision and found that the vHPC-mPFC direct input is necessary for encoding, not maintenance or retrieval, of SWM-dependent cues. Combining this approach with *in vivo* extracellular recordings of mPFC single units, we found that location-selective firing in the mPFC during SWM is dependent on vHPC direct input exclusively during the encoding phase of each trial. Finally, we found evidence that the transmission of task-critical information in the vHPC-mPFC pathway is mediated by the synchronizing of mPFC cells to gamma oscillations in the vHPC. Together, these findings suggest a role for the vHPC-mPFC pathway in the encoding of cues critical to SWM and may indicate a potential locus of pathophysiological disruption underlying the cognitive impairments associated with schiziphrenia.

TABLE OF CONTENTS

LIST OF FIGURES

Chapter 1: Introduction **Pages**

Chapter 2: Approaches to modulating hippocampal-prefrontal connectivity

Chapter 3: Behavioral effects of modulating hippocampal-prefrontal input

Chapter 4: Hippocampal-dependent encoding of location cues by mPFC

Acknowledgements

In concluding a series of projects that have collectively taken one sixth of my life to complete, I would like to thank some people whose support has been incalculable in guiding me through this challenging, tortuous, and ultimately enriching process. First, I would like to thank Josh, who accepted me into the lab when I was a first-year student with a background in psychology, a vague interest in circuit neurobiology, and zero immediately relevant experience or skills. His lucid scientific thinking, no-nonsense approach to mentorship, and personal and professional integrity have contributed to a predoctoral experience that has been immensely rewarding. I also want to thank Joseph Gogos, who welcomed a collaborative joint mentorship on a somewhat risky project using untested methods. His patience and guidance in this work are a testament to his appreciation for the importance of understanding the fundamental circuit bases of pathophysiologies in psychiatric disorders.

I would like to thank Mihir Topiwala and Torfi Sigurdsson for teaching me the finer points of rodent behavior and *in vivo* electrophysiology – their boundless patience and encouragement gave me the confidence to design my own experiments. Thanks as well to Susanne Ahmari and Mazen Kheirbek, in whose esteemed but short-lived *Center for Excellence in Neuroscience* I first learned to apply optogenetic techniques.

I owe many thanks as well to the senior post-docs with whom I collaborated and learned a great deal, including Karine Fenelon, Jayeeta Basu,

Liam Drew, and Mattia Rigotti. Many thanks also Randy Bruno, Henry Colecraft, and Attila Losonczy for helping to guide me through the development of my thesis over the past 4 years – their doors have always been open, and they have been generous with their advice and encouragement.

I would like to thank the other members of the Gordon lab, especially Avishek Adhikari, Pia-Kelsey O'Neill, Katya Likhtik, Andrew Rosen, Scott Bolkan, Joe Stujenske, Nancy Padilla, Selin Schamiloglu, Atheir Abbas, and Alex Harris, for making the lab a fantastic scientific environment and for always being willing to troubleshoot experiments, question basic assumptions, and lend a hand when needed. I want to thank Jennifer Saura, whose late-night sanity check-ins were essential to the completion of this work and whose collaboration on T-maze construction, cover art, and data visualization were invaluable. Lastly, I would like to thank my parents, John and Jeanne Spellman, who encouraged and supported my scientific curiosity from the very outset and without whom none of this work would be possible.

Chapter 1: Introduction

(Note: Portions of the this chapter were written in collaboration with Joshua Gordon, M.D./Ph.D. at Columbia University (Spellman and Gordon 2014).)

1.1 Introduction

Schizophrenia affects roughly 1% of the world's population, posing individual and societal burdens that include suffering and distress to patients and their families, as well as considerable treatment and institutionalization costs. In addition to positive symptoms, which include delusions, hallucinations and paranoias, for which effective treatment options do exist, schizophrenia is also characterized by pronounced negative and cognitive symptoms, for which treatment options remain elusive (Harvey, Green et al. 2004). Patients with cognitive symptoms experience profound difficulties in carrying out tasks essential to maintaining personal independence – particularly burdensome are deficits in working memory, the ability to acquire, store, manipulate, and employ behaviorally relevant information on a time scale of seconds (Baddeley 2003, Harvey, Green et al. 2004).

The heavy burden of working memory deficits in schizophrenia and the dearth of available treatment options are due in large part to the fact that the neural mechanisms that underlie working memory, and therefore the links between working memory and the pathophysiology of schizophrenia, remain poorly understood. The development of effective treatments for working memory deficits relies upon a clear understanding of both the circuit-level pathophysiology of the disease and the physiological bases of working memory itself. Here the

literature pertaining to both will be discussed, with an emphasis on areas where further study is essential.

1.2 Working memory: a compound cognitive process

Within the cognitive sciences, the recognition that short- and long-term memory are likely served by distinct mechanisms dates back at least to the work of William James. Referring to a class of memory in which environmental stimuli are held in an active state for attention, reflection, and action, declared that “an object of primary memory is thus not brought back; it never was lost” (James 1890). The unitary view of working memory as a single channel through which information is selectively routed into a long-term store (Atkinson and Shiffrin 1971) was challenged by Baddeley in the 1970s, who proposed a compartmental model in which working memory emerges from a central executive (attention/filtering and directed action), a phonological loop (verbal working memory) and a visuospatial sketchpad (visual and spatial cues) (Baddeley and Hitch 1974, Baddeley 2003).

Subsequently, the so-called “visuospatial sketchpad” was further divided into visual and spatial streams, following evidence that these two classes of representation could be independently measured and individually perturbed (Logie 1995, Baddeley 2003, Klauer and Zhao 2004). However, because schizophrenia patients show both spatial and verbal working memory impairment (Park and Holzman 1992, Conklin, Curtis et al. 2000), it is plausible that these

two processes share common underlying neurophysiology, which is disrupted by the pathophysiology of the illness. As will be discussed below, robust long-range connectivity likely plays an important role in the inter-structural transmission of stimulus-related information critical to the normal performance of working memory, and convergent evidence suggests disruption of such long-range functional connectivity in schizophrenia underlies the cognitive symptoms observed in the disease.

1.3 The vHPC-mPFC direct projection as a candidate signaling pathway for working memory-related spatial information

Data from clinical population goes beyond linking impairment of long-range synchrony to the pathophysiology of schizophrenia; human data can direct the study of the neurobiology of spatial working memory by identifying brain regions necessary for SWM performance. Human data suggest that both hippocampus and prefrontal cortex are critical for SWM, as damage to either structure results in SWM impairment (Jeneson, Mauldin et al. 2010, Barbey, Koenigs et al. 2013). This raises the possibility that the direct HPC-PFC projection mediates activity critical to the successful performance of SWM-dependent behavior.

Immediate early gene expression data suggests that performance of a SWM task, but not a control task involving similar motor behavior, results in increased activation of both HPC and mPFC (Yong Sang, Park et al. 2007).

Moreover, lesioning and in vivo pharmacological silencing data supports the hypothesis that both structures are necessary for successful SWM. Lee and Kesner found that lesioning or pharmacologically silencing the dorsal hippocampus (dHPC) in vivo impaired SWM at a 5 minute delay but not at a 10 second delay. Neither lesioning nor silencing the mPFC alone had any effect on performance (Lee and Kesner 2003). However, silencing either structure after lesioning the other resulted in complete impairment (chance-level performance) at both 10-second and 5-minute delays. This finding indicates a requirement for joint mPFC and hippocampal activity in the execution of delayed non-match-to-place behavior at delays as short as 10 seconds.

Wang et al found that unilateral silencing of neither mPFC nor ventral hippocampus (vHPC) affected SWM, while bilateral silencing of either structure significantly impaired SWM, and simultaneous contralateral silencing (i.e. right vHPC and left mPFC) resulted in impairment similar to bilateral silencing of each structure individually, suggesting that at least one unilaterally intact pair of structures is necessary for SWM (Wang and Cai 2006). The delays used in this study were adjusted according to each animal's individual performance and were not expressly reported. Findings from Izaki et al support a unique role for the dorsal caudal, or intermediate hippocampus (iHPC), in SWM, as excitotoxic lesioning of the mPFC and contralateral iHPC, but not vHPC, resulted in SWM deficit (Izaki, Takita et al. 2008). All these studies used a delayed non-match to place maze task, in which the animal was directed to a goal arm to obtain a

reward, then allowed to choose between returning to the same arm (no reward) or entering an opposing arm (reward).

Electrophysiological data further supports the idea that the HPC and mPFC are synchronized, and therefore potentially interactive, during SWM. Spiking of mPFC cells is often phase-locked to the prominent hippocampal theta rhythm, particularly strongly during the portion of a t-maze task immediately preceding turn choice, and this phase-locking increase is limited to correct trials (Jones and Wilson 2005). Theta *coherence* (a measure of the reliability of the phase relationship between waves or continuous time series signals) between mPFC and HPC also increases during the choice phase of the t-maze task (O'Neill, Gordon et al. 2013).

The HPC-mPFC projection is dense, ipsilateral, monosynaptic, and glutamatergic, with its cell bodies largely confined to the caudal/ventral hippocampus (Jay and Witter 1991, Jay, Thierry et al. 1992, Hoover and Vertes 2007, Takita, Kuramochi et al. 2007). In rodents, electrical stimulation of vHPC Ca1 results in EPSPs at monosynaptic latencies in both interneurons and pyramidal cells of layers 2/3 and 5 of the prelimbic mPFC (Tierney, De´gene` tais et al. 2004). Therefore, because of direct synapsing of HPC afferents onto inhibitory interneurons, it is plausible that vHPC-mPFC direct input may mediate the long-range coordination of gamma oscillations in the two structures, and that disruption of this connectivity could underlie long-range functional connectivity disruptions seen in schizophrenia.

The well evidenced role of long-range functional connectivity in the cognitive disruptions associated with schizophrenia, together with evidence for the importance of both vHPC and mPFC for the successful execution of spatial working memory, therefore suggests a likely role for the direct vHPC-mPFC pathway in SWM in both the execution of SWM-dependent behaviors and in long-range neural synchrony that critically supports these behaviors. The direct examination of this pathway in SWM is therefore a critical step in elucidating the neural circuitry disrupted in schizophrenia.

1.4 Neuropathophysiology in schizophrenia: a window into circuit-level cognitive dysfunction

Schizophrenia has long been hypothesized to be a “disconnection syndrome”, resulting from a discoordination of activity within and between brain regions (Friston 1999). This hypothesis, based originally on clinical symptomatology, was conceived prior to extensive research on neurophysiology. Nonetheless, over the past two decades a body of physiological evidence has emerged in support of disconnection as a prominent component of schizophrenia. Connectivity in neural systems is commonly assayed with measures of synchrony; temporal covariance in patterned activity is taken as evidence of neural interactions, and changes in synchrony that accompany shifting cognitive and behavioral states are seen as an indication of the relevance of such interactions to these states. There is now a substantial literature reporting schizophrenia-related disturbances in neural synchrony of varying frequency,

anatomical regionalization, and cognitive relevance (Singer. 2010). Broadly, these findings can be divided into deficits in local synchrony, characterized by alterations in the power or amplitude of local oscillations within a brain region, and deficits in long-rage connectivity, characterized by alterations in functional or anatomical connectivity between distant brain regions.

Disruptions in oscillatory activity, a measure of local synchrony

Disruptions in local synchrony can be detected in oscillatory activity, which is thought to arise during normal brain function from the synchronous activation of large numbers of synapses (Buzsaki and Wang 2012). Both evoked and spontaneous oscillations can be studied, and these do not necessarily reflect the same underlying circuit dynamics. Evoked oscillations are commonly interrogated by examining steady-state evoked potentials (SSEPs), typically with extracranial EEG electrodes. SSEPs are the responses to trains of sensory stimuli (typically auditory clicks) delivered at varying frequencies; they are typically widespread, and build to steady-state amplitudes over several hundred milliseconds. The gradual emergence, broad spatial extent, resonance, and frequency-dependence of SSEPs (strongest with 40-45Hz stimuli) suggest they reflect reverberant dynamics within recurrent cortical circuitry and not merely the sum of isolated individual responses characteristic of event-related potentials (Figure 1.1a) (Krishnan, Hetrick et al. 2009). This approach tests the ability of cortical circuitry to support oscillatory activity regardless of the underlying behavioral state, which may differ in patients and controls. Schizophrenia patients show pronounced

deficits in the amplitude of SSEPs (Kwon, O'Donnell et al. 1999, Brenner, Sporns et al. 2003, Wilson, Hernandez et al. 2008, Krishnan, Hetrick et al. 2009) which can be present at the first psychotic episode (Spencer, Salisbury et al. 2008). The severity of these deficits correlates with the severity of auditory hallucinations, suggesting that the circuit- and behavior-level phenotypes may be related (Spencer, Niznikiewicz et al. 2009). Inter-trial coherence (the temporal precision of physiological responses across presentations) is also disrupted in patients, and correlates with the severity of schizophrenia-associated working memory deficits (Light, Hsu et al. 2006). Collectively these data are suggestive of an impaired cortical circuitry that is unable to support normal oscillatory rhythmogenesis in response to appropriately timed stimuli.

Although the finding of impaired steady-state evoked responses is robust, reproducible, and correlated with symptomatology, it constitutes stimulus-locked, rather than intrinsically paced activity and therefore may not engage circuits in a way that mirrors normal functioning. A complementary approach is to measure oscillations evoked by specific tasks, though not time-locked to specific stimuli. For example, during a Gestalt visual stimulus response task in which patients had impaired performance, control subjects display a prominent 40Hz oscillation that corresponds with the initiation of a behavioral response. In schizophrenia patients, this oscillation is lower in frequency, and its strength correlates with symptom severity (Figure 1.1b) (Spencer, Nestor et al. 2004). Similarly, tasks dependent on working memory typically induce increases in oscillation strength in

prefrontal cortical circuits in healthy controls (Jensen, Gelfand et al. 2002, Jensen and Tesche 2002). Schizophrenia patients show reduced gamma and theta-frequency oscillatory power in frontal areas during such tasks (Haenschel, Bittner et al. 2009), and this reduction is correlated with impairments in task performance (Cho, Konecky et al. 2006).

Using magnetoencephalography, which has improved sensitivity and source localization compared to EEG, impaired oscillatory activity at higher frequencies can be seen. For example, deficits in gamma (60-120Hz) power over visual cortex has been found in patients during a visual face detection task (Grützner, Wibral et al. 2013).

Together, these studies demonstrate an important link between oscillations and behavior; they are correlated in healthy controls and jointly impaired in patients. However, differences between patients and controls might reflect systematic differences in the way they perform the tasks, rather than fundamental differences in circuit structure or function.

By contrast, data on oscillations in a “resting state”, absent a stimulus or task, has been used to demonstrate disease-related functional abnormalities absent any particular behavioral demands. Of course, the interpretation of resting state data is still challenging, most notably because it is unclear whether patients and controls are in equivalent behavioral states when asked simply to “rest.” Perhaps as a result, there is some disagreement as to whether the disorder affects resting state oscillatory synchrony. Some studies (Gandal, Edgar et al.

2012) suggest an increase in “baseline” or “resting state” gamma-frequency (30-80 Hz) activity in patients. However, one study found that resting-state activity in gamma-frequency oscillatory power was impaired in schizophrenia patients, as well as in their unaffected siblings, suggesting a relationship to genetic risk rather than disease state per se (Rutter, Carver et al. 2009). Notably, this report localized the impairments in gamma to cortical areas corresponding to the “default-network,” which is more active in a resting or internally-oriented state. Thus the impairment could reflect engagement in some alternative, active state (such as the experiencing of hallucinations or other positive symptoms), resulting in an inability to maintain a resting state. However, this is perhaps unlikely given that gamma oscillations have been shown to increase, not decrease, during hallucinations (Baldeweg, Spence et al. 1998).

Deficits in long-range synchrony

The strength of a locally generated oscillation is at best an indirect measure of synchrony, a conflation of the size of the rhythmically active neural population and the simultaneity of its firing. Synchrony across brain regions provides a direct measure of the functional connectivity of distant neural populations. While lacking in temporal resolution and therefore unable to speak to oscillatory dynamics, functional magnetic resonance imaging (fMRI) can be used to measure the covariance in localized BOLD signals from multiple brain regions more or less simultaneously. This allows one to examine synchronous

activation of far-flung brain areas during tasks or in the resting state, albeit on a slower time scale than with EEGs.

Results from fMRI studies of functional connectivity in specific circuits in schizophrenia patients are varied, and have included both increases and decreases relative to controls. For example, the examination of connectivity with medial prefrontal cortex (mPFC) found a reliable anticorrelation between mPFC and dorsolateral prefrontal cortex (dlPFC) in healthy controls that was absent in schizophrenia patients (Chai, Whitfield-Gabrieli et al. 2011). Meanwhile, a study of connectivity within and between two large brain networks – the default-mode and fronto-parietal networks – suggested that patients had decreased synchrony within parts of the default mode network, but increased synchrony between the default-mode and fronto-parietal networks (Chang, Shen et al. 2014).

A less directed approach to examining long-range synchrony is to measure global connectivity rather than analyzing specific networks of interest. Groups employing this approach have generally found lower connectivity in schizophrenia. For instance, a recent resting state fMRI study of schizophrenia and bipolar patients found lower global connectivity in both patient groups compared to healthy controls; connectivity correlated with symptom severity (Argyelan, Ikuta et al. 2014). Another recent whole-brain examination found increased fronto-parietal connectivity and decreased parietal-temporal and bilateral temporo-temporal connectivity. The increase in front-parietal connectivity correlated with positive symptom severity, while the decreases in connectivity

correlated with negative symptom severity (Venkataraman, Whitford et al. 2012). Yet another study demonstrated that pairwise functional connectivity throughout the brain is globally and significantly decreased in schizophrenia, while variance is increased; the brain-wide organization of weak connections in schizophrenia patients correlated with negative symptom scores, allowing for a diagnostic accuracy of 75% (Bassett, Nelson et al. 2012). The relative consistency of these whole-brain connectivity studies suggest that long-range connectivity is indeed globally disrupted in schizophrenia.

Possible neurobiological mechanisms of altered synchrony

As described above, studies of local synchrony with EEG or MEG suggest an inability of local circuits to support normal oscillations in schizophrenia, and examination of BOLD signal covariance indicates a global reduction in functional connectivity as well as specific disruptions in coordinated activity in critical schizophrenia-associated pathways. These two sets of findings are related in that they both suggest disrupted synchrony. But do they follow from the same underlying pathophysiology? Does either finding provide a causal link between schizophrenia risk and disease symptomology? Addressing these questions requires finding plausible mechanisms by which disruptions of cellular function produce the observed circuit and systems-level abnormalities. Two strong candidate mechanisms are hypofunction of fast-spiking parvalbumin-positive (PV+) interneurons, and disruption of myelination.

The critical role of GABAergic interneurons, particularly fast-spiking PV+ interneurons, in the generation of cortical oscillations, particularly gamma-frequency oscillations, is well established by direct manipulation of these cells in vivo; from such studies we have learned that optogenetically silencing PV+ interneurons impairs gamma (Sohal, Zhang et al. 2009) and that optogenetically driving them induces gamma (Cardin, Carlén et al. 2009). The literature on impairments in GABAergic interneurons in schizophrenia is long-standing and sizable (Lewis, Curley et al. 2012). Post-mortem studies have demonstrated reduced mRNA expression for GAD67, the enzyme that catalyzes glutamate into GABA (Guidotti, Auta et al. 2000, Curley, Arion et al. 2011). Such a decrease could result in less GABA or, alternatively, could reflect a downregulation of GABA precursors in response to impaired GABA metabolism. The GAD67 expression deficit is most pronounced in PV+ cells – in fact, GAD67 is not detectable in half of PV+ cells in schizophrenia patients (Hashimoto, Volk et al. 2003). Moreover, expression of parvalbumin itself is reduced in patients compared to controls, though the total number of these neurons may be normal (Woo, Miller et al. 1997). Because the strength of parvalbumin expression is activity-dependent (Donato, Rompani et al. 2010), this expression deficit could be a signature of hypoactivity. This hypoactivity may in turn result from an impairment of NMDA signaling, as disruption of NMDA signaling in PV+ cells reproduces a range of schizophrenia-related phenotypes, including decreased parvalbumin expression and behavioral impairments (Belforte, Zsiros et al. 2010). Finally,

computational modeling work has suggested a potential link between observed GAT-1/GAD67 deficiencies in PV+ cells and prolonged IPSCs that could account not only for the impairment of 40Hz entrainment to auditory clicks but also the preferential entrainment to slower 20Hz stimuli (Vierling-Claassen, Siekmeier et al. 2008).

PV+ interneuron-mediated disruptions of gamma oscillations may represent an underlying mechanism behind long-range functional connectivity disruptions seen in schizophrenia. While there exists ample evidence linking PV+ interneurons, gamma oscillations, and schizophrenia, gamma is thought to be generated in highly localized circuits (Buzsaki and Wang 2012). However, proposed mechanisms to explain long-range gamma synchrony across distant brain regions (Rajagovindan and Ding 2008, Vicente, Golloc et al. 2008) raise the intriguing possibility that disruption of fast-spiking interneuron networks may explain the observed impairments in long-range synchrony.

An alternative candidate link between cellular deficits and observed synchrony deficits is a schizophrenia-related disruption of myelination (Davis, Stewart et al. 2003). Myelination of long-range pathways permits for rapid signaling across long distances; disruptions in myelin might thus be expected to disrupt long-range synchrony.

Diffusion tensor imaging (DTI) allows for detection and quantification of fiber tracts using the measure of fractional anisotropy (FA), which detects the

degree to which the diffusion of water molecules is confined to a particular direction in any given voxel of brain tissue. While FA represents a conflation of axon number, thickness and level of myelination, it favors detection of white matter, due to the constraint of water molecules by multiple myelin layers (Kubicki, McCarley et al. 2007). Studies of DTI in schizophrenia patients reveal decreases in FA in both local and long-range connections. Locally, widespread decreases in FA have been found in frontal and occipital regions in patients despite preserved white matter volume, suggesting axon number and thickness do not account for the difference (Lim, Hedehus et al. 1999). In long-range projection pathways, schizophrenia patients have been found to have lower FA in the splenium of the corpus callosum and in the cingulum (Sun, Wang et al. 2003). Post-mortem histology also supports the idea that the myelin system is disrupted. Microarray analysis of DLPFC tissue from patients revealed impaired expression of genes related to myelination and oligodendrocyte function (Hakak, Walker et al. 2001). Electron micoscopy of post-mortem tissue reveals a higher density of concentric lamellar bodies, which signal damage to myelinated fibers, in caudate nucleus of patients relative to healthy controls (Uranova, Orlovskaya et al. 2001). There is also evidence of increased necrosis and apoptosis and decreased overall density of oligodentrocytes in prefrontal layer 4 in post-mortem patients (Uranova, Vostrikov et al. 2004).

Understandably, deficits in interneuron function have been proposed to underlie the abnormalities in local synchrony seen in schizophrenia. Similarly,

deficits in myelin have been proposed to underlie long-range connectivity abnormalities. But direct evidence for such a division is minimal, and the impact of the two cellular deficits could overlap (Figure 2). Long-distance synchrony can involve locally generated oscillations (Chai, Whitfield-Gabrieli et al. 2011) and may thus require interneurons to maintain this oscillation-based connectivity; moreover, it is become increasingly clear that there are inhibitory projection neurons that may be directly involved in long-range synchrony (Caputi, Melzer et al. 2013). With regard to the role of myelination, findings of heterogeneous distributions of myelin within and across neocortical neurons suggests more nuanced and potentially pathway-selective contributions to cortical communication (Tomassy, Berger et al. 2014). Modeling work has found that biologically relevant conduction delays on a scale consistent with changes in myelination can account for substantial attenuation of the amplitude of gamma oscillations (Pajevic, Basser et al. 2013). Thus heterogeneity of myelination could have implications for even local cortical synchrony, just as interneuron dysfunction could potentially disrupt long-range synchrony.

Mechanisms: linking synchrony to behavior

Animal models of schizophrenia predisposition play a critical role in sorting out the complex relationships between cellular mechanisms, circuit synchrony, and behavior. Animal models allow for direct genetic, molecular and circuit manipulation, and for testing the effects of such manipulations on local and long-

range synchrony as well as behavior. Indeed, disruption in synchrony is recapitulated in in multiple rodent models of schizophrenia, including pharmacological and genetic models. Pharmacological models have chiefly focused on the glutamate hypothesis, employing NMDA antagonists such as ketamine and MK801 to block NMDA receptors. Systemic administration of ketamine increases baseline spontaneous gamma-range activity and decreases auditory-evoked (paired clicks, as opposed to steady-state) responses, similar to some findings in patients, as described above (Lazarewicz, Ehrlichman et al. 2010). Stimulation of maternal immune response during pregnancy is another well-studied rodent model of schizophrenia predisposition, based on clinical evidence that early immune stress confers schizophrenia risk. Following maternal immune activation, impairments are seen in broad-spectrum hippocampal-prefrontral (HPC-PFC) synchrony (Dickerson, Wolff et al. 2010).

Finally, several genetic mouse models of schizophrenia predisposition have replicated deficits in synchrony. In a mouse homologue to the 22q11.2 microdeletion syndrome, there is evidence of impaired long range HPC-PFC synchrony in the theta and gamma ranges; the long-range synchrony deficits correlate with cognitive impairment (Sigurdsson, Stark et al. 2010). Moreover, a mouse heterozygous for a 22q11.2 component gene, Dgcr8, shows an inability to follow trains of 50-Hz stimulation in prefrontal layer II-V projections, a finding reminiscent of SSEP data from schizophrenia patients (Fénelon, Mukai et al. 2011). Mice heterozygous for the schizophrenia-associated gene *Disc1* gene

also show reduced HPC-PFC synchrony in the 30-50Hz gamma range (Kurihara, Dunlop et al. 2013). Recently, a mouse homologous for the human 15q13.3 deletion, which is associated with schizophrenia and epilepsy, was found to exhibit the SSEP gamma deficits and elevated baseline gamma (prefrontal and hippocampus) often seen in schizophrenia patients (Fejgin, Nielsen et al. 2013).

But while numerous studies have found impaired synchrony in rodent models of schizophrenia risk, recapitulation of the disruption in circuit dynamics does not complete the picture. A model that links risk with circuit pathophysiology requires elucidation of the cellular and molecular signaling components of the disruption; for the models listed above, these mechanisms are unclear to date, though work continues to define them. One promising model where the cellular mechanisms have been more clearly defined involves neuregulin, a candidate schizophrenia-related gene that facilitates glutamate receptor subunit expression and is involved in synapse formation and stabilization. Neuregulin enhances cortical gamma oscillations in vivo and in vitro, acting on GABAergic interneurons and mediated by synapses (as opposed to gap-junctions) (Hou, Ni et al. 2014). Moreover, deletion of Erbb4, a receptor for neuregulin, from PV+ interneurons results in decreased HPC-PFC theta coherence under anesthesia and increased HPC gamma power during running (Figure 1.1c) (Del Pino, García-Frigola et al. 2013). Thus investigating the interactions between neuregulin and Erbb4 and their downstream consequences on synapse and circuit function is one potential avenue by which we might begin to mechanistically link genetic risk with neural

synchrony deficits. Similar links upward from synchrony to behavior might be forged with any of the models mentioned here.

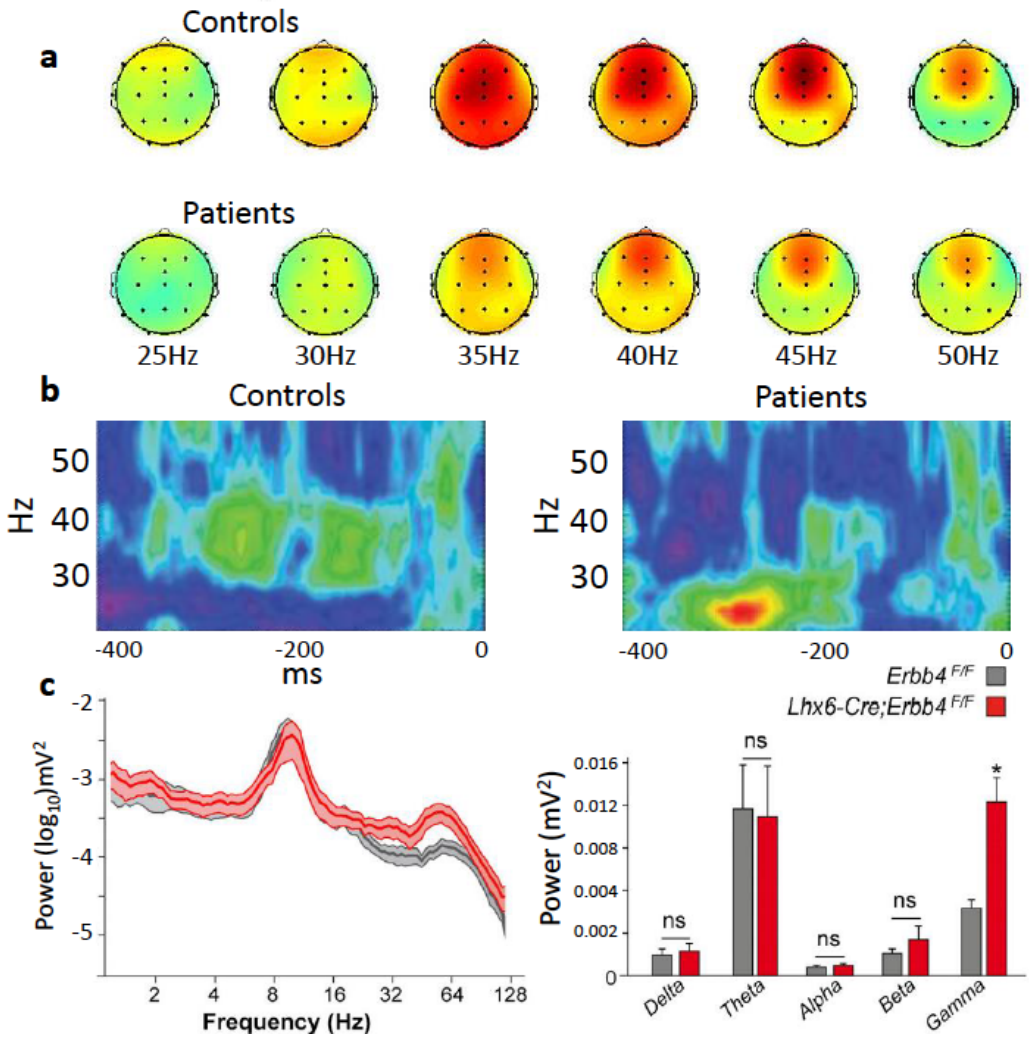

Figure 1.1 Disruptions in gamma synchrony in schizophrenia patients and in genetic animal models.

(A) A widespread SSEP response is seen to 35-45Hz stimulus trains; this response is larger in healthy controls compared to patients with schizophrenia (Krishnan, 2009).

(B) During a visual gestalt task, the characteristic 40 Hz oscillation induced in controls (left) is lower in frequency (middle) and correlates with symptoms in schizophrenia patients (Spencer, 2008).

(C) Spectral power in the hippocampus of mice lacking the Erbb4 neuregulin receptor in PV+ interneurons (red) and control mice (grey). Deletion mice show a significant, frequency specific increase in gamma power (Del Pino, 2013).

Chapter 2: Approaches to modulating hippocampal-prefrontal connectivity

(Note: The experiments on light-induced heat diffusion in neural tissue described in this chapter were completed in collaboration with Joseph Stujenske, M.Phil., in the lab of Dr. Joshua Gordon, M.D., Ph.D., at Columbia University. J.S. built the computational model, and T.S. performed the *in vivo* validation experiments.)

2.1 Introduction

The ability to perform experiments requiring reversible neural inhibition on the time scale of working memory is among the most valuable features of recent generations of light-activated microbial opsins, collectively known as optogenetics (Yizhar, Fenno et al. 2011). The ability to constrain optogenetic inhibition to individual projection pathways has furnished experimentalists with an added dimension of control in study design, namely the targeting of inhibitory manipulations to desired pathways of anatomical connectivity. By systematically applying reversible silencing to relevant connections during corresponding behavior, experimentalists may begin to produce a functional connectome. It is therefore critical, particularly at the early stages of its use, that optogenetically mediated terminal inhibition be validated not only behaviorally but physiologically as well.

Relatively little work has been published to date to provide physiological validation that axon terminals can be robustly silenced by synthetic membrane-bound proteins localized to the synapse. Various groups have, for several years, leveraged such proteins to affect behavior (Tye, Prakash et al. 2011). DREADDS (designer receptors exclusively activated by designer drugs) have been shown to

silence synaptic transmission *in vitro*, a result demonstrated by paired patching and pharmacological manipulation (Stachniak, Ghosh et al. 2014). Chromophore-assited light inactivation (CALI), which uses reactive oxygen species to endogenously inactivate synapses, has similarly been validated physiologically *in vivo* (Lin, Sann et al. 2013). Terminal inhibition using optogenetics, to our knowledge, has not yet been demonstrated *in vivo*. However, it has been validated physiologically *in vitro* by expressing excitatory and inhibitory opsins in the same construct, then abolishing the effect of light-mediated excitation with concurrent light-mediated inhibition (Stuber, Sparta et al. 2011).

In vitro preparations are not directly analogous to *in vivo* conditions in numerous respects, lacking contributions from long-range inputs, and ongoing spontaneous activity that may mitigate or amplify the effects of synthetic silencing. Moreover, due to experimental variation in the spatial extent and intensity of opsin expression, as well as variable time-courses for expression along axon extents, it is important to demonstrate the extent to which axon terminals can be inhibited in a given experimental preparation. While a behavioral change in response to the combination of opsin expression and light stimulation constitutes evidence of neuronal inhibition, physiological validation serves as supporting evidence that an observed behavioral change is in fact due to the optogenetic manipulation and not and a nonspecific interaction of opsin expression and light stimulation.

This chapter describes experiments that serve as groundwork for the use of optogenetics to inhibit axon terminals i*n vivo*. First, the potential for light-induced temperature changes in neural tissue will be described, including background on known effects of temperature changes on neural activity, a computational model that predicts light-induced temperature changes in neural tissue, and experimental validation of the model. Next, experimental validation of the approach of in vivo optogenetic terminal inhibition will be described and discussed.

2.2 Effects of Light on Temperature of Illuminated Neural Tissue In Vivo

Optogenetic tools have, in recent years, become a standard class of experimental manipulation in studying circuit-level neural systems. Since their effectiveness was first demonstrated in the mammalian nervous system (Boyden, Zhang et al. 2005), the use of light-activated microbial opsins to carry out loss-of-function and gain-of-function experiments with ever-greater anatomical, temporal, and cell-type specificity has made it all the more critical to better understand the precise physiological mechanisms by which observed behavioral changes are produced. These tools require only endogenous expression of microbial opsins and the application of light, avoiding the need for more the acutely invasive approach of intracranial drug administration. However, *in vivo* optogenetic experiments, in particular experiments involving the use of the inhibitory microbial opsins such as archaerhodopsin and halorhodopsin for prolonged neural

inhibition, require electromagnetic radiation within the visible light spectrum to be applied directly to neural tissue, which has the potential to induce temperature changes within a range which previous work has associated with physiological changes (Acker and al. 2012, Christie and al. 2012, Han 2012). It is therefore important, when designing such experiments, to carefully consider the parameters used for tissue illumination, in order to minimize unnecessary risk of inducing heat-associated activity changes with might confound results. While groups performing earlier experiments have made estimates of such temperature changes for brief light stimuli (Yizhar et al., 2011), accurate models for prolonged illumination are presently lacking.

The effects of temperature changes on various physiological features of neuronal functioning have been studied previously. *In vitro* experiments in which bath temperatures were systematically varied produced changes in spontaneous firing rate, membrane resistance, time constant, resting potential, and synaptic activity (Thompson, Masukawa et al. 1985, Volgushev, Vidyasagar et al. 2000, Volgushev, Vidyasagar et al. 2000, Kim and Connors 2012). Temperature-dependent effects on the amplitude of evoked synaptic responses *in vivo* have been reported as well (Moser E 1993, Andersen and Moser 1995). Moreover, physiological effects of temperature have been leveraged to alter neural activity *in vivo* using cooling probes (Ponce, Lomber et al. 2008, Vicente, Golloc et al. 2008). It therefore plausible and even likely that optogenetically-associated illumination of neural tissue may induce physiological and behavioral changes by

virtue of the light-induced heat alone, absent any opsin-mediated effects (Yizhar, Fenno et al. 2011, Han 2012).

While heat-associated behavioral and physiological effects associated with prolonged illumination in optogenetic experiments has not been directly tested, previous work indicates that heat produced by prolonged illumination may suffice to change neural activity (Acker and al. 2012, Christie and al. 2012). We therefore sought to refine and validate a model of the time course of light-induced heat in neural tissue using an *in vivo* preparation. Finding the chosen heat model to be a good predictor of induced heat, we used it to inform our selection of experimental parameters in subsequent optogenetic experiments.

Modeling Light-Induced Heat Induction in Optogenetic Experiments

To model the heat induced by direct illumination of neural tissue *in vivo*, we first selected a model and set of parameters for the spread of photons from the tip of an implanted fiber optic light source. For this we employed a Monte Carlo model to simulate photon trajectories. To simulate the induction and diffusion of heat, we used a model based on the Pennes bio-heat transfer equation, using experimentally obtained values for brain density, conductivity, and specific heat (see Methods).

To validate the model and to determine an appropriate set of values for input parameters, we compared output values from the model with measurements obtained from direct measurement of optically-induced

temperature changes *in vivo*. We generated model predictions using input parameters for scattering and absorption from experimentally obtained values from *in vivo* neural tissue (Johansson 2010), as well as from acute slices (Yaroslavsky et al. 2002). While the light spread in the two simulations was similar due to similar scattering coefficients, they diverged substantially in their absorption coefficients – this can likely be attributed to the absorption of light energy by blood, which is present *in vivo* but not in the exsanguinated slices used for the *in vitro* measurements. Because of differing absorption coefficients, the parameters obtained from *in vivo* measurements produced a 3 to 5-fold larger temperature change than those from *in vitro* measurements.

To determine how the selection of input parameters affects the accuracy of predicted temperature changes, we cross-validated the two simulations with experimentally measured temperature changes in an *in vivo*, acute anesthetized preparation (532 nm wavelength, 10 mW, 62 μm diameter, .22 NA). Mice were acutely implanted with a microthermistor and an optical fiber from craniotomies in opposite hemispheres, such that the thermistor was positioned within the fiber's light beam through undisturbed tissue. The distance between the tips of the micothermistor and the fiber was then systematically varied (Figure 2.1A). As predicted, the recorded temperature changes were similar to those predicted by the simulation with model parameters obtained from *in vivo* measurements, although for distances under 200uM, temperature changes were underestimated on the order of 1°C. We found that the discrepancy could be accounted for when

the direct effect of incidental light on the surface of the microthermistor was factored in – this direct effect was measured in a temperature-controlled bath of saline. (Figure 2.1B; see methods). Predicted temperature changes were also in agreement with heat induced by blue light in previous work (Christie and al. 2012).

In contrast with the results from model parameters obtained from *in vivo* measurements, predictions for heat induction using model parameters measured *in vitro* were notably smaller than our experimentally measured changes. Notably, predicted temperature changes peaked at a delth of 100-200μm, while the measured temperature changes peaked at depths approaching zero. This may be due to discontinuities within the tissue such as extracellular blood, non-uniformity of temperature sensitivity of the microthermistor across its surface, or reflection of light off the thermistor surface, resulting in increased light in the tissue surrounding the microthermistor itself.

We next took advantage of the fine temporal resolution of the model to examine the time course of induced temperature changes and compare with an experimentally obtained time course. This comparison, however, revealed a faster time to steady state produced by the model than by observation via the microthermistor. This was likely due to intrinsic delays in the thermistor itself (Figure 2.1C). When we added a delay kernel to account for the temporal dynamics of the thermistor, the temperature change predicted by the model still had a higher initial slope than the measured temperature time course, but the

time required to reach 90% steady state was similar (Figure 2.1C-D). The intensity of light used did not affect the time course of heat induction. Both the predicted and observed time courses agree that temperature change reaches 80% steady state within 5 seconds.

Light power is an experimental parameter of obvious importance for the design of optogenetic experiments. Higher power allows for illumination of greater volumes of tissue and higher proportions of local opsin channels, while excessive light power has the potential to damage tissue. We therefore used our model to examine whether the relationship between light power and temperature was linear, averaging temperature changes at various depths over 250uM circular areas. Not surprisingly, the relationship was in fact linear, peaking near 200uM below the fiber tip (Figure 2.2A).

Another parameter of interest to the design of optogenetic experiments is fiber diameter. Commercially available fibers that could feasibly be chronically implanted range from 62uM to 400uM – the relationship between fiber diameter and heat induction is therefore of direct interest to optogenetic investigators. Our model predicted that, within 100uM of the fiber tip, peak temperature changes were up to 50% greater for a 62uM diameter fiber than for a 200uM fiber (Figure 2.2B). This difference decayed as a function of distance from fiber tip (Figure 2.2E). This result suggests that, when experimental design permits, larger fibers are generally preferable to smaller ones, though this concern may be avoided by placing fibers at greater distance (>100uM) from target tissue.

2.3 Opsin-mediated inhibition of HPC-to-mPFC terminals *in vivo*

Having established a set of optical stimulation parameters with which light-induced heat effects were unlikely to exceed a physiologically normal range, we next sought to design an experiment to test whether optogenetic inhibition of axons terminals could interfere with synaptic transmission.

In order to specifically interfere with the inputs from the HPC to the mPFC, a projection-specific targeting approach was used. An adeno-associated virus vector (AAV2/5) engineered to express enhanced archaerhodopsin (Belfort, Lin et al. 2010, Gradinaru, Zhang et al. 2010) fused to enhanced yellow fluorescent protein (eYFP) was targeted to subfield Ca1 of vHPC in male C57BL/6J mice. Following a 6-week incubation period, robust expression was seen in dendrites and axons of vHPC, as well as in projection axons afferent to prelimbic (PL) and infralimbic (IL) regions of mPFC (Figure 2.5A). Fluorescent axons were densest in layers 2-6 of IL and layers 5-6 of PL. Histological examination of slices from animals transfected with CamKIIa-mCherry in ventral Ca1 and co-stained with a NeuN antibody revealed that 45 +/-13% of neurons in ventral Ca1 were co-labeled (Figure 2.4).

To determine whether Arch-mediated hyperpolarization of distal axon terminals affected spontaneous firing of vHPC cells expressing the opsin (e.g. via passive conductance), tetrode bundles coupled to an optical fiber were implanted in the vHPC, as well as an optical fiber in the mPFC. Light pulses (532nm,

10mW, 10sec) delivered to vHPC silenced roughly 50% of spontaneous multiunit activity (MUA) in the awake/resting state, while illumination of terminal fields had no impact on MUA, suggesting that terminal illumination did not affect spontaneous activity at the level of the cell bodies (Figure 2.5B).

Next, the effect of terminal illumination on synaptic transmission was measured. In acutely anesthetized mice, electrical stimuli (500μA, 0.1ms, 30sec ISI) were delivered via a bipolar stimulating electrode positioned in ventral Ca1 in Arch-expressing mice and un-injected controls, while postsynaptic MUA in the mPFC was recorded using optical fiber-coupled stereotrodes. Electrical pulses produced robust evoked MUA responses with a latency of between 5 and 40ms post-stimulus (Figure 2.5C). Light pulses delivered to the mPFC on interleaved trials reduced the evoked MUA response by ~40% for Arch animals but not controls (Figure 2.5D).

2.4 Discussion

Here we have validated the approximate accuracy of a model of light-induced heat and its diffusion in living brain tissue and used it to identify parameters for the design of optogenetic experiments. This model represents an advancement on other widely used and cited models, in that it makes use of physically realistic Monte Carlo statistics of light scattering rather than assuming straightforward geometries for light spread, and that it takes into account physiologically realistic absorption and scattering coefficients – the importance of

these experimentally obtained values in reaching accurate model predictions is evidenced by the degree to which the model agrees with observed temperature changes.

Here the model and the parallel experiment are in agreement in finding temperature increases across large volumes of illuminated tissue as high as 4° C at light intensities frequently used in optogenetic experiments. A temperature increase on this order has been found previously to alter both circuit-level neural activity and behavior (Thompson, Masukawa et al. 1985, Moser, Mathiesen et al. 1993). Moreover, it should be noted that temperature changes capable of producing observable changes in physiology may not affect behavior that depends on the affected circuit (Moser and Andersen 1994, Marder 2011). The ability of neural networks to shift modes as a function of changes in factors such as temperature and yet produce functionally equivalent outputs is of particular concern to those studying *in vivo* physiology – a network of cells may homeostatically alter their behavior with no overall loss of function, obscuring the naturalistic activity an experimenter is looking for. The potential for light-dependent effects mediated by heat serves to underscore the importance of opsin-negative controls in every experiment.

We therefore used experimental parameters informed by our model to validate our ability to selectively and reversibly inhibit axon terminals *in vivo*, which to our knowledge has heretofore not been demonstrated. In fact, we found that, expressing eArch3.0 under the CamKIIa promoter and allowing 6 weeks for

incubation, we were able to reduce evoked post-synaptic response by ~40%. It is important to note the indirect nature of this measurement as a means of testing terminal inhibition. Post-synaptic multi-unit response may be a sub- or supralinear function of synaptic transmission. We also cannot ascribe a precise mechanism to this inhibition – it may be that action potentials are prevented from reaching synaptic terminals, or that neurotransmitter release probability is diminished. Given the prohibitive difficulties of patching these projection axons, particularly *in vivo*, it will suffice for the purposes of our subsequent experiments to know that the effect on post-synaptic activity is diminished. The magnitude of this effect, moreover, remains unclear. While an averaging of evoked response across the entire 40ms post-stimulus window yields a decrease of ~40%, at earlier time points (notably the 5-10ms bin) the decrease is nearly 100%. Given that 5-10ms represents the latency for the initiation of the monosynaptic response (Figure 2.3), and that later timepoints are likely contaminated by polysynaptic reverberant response, the figure of a 40% reduction represents a minimum, not a true, effect size.

2.5 Methods

Subjects

Male C57 mice (Jackson Labs) were used for all experiments, aged 8-12 weeks at first use. Mice were housed in a New York State Psychiatric Institute satellite facility and were maintained on a 12-hour light-dark cycle. Except when

food-restricted for the purpose of behavioral training and testing, all mice were given ad libitum access to food and water. Presurgical mice were group-housed with littermates, while mice with chronic recording implants were singly housed in divided cages with visual, auditory and olfactory contact with another implanted mouse. All procedures were approved by Columbia University and the New York State Psychiatric Institute IACUCs.

Surgical Preparation

Animals were placed inside a flow box and anesthetized with isoflurane gas (2%) until sedated, at which point they were placed in a stereotax and maintained on 0.5% isoflurane for the duration of the surgery. Craniotomies were made bilaterally above mPFC and vHPC (coordinates below), and skull screws placed over cerebellum and olfactory bulb served as ground and reference, respectively. In the acute anesthetized experiment, surgical depth was maintained with isuflurane for the duration of the experiment.

Viral Transduction

AAV2/5 of titer exceeding 10^{12}vg/ml (UNC Vector core and UPenn Vector Core) was used to package all viruses. Virus was targeted to multiple targets within stratum pyramidal of ventral Ca1 (2 mediolateral rows at AP 2.95 and 3.25, with sites at ML/DV: 2.65/4.5, 3.0/4.3, 3.35/3.9, 3.7/3.3-2.9. An additional row

was made at AP 3.1, with ML/DV sites at 2.8/1.55 and 3.15/1.7. All coordinates reported in mm, all AP and ML w.r.t. bregma, DV w.r.t. brain surface. A 200nL bolus was delivered to each site via glass micropipette (20-40μM diameter) at a rate of 100nL/min continuous infusion, with a wait time of 5 minutes between infusion and retraction.

Electrode and Fiber Implantation

Spikes were recorded using stereotrodes (mPFC) and tetrodes (vHPC) made from 13μM-diameter tungsten fine wire. Stereotrodes were coupled to ferrule-bound optical fibers (Thorlabs, 200μM-diameter core, 0.39NA) positioned 300-500μM dorsal to the stereotrode tips, which were arrayed semicircularly around the lateral edge of the fiber. Fiber-coupled stereotrode bundles were then implanted bilaterally in mPFC (1.8mm anterior, 0.4mm lateral, 1.4mm ventral), while tetrode bundles were implanted bilaterally in vHPC (3.1mm posterior, 3.0mm lateral, 3.9mm ventral). Tetrodes were advanced until spikes with putative pyramidal-cell waveforms were detected. mPFC optical fibers in these 4 animals were coupled to bilateral LFP wires. All movable microdrives were advanced at a rate of 40μM per day across all recording days. Prior to sacrificing and perfusing implanted animals, recording sites were histologically confirmed by visual examination of electrothermolytic lesions. Lesions were induced by passing current through an electrode at each implanted site (50μA, 20sec). Perfused and

fixed tissue was then sectioned, and DNA was stained using DAPI Fluoromount-G mounting medium (Southern Biotech).

Acute recording and stimulation

Animals were placed inside a flow box and anesthetized with isoflurane gas (2%) until sedated, at which point they were placed in a stereotax and maintained on 0.5% isoflurane for the duration of the surgery. Craniotomies were made bilaterally above mPFC, and skull screws placed over cerebellum and olfactory bulb served as ground and reference, respectively. Surgical depth was maintained with isuflurane for the duration of the experiment. Electrical stimuli (500μA, 0.1ms, 30sec ISI) were delivered via a bipolar stimulating electrode positioned in ventral Ca1 in Arch-expressing mice and un-injected controls, while postsynaptic MUA in the mPFC was recorded using optical fiber-coupled stereotrodes. Recordings were amplified, band-pass filtered (1-1000Hz LFPs, 600-6000Hz spikes), and digitized using the Neuralynx Digital Lynx system. LFPs were collected at a rate of 2kHz, while spikes were detected by online thresholding and collected at 32kHz. Noise (electrical stimulus artifact) was initially clustered using Klustakwik (Ken Harris), sorted according to the first two principal components, voltage peak, and energy from each channel.

Modeling Heat Diffusion

To model heat diffusion, a tissue volume was modeled as a cylindrical volume with radius 6 mm, height 10 mm, with boundaries absorbing heat. Heat movement through the volume was modeled using the well-established modified diffusion equation, the Pennes' 'bio-heat transfer' equation (Pennes 1948), which in previous work has been used to model heat in brain tissue (Aronov and Fee 2011):

$$\rho c \frac{\partial T}{\partial t} = \nabla k \nabla T + \rho_b c_b w_b (T_A - T) + q_m$$

Here T represents tissue temperature (baseline: 37°C) while T_A is constant arterial blood temperature (36.7 °C). k, and ρ, c denote thermal conductivity, density, and specific heat, respectively. Values for blood are denoted ρ_b and c_b. w_b and q_m denote, respectively, rate of blood perfusion and the endogenous heat produced by metabolism.

Temperature measurement

Two mice (male C57/B6, 8-12 weeks old) were deeply anesthetized with isoflurane and mounted into a stereotax. A craniotomy was made over the lateral surface of the frontal cortex, on either side. A small, 62 micron diameter optical fiber was coupled to a 532 nm laser (OEM lasers) and passed from one end of the brain through to the other end. A thermistor probe was pressed firmly against the surface of the cortex, anti-parallel to the optical fiber, so that their centers

aligned. Heat measurements were made before, during, and after 60 seconds of illumination at various distances between the thermistor and fiber (0-1.6 mm). Both 10 mW and 20 mW intensities were tested. After surgery, the mice were euthanized with a lethal dose of ketamine.

We chose to use a thermistor because of its high temperature sensitivity at physiological temperatures. Thermistor resistance readings were calibrated to temperature by touching the thermistor tip to temperature controlled baths of water. As expected, a log-linear relationship was found between resistance and temperature. To compare model outputs to thermistor readings, we accounted for two unavoidable sources of experimental error introduced by the thermistor readings. First, the temporal delays introduced by the thermistor were calculated. In a medium of constant temperature, the temperature reading of the thermistor was found to be accounted for by a simple exponential time constant of about 4 seconds. However, in our experiment only part of the metal was in contact with the brain, while the rest was in a medium of roughly constant temperature (air). This introduced a non-linearity into the temporal dynamics of the thermistor readings. To correct for this non-linearity, a temporal kernel was measured experimentally by touching the tip of the thermistor to a water bath held at various temperatures (equivalent to step function increase). Since water has a similar thermal conductivity to brain, we reasoned that this should approximately emulate the temporal dynamics in our experiment. The calculated kernel was used to convolve the model output to introduce a non-linear temporal delay.

Second, the effects of light directly hitting the thermistor and being absorbed by the metal were modeled. The conversion of incident light power to steady state resistance changes in the metal were measured in water held at 37°C by illuminating the thermistor with an optical fiber at various distances (0-1 mm). There was a measured increase of .08 °C/mW at a distance of 0 mm, with the measured temperature change dropping off in a way that was well-modeled by the attenuation of light in saline (non-scattering medium). For modeling, the temporal dynamics for this direct light absorption were treated as having the same non-linear kernel as measured previously.

An important caveat for any means of measuring temperature change is the potential contribution of the device itself to temperature changes in the tissue. In particular, direct heating of the thermistor by directly incident light might artificially elevate the temperature change in the brain. However, the contribution of direct light absorption was negligible past 1 mm from the fiber, at which distances our model reliably predicted recorded temperature changes in the brain. For this reason, we concluded that incident light on the thermistor did not explain our results.

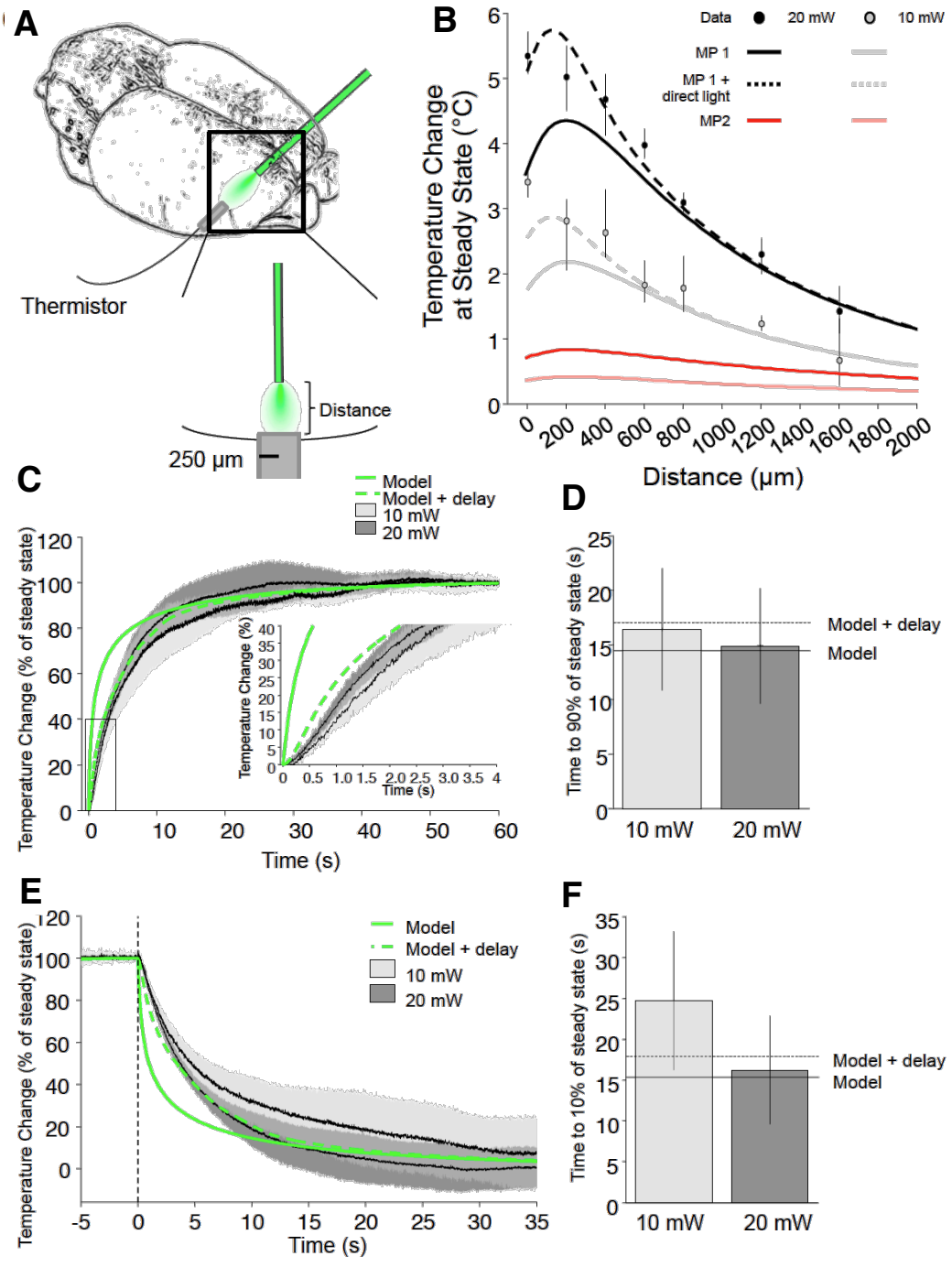

Figure 2.1 Validation of Light-evoked Heat Model with In Vivo Temperature Measurements

(A) Experimental design for measuring temperature change from optical illumination in the mouse brain.

(B) Temperature changes measured for various distances between an optical fiber (532 nm, 62 μm, NA .22) and a thermistor for both 10 mW (gray circles) and 20 mW (black circles) power output. Error bars indicate the range of all measured temperatures across 5 repetitions. On the same axes, predicted temperature change as a function of depth is plotted for both sets of model parameters are plotted for 10 mW and 20 mW light power. The effects of direct light were also included and plotted for the first model (dashed lines).

(C) Temperature change as a function of time from light onset for both 10 mW and 20 mW light power recorded at a thermistor 400 μm away from an optical fiber as in (A) Super-imposed are the predictions for the model with (green, dashed) and without (green) a compensatory delay measured for the thermistor experimentally. Error bars indicate the entire range of recorded values.

(D) Time to reach 90% of steady state temperature for 10 mW (light gray) and 20 mW (dark gray) power output at 400 μm distance. Predictions for the model are plotted with (black) and without (dashed black) delay.

(E) Temperature change at a distance of 400 μm as in (A), except after turning off light output.

(F) Time to reach 10% of steady state temperature after light offset, plotted as in (B)

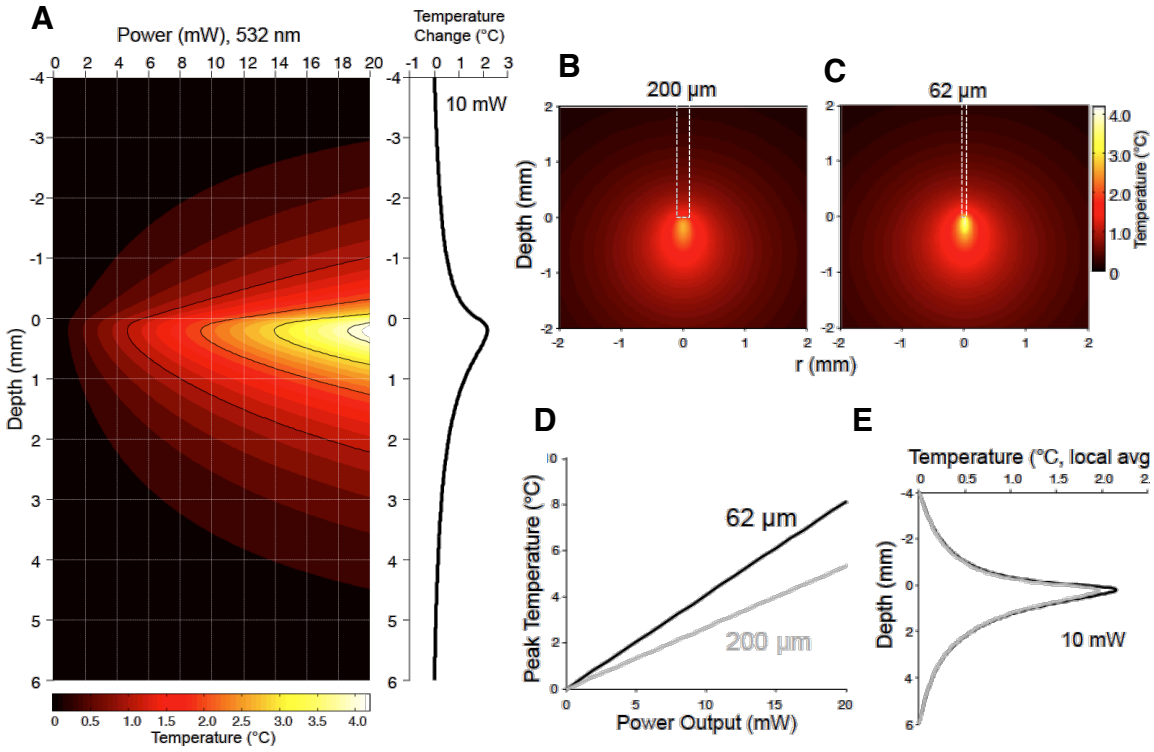

Figure 2.2 Effects of Changes in Relevant Light Parameters on Temperature

(A) Predicted temperature change as a function of power and depth (averaged in 250 µm circles below the fiber; 532 nm, 62 µm, .22 NA). An example curve is shown for 10 mW on the right

(B) Predicted temperature change as a function of distance from an optical fiber (532 nm, .22 NA) of either 200 µm (left) or

(C) 62 µm (right) diameter.

(D) Peak temperature change (maximum temperature change in a voxel) as a function of power output for 62 µm and 200 µm fibers as in (B-C).

(E) Temperature change as a function of depth, quantified as in (A) for the 62 μm and 200 μm fiber of (B).

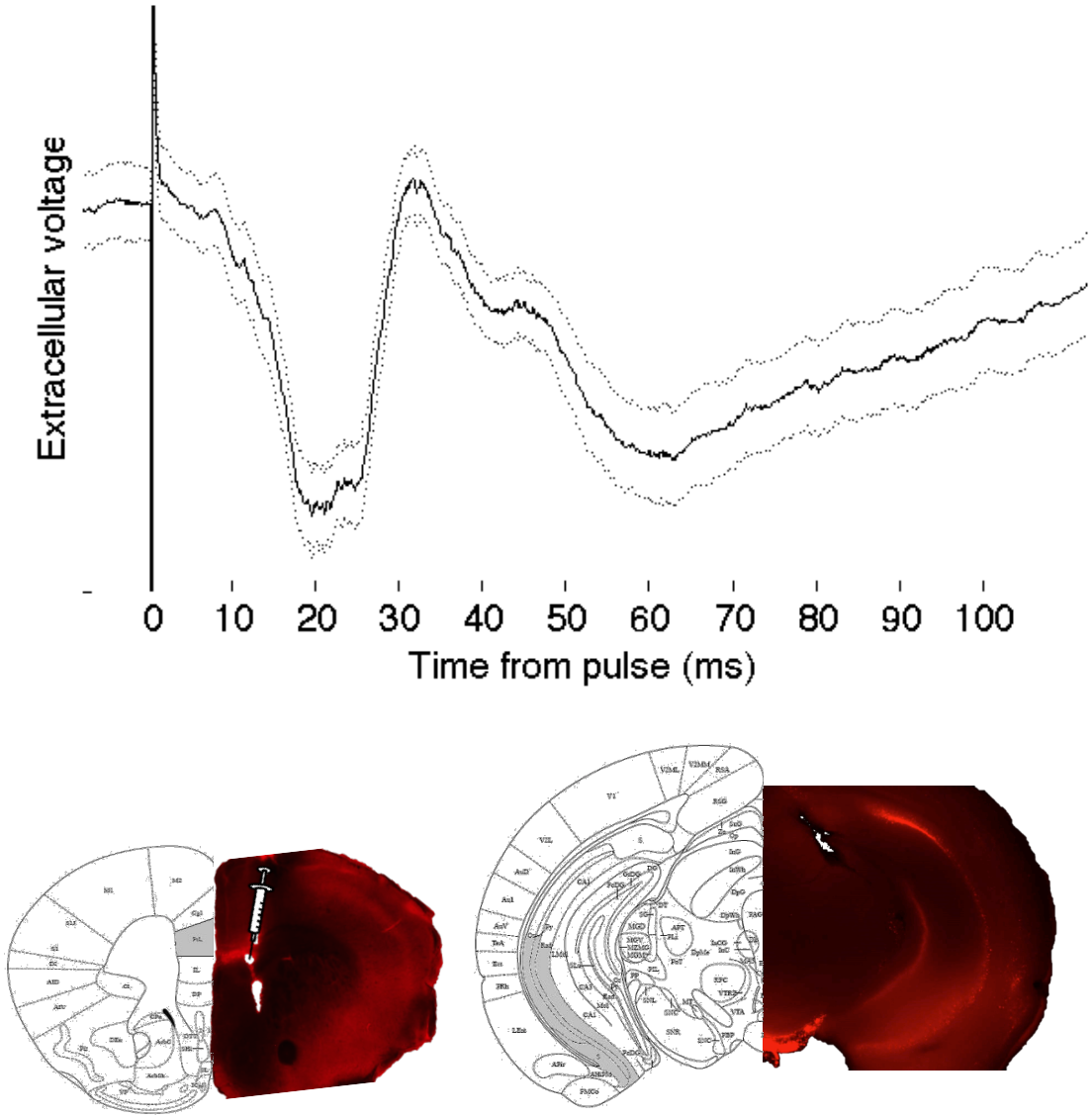

Figure 2.3 Characterizing the vHPC-mPFC projection in vivo

(A) Depolarizing extracellular field responses are visible in mPFC beginning 5-10ms after delivery of electric pulses to vHPC Ca1—this latency is putatively monosynaptic, given the ~5mm range of the direct projection and its unmyelinated conduction velocity.

(B) Site of injection of Lumofluor retrograde fluorescence beads in mPFC.

(C) Resulting labeling of pyramidal layer of ventral Ca1.

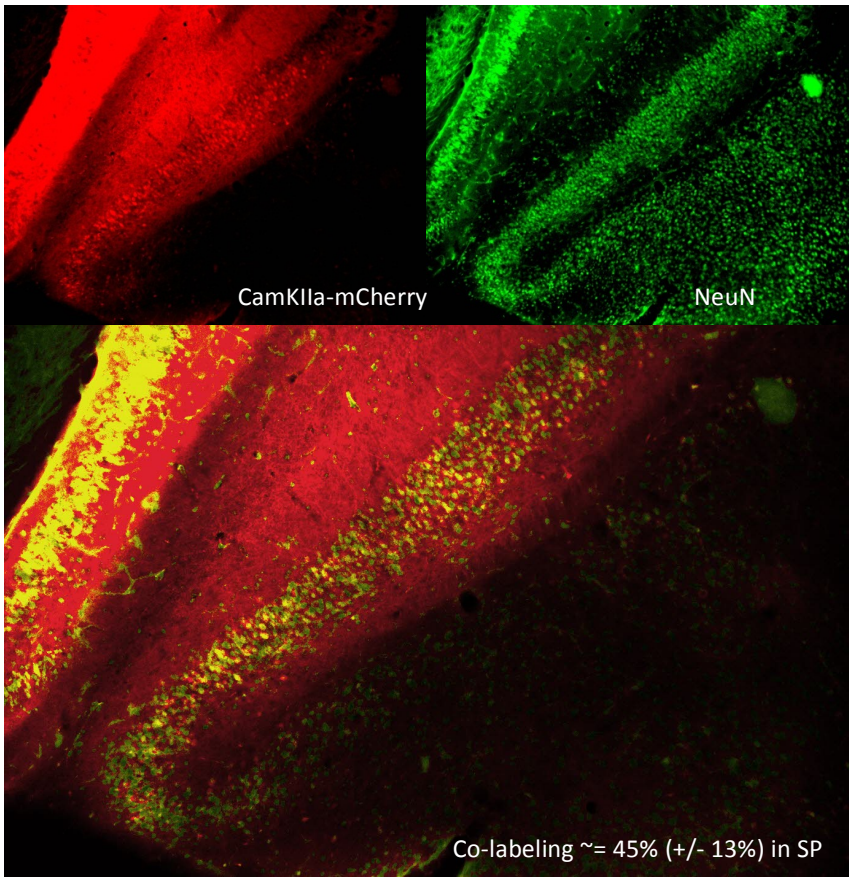

Figure 2.4 Expression of virally-packaged synthetic protein in vHPC Ca1

After a 6-week incubation period following targeted injection, robust expression is seen in ventral Ca1. In vHPC Ca1 of mice expressing mCherry under the CamKIIa promoter, co-labeling of mCherry was seen in ~45% of NeuN positive cells.

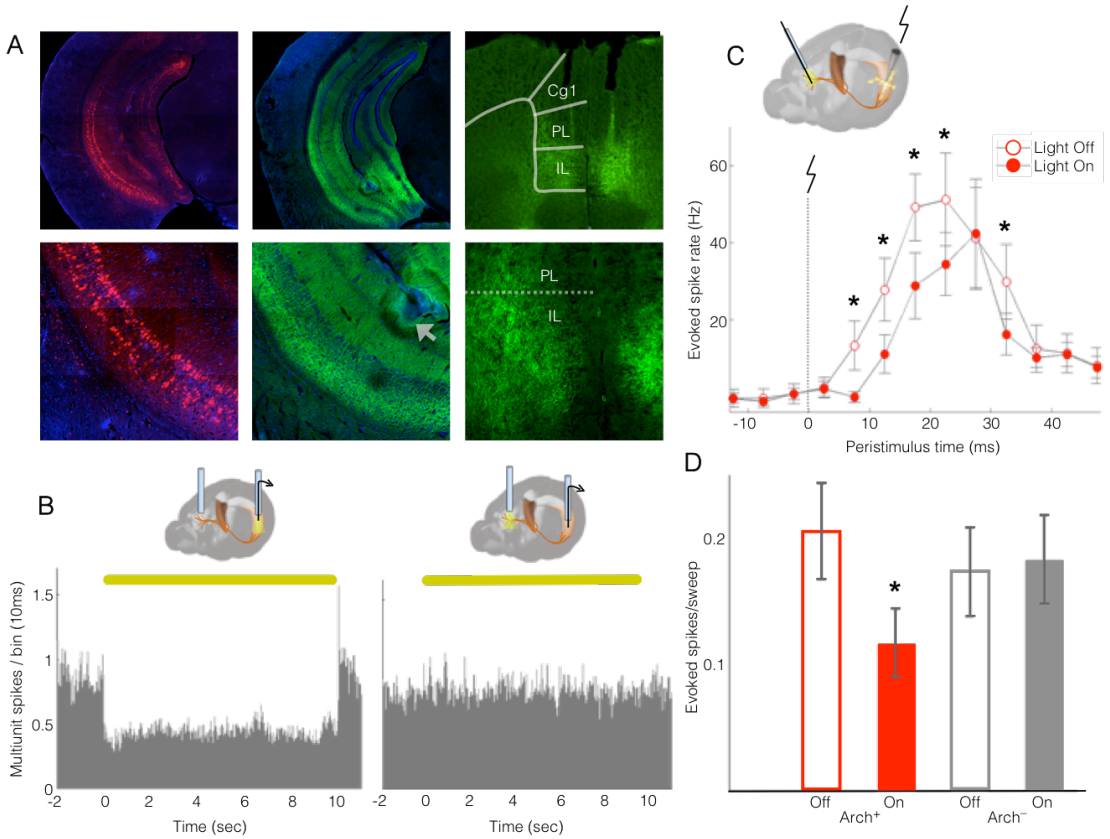

Figure 2.5 Optogenetically Mediated Inhibition of vHPC-mPFC Terminal Fields Impairs Projection-specific Signal Propagation but not Spontaneous Activity *in vivo*

(A) Expression of Arch and mCherry in mPFC-projecting cells of ventral Ca1. Six weeks following injection of CamKIIa-mCherry (left) and CamKIIa-eArch3.0-EYFP (center), robust fluorescent labeling was seen throughout ventral and intermediate Ca1. Arrow in lower center panel indicates the site of a lesion from a chronically implanted recording electrode in layer SLM. (Right) fluorescent axon terminals were visible in layers 2-6 of IL and 5-6 of PL regions of mPFC.

(B) Schematic and MUA traces from somatic and terminal field illumination *in vivo*. Arch-injected mice with chronically implanted optrodes in vHPC and fibers in mPFC (N=2) rested in their home cages during recording. Spontaneous activity in vHPC cells was robustly silenced by illumination of the vHPC (left) but not by illumination of mPFC terminal fields (right).

(C) Schematic diagram of acute experiment and evoked responses (5ms nonoverlapping bins, baseline rate = 6.1+/-0.14Hz). Robust evoked multi-unit responses to electrical stimuli in ventral Ca1 were seen in mPFC beginning 5-10ms, lasting 40ms, post-stim. When pulses were paired with terminal field illumination in Arch-expressing animals, a reduction in the evoked response was observed, particularly for early (putatively monosynaptic) latencies.

(D) Totals for arch-expressing and arch-negative controls. In Arch-expressing animals, but not in controls, illuminated of mPFC diminished the MUA response across the 5-40 ms post-stimulus (N = 16 sites across 3 animals, $t = 6.68$, $p = 0.0004$; $t = 1.57$, $p = 0.3$, respectively).

Chapter 3: Behavioral effects of modulating hippocampal-prefrontal input

3.1 Introduction

The dominant explanatory model of working memory in human psychology over the past 4 decades was originated by Alan Baddeley, whose work in primate prefrontal cortex in the 1970's provided some of the earliest evidence of so-called "memory cells", those which became active upon cue presentation and persisted through the delay period until a response was made (Baddeley and Hitch 1974, Baddeley 2003). A substantial body of research in primate as well as human and rodent models has extended from these initial findings and this model (Niki 1974, Niki and Watanabe 1976, Joseph and Barone 1987, Logie 1995, Miyake and Shah 1999, Andrade 2001, de Zubicaray, McMahon et al. 2001, Baeg, Kim et al. 2003, Curtis and D'Esposito 2004, Klauer and Zhao 2004, Jo, Park et al. 2007, Horst NK 2012, Miller 2013, Sreenivasan, Curtis et al. 2014). According to this conceptual framework, working memory requires 3 essential elements: a central executive, allocating attention and directing the contents of working memory to goal-directed action, a phonological loop, and a visuospatial sketchpad. Later findings of dissociability suggested that the visuospatial sketchpad may have distinct visual and spatial components (Logie 1995, Baddeley 2003, Klauer and Zhao 2004). Orthogonal to these modular cognitive components are phase components – information processed through working memory undergoes encoding, in which information is taken in through sensory pathways, maintenance, in which information is transiently held in an active state, and retrieval, in which it is applied toward motivated behavior.

For experiments requiring the use of rodent models of cognition, the study of phonological loops is challenging – while there is ample evidence for the use of vocalizations for communication in rodents (Arriaga, Zhou et al. 2012), it is unlikely to involved homologous circuitry to human speech and remains largely unexplored as a cognitive modality. Navigational capabilities in rodents, however, are highly developed – the robust tuning properties of entorhinal grid cells and hippocampal place cells provide strong evidence for the homology of this circuitry across mammalian systems (O'Keefe, Burgess et al. 1998, Burgess and O'Keefe 2003).

While spatial working memory in humans and primates is typically tested using keyboard and touch-screen paradigms, behavioral assays of spatial working memory in rodents typically involve spatial navigation to reward-associated goals – this has most often involved the H-maze, Figure-8 maze, or W-maze delayed spatial alternation (DSA) task, and the T-maze delayed non-match-to-place (DNMTP) task. DSA and DNMTP are distinct in that DNMTP features distinct encoding and retrieval trial phases, while DSA lacks such distinct phases (Dudchenko 2004).

A substantial body of literature implicates both hippocampus and prefrontal cortex in the successful execution of DNMTP tasks. Lesions of the mPFC results in impaired performance on such tasks involving delays between 0 and 25 seconds (Rogers, Wright et al. 1992, Shaw and Aggleton 1993, Lee and Kesner 2003, Sloan, Good et al. 2006, Izaki, Takita et al. 2008). Moreover,

previous work has shown that the joint contribution of medial prefrontal cortex (mPFC) and hippocampus (HPC) is critical to successful spatial working memory in rodents (Lee and Kesner 2003, Jones and Wilson 2005, Wang and Cai 2006, Hyman, Zilli et al. 2010, Sigurdsson, Stark et al. 2010).

Despite ample evidence for the necessity of mPFC in the successful performance of spatial working memory, the nature of this role is the subject of debate. It has been proposed that mPFC plays the role of a monitor, detecting changes in the environment and orchestrating the activity of structures that play a more direct role in fine-grained information coding (Andrade 2001, Horst NK 2012, Miller 2013), and alternatively that the mPFC itself encodes precise cue information, playing a more direct computational role in working memory (Euston, Gruber et al. 2012, Hymana, Maa et al. 2012). To better characterize the role of mPFC in SWM, and to assess the contribution of vHPC input to this role, we applied a projection silencing approach to reversibly inhibit vHPC-mPFC input during distinct phases of DNMTP trials.

3.2 vHPC-mPFC Terminal Inhibition Impairs Performance on a 2-Goal T-Maze Task

To assay working memory performance, a T-maze delayed non-match-to-place (DNMTP) task was employed. In this task each trial is divided into two phases; in the sample phase, one of the two goal locations is blocked by a wall, and the mouse is directed toward a food reward in the open location. In the

choice phase the wall is removed, and the mouse must select the opposite, previously closed arm in order to receive a second reward (Figure 3.1A). Arch-expressing mice, as well as control mice expressing an AAV-encoded fluorophore, were both trained to criterion in the task (see Methods). Following successful task acquisition, vHPC-mPFC terminal fields illumination was delivered either during the entire trial, sample phase only, or choice phase only. On each day of testing, mice received illumination trials of each type, along with no-light trials, and trial types were randomly interleaved.

Illumination of mPFC terminal fields in the *Entire Trial* or *Sample Light* condition was sufficient to impair task performance, while illumination in the *Choice Light* condition failed to affect performance (N = 6 control, N = 8 Arch animals; t = 3.96, p = 0.002; t = 2.98, p = 0.011; t = 1.1, p = 0.29, respectively). Performance was not affected by light for Arch-negative control animals in any condition (N = 8 and 6, respectively; ANOVA, virus-by-light interaction, F = 5.92, p = 0.02). Pairwise comparison of performance during illuminated trials relative to *No Light* trials revealed a decrease in performance for Arch animals in the *Entire Trial* (t = 4.9, p = 0.002) and *Sample On* conditions (t = 4.5, p =0.003) but not *Choice On* (t = 1.7, p = 0.125). There was no significant decrease in performance for Arch-negative animals trials in any of the illuminated trial types (t = 0.18, p = 0.87; t = 1.1, p = 0.3; t = 1.3, p = 0.25, respectively).

In Arch-expressing mice but not opsin-negative controls, performance was impaired by entire trial and sample phase illumination, but not by choice phase

illumination. These data raised the possibility that vHPC-mPFC input is critical for the encoding of location cues associated with sample goal but may not be required for the maintenance or retrieval of such cues.

3.3 vHPC-mPFC Terminal Inhibition During Encoding, not Maintenance or Retrieval, Impairs SWM Performance

This native version of the T-maze task, however, is not optimized to discriminate between encoding and retrieval, as the animal could begin forming a motor action plan (i.e. go into the opposite arm) any time after it encounters the sample goal. To better segregate the encoding, maintenance, and retrieval phases within trial, selection of the choice goal was temporally restricted to the choice run using a modified, 4-goal T-maze. Here, as in the 2-goal task, a single goal was made available for retrieval of the sample reward. Prior to the subsequent choice run, one of the three remaining doors would open (Figure 3.2A). This design prevents the mouse from formulating a spatially-directed action plan until the choice phase, when, at the end of its center arm run, it is presented with two of the four goals as options.

Baseline performance in this version of the T-maze was somewhat lower than the two-arm version, and animals did slightly worse when the sample and goal arms were in the same compared to the opposite direction (left vs. right) – nonetheless, performance remained well above chance for all trial types (Figure 2D). Animals performed better in the 4-goal task when sample and choice goals

differed in the left/right dimension than when they matched (N = 13 mice; mean = 0.71 +/- 0.02 and 0.65 +/- 0.01, respectively; t = -3.91, p = 0.001). However, performance on trials with left/right matching was significantly above chance (t = 4.0×10^{3}, p = 3.1×10^{-38}).

The effects of terminal inhibition confirmed the requirement for vHPC-mPFC input during encoding. Performance was impaired only in the Sample Light condition, while it was not impaired in the Delay Light condition or in the Choice Light condition (repeated here with either 10 or 20 second delays; Figure 3.2B). As in the 2-Goal task, performance was impaired in a task-phase selective manner for Arch-positive animals but not for Arch-negative animals (N = 7 and 6, respectively; ANOVA F = 3.74, p = 0.03; ANOVA F = 0.89, p = 0.47, respectively). Impairment was restricted to *Sample On* trials (t = 3.1, p = 0.0093), while *No Light* runs, *Delay On* runs and *Choice On* runs following both 10 and 20 second delays showed no impairment (t=1.1, p=0.29; t = 1.0, p = 0.34; t = 1.91, p = 0.08; t=1.2, p = 0.24, respectively). Pairwise comparison of performance between *No Light* runs and *Sample Light* runs also revealed a significant difference for Arch-positive animals (t = 2.5, p = 0.04) but not for Arch-negative animals (t = 0.35, p = 0.73). Moreover, performance during *Sample Light* runs was not significantly above chance level (t = 1.9, p = 0.11), though it was for *No Light, Delay,* and *Choice On* trials with both 10 and 20-second delays (t = 8.0, p = 2×10^{-4}, t = 6.1, p = 9.1×10^{-4}, t = 3.9, p = 0.008, t = 3.7, p = 0.009, respectively).

Together these experiments indicate that input from the vHPC to the mPFC is critical for encoding but not maintenance or retrieval of location cues in this task.

3.4 Discussion

In this study we used a projection silencing technique to reversibly interfere with direct HPC-mPFC input in a temporally and anatomically precise manner. We found that direct hippocampal input to the prefrontal cortex is essential for successful encoding of SWM-related cues. The finding of a dependence of task performance on vHPC input during sample runs, replicated across both behavioral paradigms used in this study, provides a strong argument for the importance of vHPC-mPFC afferent input during the phase of each trial in which relevant spatial cues are encoded. We furthermore find no significant effect of vHPC-mPFC terminal inhibition on performance during task phases concurrent with maintenance or retrieval of spatial cues. In light of multiple prior studies demonstrating the mPFC to be critically involved in SWM at delays less than or equal to those used here in the 4-goal experiment (Rogers, Wright et al. 1992, Shaw and Aggleton 1993, Lee and Kesner 2003, Sloan, Good et al. 2006, Izaki, Takita et al. 2008), the findings presented here argue that the critical window for vHPC-mPFC input is constrained to the encoding phase. In the 4-goal T-maze task used here, unlike with the spatial alternation task, choice goal is not fully determined by sample goal. While the animal may, during the delay phase, prepare to suppress a return to the sample goal, this anticipated action suppression does not fully determine an action plan. The task is therefore

uniquely suited to segregating cue encoding, maintenance, and retrieval. Our findings point to a role for the vHPC-mPFC afferent pathway as a conduit for the updating of SWM-critical location cues – this is in agreement with prior work implicating both vHPC and mPFC contextual learning (Fanselow and Dong 2010, Euston, Gruber et al. 2012, Hymana, Maa et al. 2012, Ruediger, Spirig et al. 2012, Komorowski, Garcia et al. 2013, Miller 2013).

3.5 Methods

Viral Transduction

AAV2/5 of titer exceeding 10^{12}vg/ml (UNC Vector core and UPenn Vector Core) was used to package all viruses. In the 2-goal t-maze experiment, a CamKIIα-eArch3.0-eYFP sequence was used to express the opsin and CamKIIα-mCherry was used as an opsin-negative control. For the 4-goal experiment, hSyn-eArch-eYFP and hSyn-eYFP were used for opsin and control, respectively. The hSynapsin promoter was chosen for the 4-goal experiment to account for possible long-range GABAergic vHPC-mPFC projections and to avoid potential toxicity effects resulting from opsin expression under the stronger CamKIIα promoter. Virus was targeted to multiple targets within stratum pyramidal of ventral Ca1 (2 mediolateral rows at AP 2.95 and 3.25, with sites at ML/DV: 2.65/4.5, 3.0/4.3, 3.35/3.9, 3.7/3.3-2.9. An additional row was made at AP 3.1, with ML/DV sites at 2.8/1.55 and 3.15/1.7. All coordinates reported in mm, all AP and ML w.r.t. bregma, DV w.r.t. brain surface. A 200nL bolus was delivered to

each site via glass micropipette (20-40μM diameter) at a rate of 100nL/min continuous infusion, with a wait time of 5 minutes between infusion and retraction.

Behavioral Training and Testing

Mice undergoing behavioral testing were given 5 weeks to recover from surgery, at which time they were placed on a food-restricted diet consisting of 1.5-2.5 grams of food per day as needed to maintain 85% of their post-recovery bodyweight. Mice were then given 2 days of habituation to the maze, which consisted of 10 minutes free exploration and foraging (plugged into optical fibers and recording tether) with all doors open, followed by 5 minutes of interleaved laser light pulses in the start box with doors closed (5-10sec on, 30sec off, 5 min). On the subsequent 2 days mice underwent behavioral shaping consisting of 10 minutes of running to baited goal arms in alternating directions. Mice then underwent training on the t-maze task until criterion performance, consisting of 70% correct trials on 2 out of 3 consecutive days) was achieved. Inter-trial delay was 20 seconds. On the 2-goal experiment, reward consisted of dustless pellets (Bio-Serv). To minimize across-session performance drift, we adjusted intra-trial delay according to the preceding day's performance, beginning at 10sec and adding 5 seconds of delay following days on which performance was above 80%. For the 4-goal experiment, reward consisted of sweetened condensed milk (~50μL, 3:1 dilution). To allow for direct comparison of delay within animal, intra-

trial delay was fixed at 10sec, with addition of a single session of 20sec delays as the final session for each animal. Light stimulation was 532nm, 10mW.

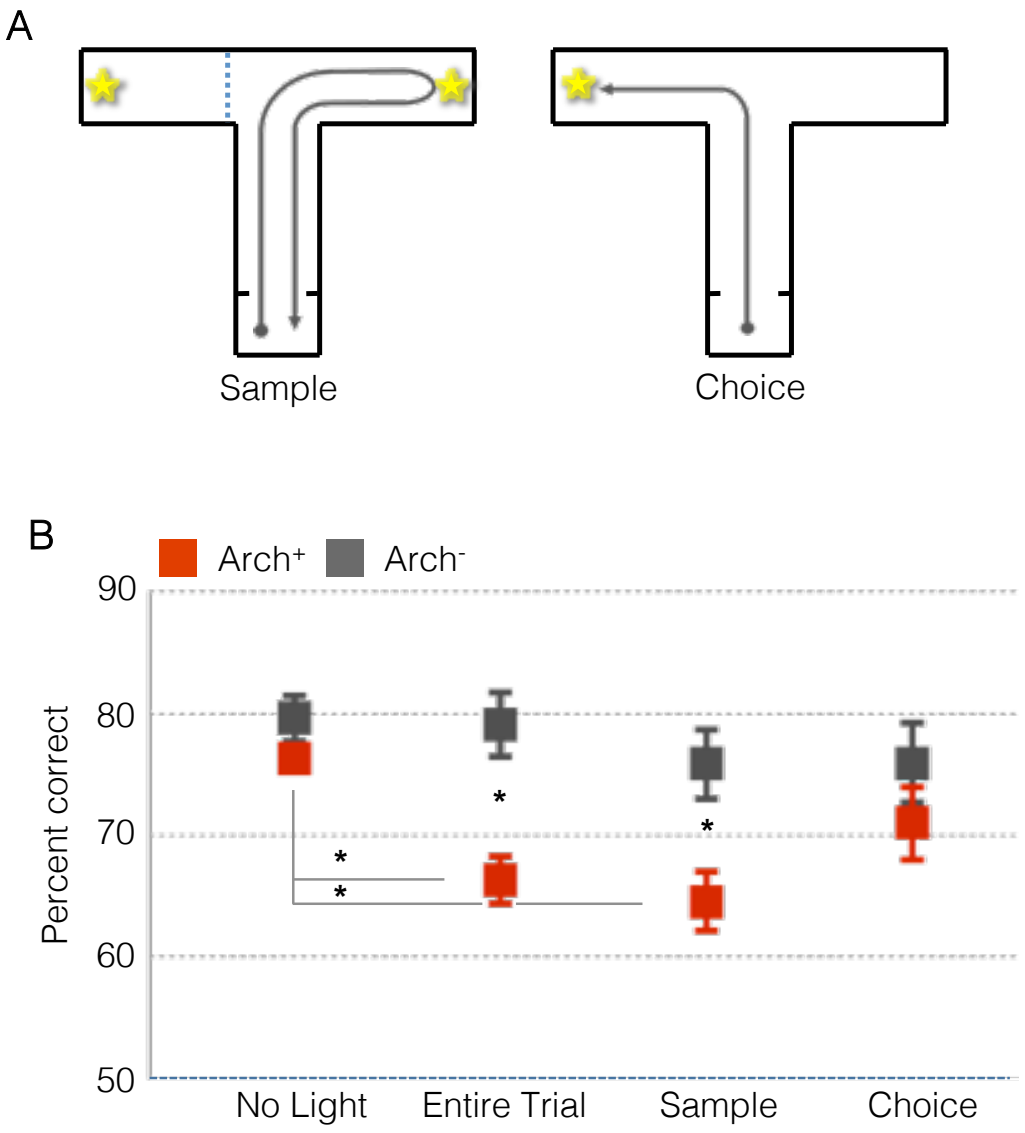

Figure 3.1 Inhibition of vHPC-mPFC Terminal Fields Impairs Performance in SWM-dependent Task

(A) Schematic of 2-Goal DNMTP task. The task was run in a standard T-maze configuration, in which a trial consisted of a forced-direction sample run to one of two rewards, followed by a choice run to the remaining reward.

(B) Task impairment with terminal inhibition during encoding. Illumination of mPFC terminal fields in the *Entire Trial* (t = 3.96, p = 0.002) or *Sample*

Light condition (t = 2.98, p = 0.011), was sufficient to impair task performance, while illumination in the *Choice Light* condition failed to affect performance (t = 1.1, p = 0.29). Performance was not affected by light for Arch-negative control animals in any condition (N = 8 and 6, respectively; ANOVA, virus-by-light interaction, F = 5.92, p = 0.02). Pairwise comparison of performance during illuminated trials relative to *No Light* trials revealed a decrease in performance for Arch animals in the *Entire Trial* (t = 4.9, p = 0.002) and *Sample On* conditions (t = 4.5, p =0.003) but not *Choice On* (t = 1.7, p = 0.125). There was no significant decrease in performance for Arch-negative animals trials in any of the illuminated trial types (t = 0.18, p = 0.87; t = 1.1, p = 0.3; t = 1.3, p = 0.25, respectively).

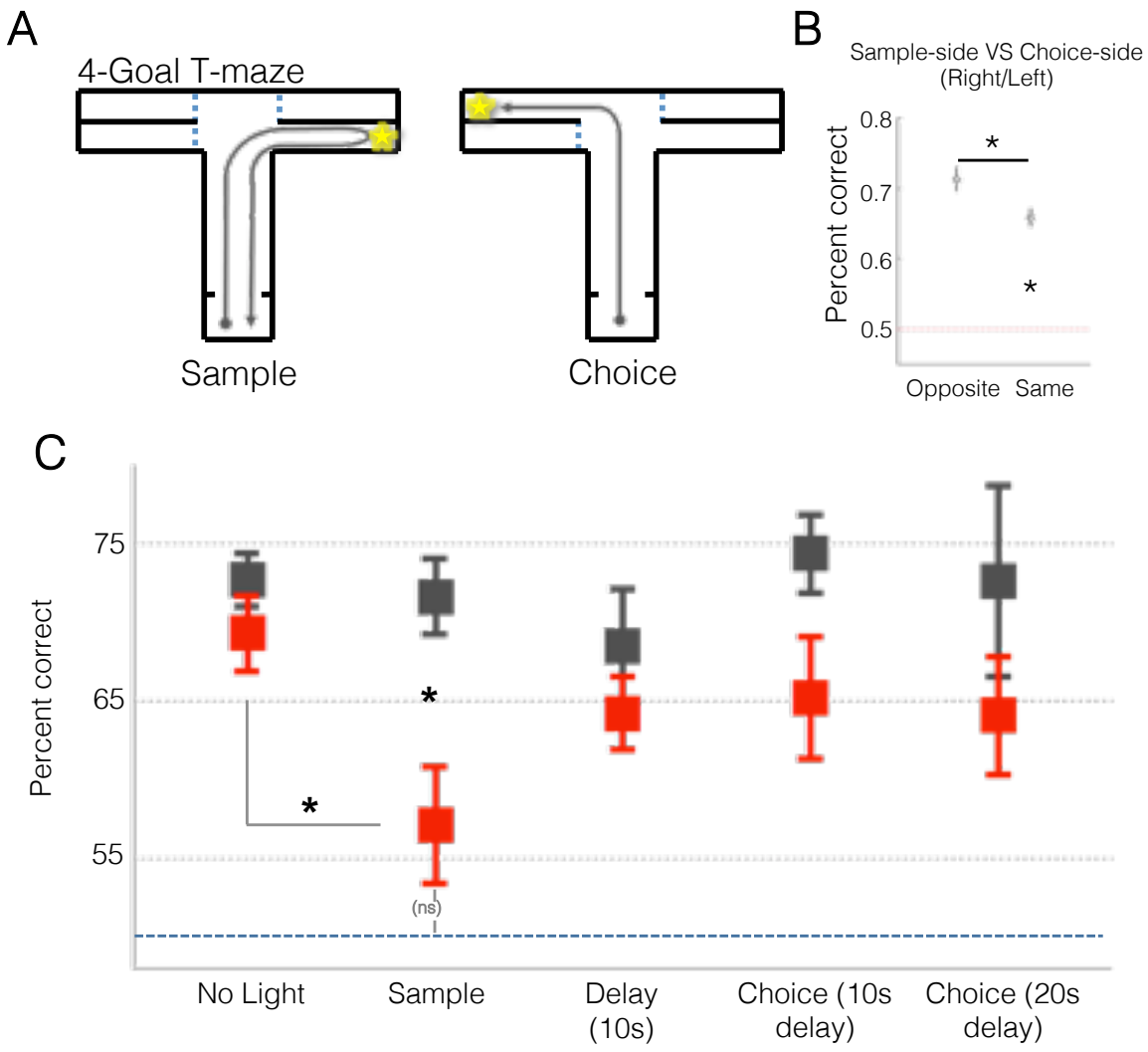

Figure 3.2 Inhibition of vHPC-mPFC Terminal Fields Impairs the Encoding, but not Maintenance or Retrieval, of Spatial Working Memory

(A) Schematic of 4-Goal DNMTP Task. For improved temporal segregation of encoding, maintenance, and retrieval phases, a modified 4-Goal configuration was used. As with the standard 2-Goal T-maze, Sample run consisted of a forced-direction turn into one of four goals.

(B) Task performance by sample-choice relationship. Animals performed better in the 4-goal task when sample and choice goals differed in the left/right dimension than when they matched (N = 13 mice; mean = 0.71 +/- 0.02 and 0.65 +/- 0.01, respectively; t = -3.91, p = 0.001). However, performance on trials with left/right matching was significantly above chance ($t = 4.0 \times 10^{3}$, $p = 3.1 \times 10^{-38}$).

(C) Task impairment with vHPC-mPFC terminal inhibition during encoding but not maintenance or retrieval. As in the 2-Goal task, performance was impaired in a task-phase selective manner for Arch-positive animals but not for Arch-negative animals (N = 7 and 6, respectively; ANOVA F = 3.74, p = 0.03; ANOVA F = 0.89, p = 0.47, respectively). Impairment was restricted to *Sample On* trials (t = 3.1, p = 0.0093), while *No Light* runs, *Delay On* runs and *Choice On* runs following both 10 and 20 second delays showed no impairment (t=1.1, p=0.29; t = 1.0, p = 0.34; t = 1.91, p = 0.08; t=1.2, p = 0.24, respectively). Pairwise comparison of performance between *No Light* runs and *Sample Light* runs also revealed a significant difference for Arch-positive animals (t = 2.5, p = 0.04) but not for Arch-negative animals (t = 0.35, p = 0.73). Moreover, performance during *Sample Light* runs was not significantly above chance level (t = 1.9, p = 0.11), though it was for *No Light, Delay,* and *Choice On* trials with both 10 and 20-second delays (t = 8.0, $p = 2 \times 10^{-4}$, t = 6.1, $p = 9.1 \times 10^{-4}$, t = 3.9, p = 0.008, t = 3.7, p = 0.009, respectively).

Chapter 4: Hippocampal-dependent representation of location cues by mPFC neurons

(Note: Analyses in this chapter involving a linear classifier were done in collaboration with Mattia Rigotti, Ph.D., in the lab of Stefano Fusi, Ph.D. at Columbia University.)

4.1 Introduction

Since the initial discovery of hippocampal place cells over 40 years ago (O'Keefe and Dostrovsky 1971), the role of the hippocampus in spatial navigation has been studied extensively and in fine spatial, temporal, and anatomical detail. Yet the vast majority of studies of the hippocampus in spatial navigation have focused on the dorsal/septal third of the structure. The dorsal hippocampus has been called the “cold” hippocampus, processing information supporting memory, navigation, and cognition in a manner relatively unbiased by emotional valence, while the ventral hippocampus has been called the “hot” hippocampus, critical for regulation of emotional states such as anxiety, stress, and fear (Fanselow and Dong 2010). This dichotomy is supported by studies showing that the dorsal hippocampus exhibits place representation in the absence of explicit motivation (O'Keefe and Dostrovsky 1971), while place fields in the ventral hippocampus are larger, less spatially resolved, and tend to correspond with salient spatial features, rather than Cartesian coordinates (Jung, Wiener et al. 1994, Poucet, Thinus-Blanc et al. 1994, Kjelstrup, Solstad et al. 2008, Royer, Sirota et al. 2010, Keinath, Wang et al. 2014). For example, the ventral hippocampus shows spatial periodicity in environments with spatially repeating features (Royer, Sirota et al. 2010). Nevertheless, despite the fact that the vHPC displays more abstracted

spatial representations than the “literal” representations seen in place cells of the dHPC, an animal’s spatial location can nevertheless be decoded with a high degree of accuracy from populations of simultaneously recorded vHPC cells (Keinath, Wang et al. 2014). Moreover, there is ample evidence that the vHPC is involved in spatial exploration (Fanselow and Dong 2010, Ruediger, Spirig et al. 2012, Komorowski, Garcia et al. 2013).

Like ventral hippocampus, cells of the mPFC exhibit coding for abstracted, behaviorally salient environmental features, rather than absolute location as seen in the dHPC (Jung, Qin et al. 1998, Hok, Save et al. 2005, Fujisawa, Amarasingham et al. 2008, Burton, Hok et al. 2009). Moreover, in some cases mPFC cells exhibit memory traces corresponding with previously observed stimuli. These “memory cells” have been demonstrated in primates performing working memory tasks; a subset of PFC cells will begin firing in response to a given stimulus, continue firing through the delay period, and stop firing as the animal performs a response (Fuster and Alexander 1971, Fuster 1973, Niki 1974, Niki and Watanabe 1976, Joseph and Barone 1987, Funahashi, Bruce et al. 1989, Sreenivasan, Curtis et al. 2014). In rodents, this phenomenon has proven elusive. In delayed spatial alternation tasks, PFC cells have been identified that correspond with both previous and future run trajectories (note that past and future trajectories are intertwined in spatial alternation) (Baeg, Kim et al. 2003, Horst NK 2012). However, when mPFC memory cells have been sought in DNMTP tasks, they have been notably absent (Jung, Qin et al. 1998).

We set out to elucidate the role of the mPFC in SWM by recording from multiple single units during the 4-goal T-maze task and examining spatial firing properties of cells both individually and at the population level. We hypothesized that, at the population level, the previously visited goal location should be decoded from aggregate population activity. We also wanted to clarify the role of vHPC input to mPFC SWM-related firing, hypothesizing that vHPC input should be essential to spatial coding during sample runs but not necessarily during choice runs.

4.2 mPFC Cells Encode Goal Location Both Categorically and Globally

The criticality of vHPC-mPFC input for the encoding of spatial working memory-related cues suggests that task-related spatial locations are encoded by specific mPFC firing patterns in a vHPC input-dependent manner. To test this hypothesis, optical fiber-coupled stereotrodes were used to obtain recordings of multiple single units in the prelimbic region of the mPFC in mice performing the 4-goal task. Activity in mPFC cells discriminated sample goal location (Figure 4.2A-C), with cells displaying varying degrees of mixed selectivity for the two spatial dimensions that distinguished goal arms (left/right, back/front; Figure 4.2C).

The percentage of cells that were goal-selective according to left/right, back/front, and combined spatial dimensions was modulated during the approach to the goal (Figure 4.2C). 2-way repeated measures ANOVAs were performed on binned spike rates (500ms windows, 100ms overlap) at successive peri-event

time points. The dashed line in figure 4.2C represents chance percentage. Across the population, cells showed preference for each spatial dimension individually, as well as for the interaction, suggesting a mixed selectivity of location coding among mPFC cells.

While some goal-modulated units displayed pure selectivity for a single spatial dimension (left/right, 20%; back/front, 8%), others had mixed selectivity for both dimensions, either in isolation (4%) or with interaction (14%).

4.3 Hippocampal Input is Required for Spatial Encoding in mPFC Units

Given this inhomogeneous and distributed nature of the representation of spatial information among recorded mPFC units, a maximum margin linear classifier (Anlauf and Biehl 1989, Meyers, Freedman et al. 2008, Barak and Rigotti 2011, Rigotti, Barak et al. 2013) was used to decode sample goal location from binned population rate vectors and quantify the strength and reliability of its neural encoding (Figure 4.3A-C). The classifier was trained on data from half of the trials, and model accuracy was tested on data from the remainder (see Methods).

Sample goal was decoded from spike histograms aligned to multiple trial events (Figure 4.3A), with model accuracy peaking in the temporal epoch that corresponded with arrival at the sample goal (Figure 4.3C). Sample goal representation at goal arrival time was then assessed in the presence and absence of inhibition of vHPC input by training the model on spikes from non-

Sample Light trials and testing on spikes from Sample Light trials. For eYFP-expressing animals, sample goal was decoded equally well with or without mPFC illumination, while in Arch-expressing animals accuracy was impaired by mPFC illumination (Figure 4.3D), demonstrating that vHPC input is critical for the representation of sample goal among mPFC cells during encoding. Decoding accuracy for Sample Goal upon arrival at the reward port was impaired by vHPC-mPFC terminal inhibition (269 Arch cells, 285 EYFP cells; N = 100 permutations; $t = 0.48$, $p = 0.64$ for EYFP; $t = 161.2$, $p = 1.2 \times 10^{-121}$ for Arch).

4.4 Hippocampal Input is Not Required for Episodic Encoding in mPFC Units

To assess the impact of terminal inhibition on encoding of non-spatial, task-relevant cues, the same classifier was used to decode task phase (sample vs. choice) at the time the start-box doors opened immediately prior to the run down the center arm. We reasoned that, because this epoch was behaviorally equivalent in sample and choice runs, a representation of task phase at this time point would rely upon a memory of the preceding task phase. In fact, task phase was decoded at this time point with near-perfect accuracy (Figure 4.4A). When the decoder was tested on choice runs from *Sample Light* trials, model accuracy was not affected for eYFP or Arch animals (Figure 4.4B), suggesting that vHPC-mPFC terminal inhibition interferes specifically with encoding of spatial

information pertaining to the goal location, and that it does not generally interfere with the encoding of other relevant task information.

Terminal inhibition did not affect encoding of episodic memory. When trained on trials with no light and tested on choice runs from Sample Light trials, accuracy remained high for both populations (0.96 and 0.95 for EYFP cells, 0.87 and 0.87 for Arch cells).

4.5 mPFC Cells Encode Choice Goal Location, and Not Sample Goal Location, During Choice Runs

During the subsequent delay period leading up to the choice run, sample goal could no longer be decoded (Figure 4.5A-B), arguing against the persistence of cue representation in the mPFC during the delay phase of this task. Instead, choice goal was decoded during choice run in a manner affected by trial outcome (Figure 4.5C-D). mPFC units also encoded trial outcome during choice running, with accuracy at decoding correct vs incorrect responses exceeding chance levels beginning 1 second prior to reaching the reward port.

4.6 mPFC Units Encode vHPC Input, though Not as a Change in Overall Firing Rate

The finding of vHPC input-dependent location coding in mPFC prompted the question of how location is encoded among mPFC cells. For example, vHPC

input could result in a location-specific firing rate increase, decrease, or a net-zero combination of the two. To answer this question, we first examined the effect of terminal inhibition on overall firing rate and found no change in eYFP or Arch animals. Firing rate during outbound running (points a-c from 4.3A) was unaffected by terminal field illumination in Arch or EYFP-injected animals (N = 474 cells, sign rank z = -0.23, p = 0.82; N = 418, z = -0.97, p = 0.33, respectively).

When putative pyramidal cells or interneurons were separated based on waveform features, putative FS and non-FS cells, sorted by spike width, showed no effect of terminal illumination on spike rate (EYFP Non-FS: sign rank z = -1.7, p = 0.095, EYFP FS: z = -1.6, p = 0.11; Arch Non-FS: z = -2.7, p = 0.79; Arch FS: z = -0.49, p = 0.62) (Figure 4.6A-C).

Despite the lack of overall change in firing rate due to vHPC-mPFC terminal inhibition, this inhibition could be decoded using our linear classifier 4.6D, suggesting the removal of vHPC input caused a shift in the pattern of firing rates across the mPFC population.

4.7 mPFC Units Show Hippocampal-dependent Location Selectivity During Encoding but Not Retrieval

Next, cells with high selectivity for sample goal were identified using weights generated by the classifier. These weights were also used to identify each cell's preferred goal, the goal in which firing rate was most different from

spiking in the other goals. This selection criterion deliberately left the sign of the rate differences intact, allowing for the possibility that any given unit might represent location by an increase or decrease in rate. Nevertheless, this difference was observed as an elevation in mean firing rate relative to other goals (Figure 4.8), and this elevation was particularly high for cells with high goal selectivity (Figure 4.7). During sample goal approach on *Sample Light* trials, high goal selective cells from Arch animals experienced a decrease in firing rate only when in the preferred goal, so that firing in preferred goals now equaled firing in non-preferred goals, while cells from eYFP animals were unaffected (Figure 4.7B). This change reveals an excitatory role for vHPC input in the location-selective firing of mPFC cells.

During choice runs, firing rate for high goal selective cells was also higher in the preferred goal than in non-preferred goals, but this elevation was unaffected by vHPC-mPFC terminal inhibition (Figure 4.7C), indicating that goal selectivity following encoding is no longer dependent on vHPC input.

4.8 Discussion

Here we have recorded from a large population of mPFC single units and found evidence of robust spatial representation in mPFC during both encoding and retrieval task phases. However, we found no evidence of retrospective coding for previously visited locations, either at the level of individual units or at the population level. Moreover, we find strong evidence that the contribution of

vHPC direct input to mPFC activity is critical for this spatial representation exclusively during the encoding phase of each trial, in close agreement with our behavioral findings of the necessity of this input for encoding but not retrieval (Chapter 4).

Using 2-way ANOVA, as well as a linear classifier, we find that the activity of mPFC units robustly represents the animal's contemporaneous location. This activity was observed as a goal-selective enhancement of firing in preferred goals, which depended on direct vHPC input. Moreover, while contemporaneous location was represented during both sample and choice runs, this representation depended on vHPC input only during the sample run. Here the physiology appears to agree with the behavioral observation that vHPC-mPFC input is critical for encoding, not retrieval, of task-relevant location cues.

Interestingly, using the same linear classifier that was highly accurate in decoding the mouse's contemporaneous location in both sample and choice runs, we find no evidence of retrospective location coding in mPFC activity. Within the parameters of this study, this appears to rule out persistent firing within mPFC as a means of maintaining the stimulus representation between encoding and retrieval. Retrospective and prospective location encoding have been seen in mPFC cells of rodents during delayed spatial alternation tasks in which past and future location are intertwined, and in which the rodent may form an action plan during the delay period (Baeg, Kim et al. 2003, Horst NK 2012), while in primates there is ample evidence for stimulus-specific delay-period firing in dorsolateral

prefrontal cortex, homologous to rodent PL (Fuster and Alexander 1971, Fuster 1973, Niki 1974, Niki and Watanabe 1976, Joseph and Barone 1987, Funahashi, Bruce et al. 1989). But in an 8-arm radial maze SWM task, in which an animal freely chooses a sequence of goal visitations, retrospective place firing has been shown to be notably absent in rodent mPFC (Jung, Qin et al. 1998).

In the 4-goal T-maze task used here, unlike with the spatial alternation task, choice goal is not fully determined by sample goal. While the animal may, during the delay phase, prepare to suppress a return to the sample goal, this anticipated action suppression does not fully determine an action plan. The task is therefore uniquely suited to segregating cue encoding, maintenance, and retrieval. Beyond the behavioral result itself, we consider the lack of retrospective place firing as additional validation that SWM cognitive phases (encoding, maintenance, retrieval) are temporally distinct in this task.

The combined results that vHPC-mPFC input is necessary only during location encoding, that mPFC lacks retrospective location representation during maintenance and retrieval, and that mPFC representation of contemporaneous location during retrieval is not vHPC input-dependent suggests that mPFC processes sample goal location transiently and that some downstream structure(s) may maintain the information thereafter. Likely candidate structures would include dHPC (by way of entorhinal cortex) and the thalamic nucleus reuniens. We cannot, however, rule out the possibility that retrospective location is persistently represented in the mPFC in a form not decodable from spike rates

alone, such as temporary changes in synaptic weights, or reactivation of retrospective spatial representations that are transient and not well aligned to trial events.

4.9 Methods

Recording and Spike Sorting

Recordings were amplified, band-pass flitered (1-1000Hz LFPs, 600-6000Hz spikes), and digitized using the Neuralynx Digitcal Lynx system. LFPs were collected at a rate of 2kHz, while spikes were detected by online thresholding and collected at 32kHz. Units were initially clustered using Klustakwik (Ken Harris), sorted according to the first two principal components, voltage peak, and energy from each channel. Clusters were then accepted, merged, or eliminated based on visual inspection of feature segregation, waveform distinctiveness and uniformity, stability across recording session, and ISI distribution. Recording sites were validated by histological examination of electrothermolytic lesions performed pre-perfusion (50μA, 20sec).

Spike Analysis Using a Linear Classifier

Analysis using the population decoder was performed on binned spike vectors (500ms bins, 100ms increments) of all recorded cells from sessions with

at least 2 trials for each feature class under consideration. As in previous work with spike data from prefrontal cortex, we therefore took advantage of the accumulated data to decode task-relevant features by treating all cells as a single, pseudosimultaneously recorded population (Meyers, Freedman et al. 2008, Machens, Romo et al. 2010). This approach assumes equivalent spike statistics across animals and recording sessions, and ignores potential contributions to population coding from correlated spike variability that would be observed if all cells were indeed simultaneously recorded (Abbott and Dayan 1999).

Model training was performed using constrained quadratic programming (Anlauf and Biehl 1989, Barak and Rigotti 2011) that employed a maximal margin perceptron (Rosenblatt 1962, Krauth and Mezard 1987, Anlauf and Biehl 1989). The training samples to this algorithm are generated by averaging the recorded spike counts within the relevant conditions that need to be decoded, and across a specified training set of trials. This procedure gives a mean activity vector per condition, where each component of the vector represents the trial-averaged activity of a given neuron at a given condition (Figure 4.9). The quadratic programing procedure then aims at finding a set of readout weights that maximally separate the mean activity vectors corresponding to the conditions that have to be discriminated. Multi-class discrimination problems are reduced to a set of binary discrimination problems involving all pairwise combinations of conditions (Dietterich and Ghulum 1991).

The model is then tested by cross-validating its performance on a test set of recorded trials. Given a task condition, a test vector is generated by sampling its components from the distribution of spike counts recorded from the corresponding neuron during the test trials. At each test phase 100 test vectors per condition are randomly resampled with replacement, and the performance of the model is quantified as the average accuracy in classifying them. For each time bin, model training and testing was performed 100 times (at which point estimates of model accuracy approached asymptote) on non-overlapping subsets of trials (half of trials to train, half to test, random subsampling without replacement), with subsets constrained to include at least one trial corresponding with each feature class under consideration. For training and testing across separate trial conditions (Figure 4), the same trial number requirement was applied across training and testing sets to ensure equal population sizes and equal representation of feature classes in the two trial sets.

For identification of each cell's preferred goal, absolute values of model weights for each goal's 3 binary classifications (comparison with each other goal) were summed, and the goal with the highest summed value was judged to be the preferred goal. To segregate cells with high and low goal selectivity, the absolute model weights for all 6 binary classifications (each goal-goal comparison) were summed; cells in the upper and lower quintiles were judged to have high and goal selectivity, respectively.

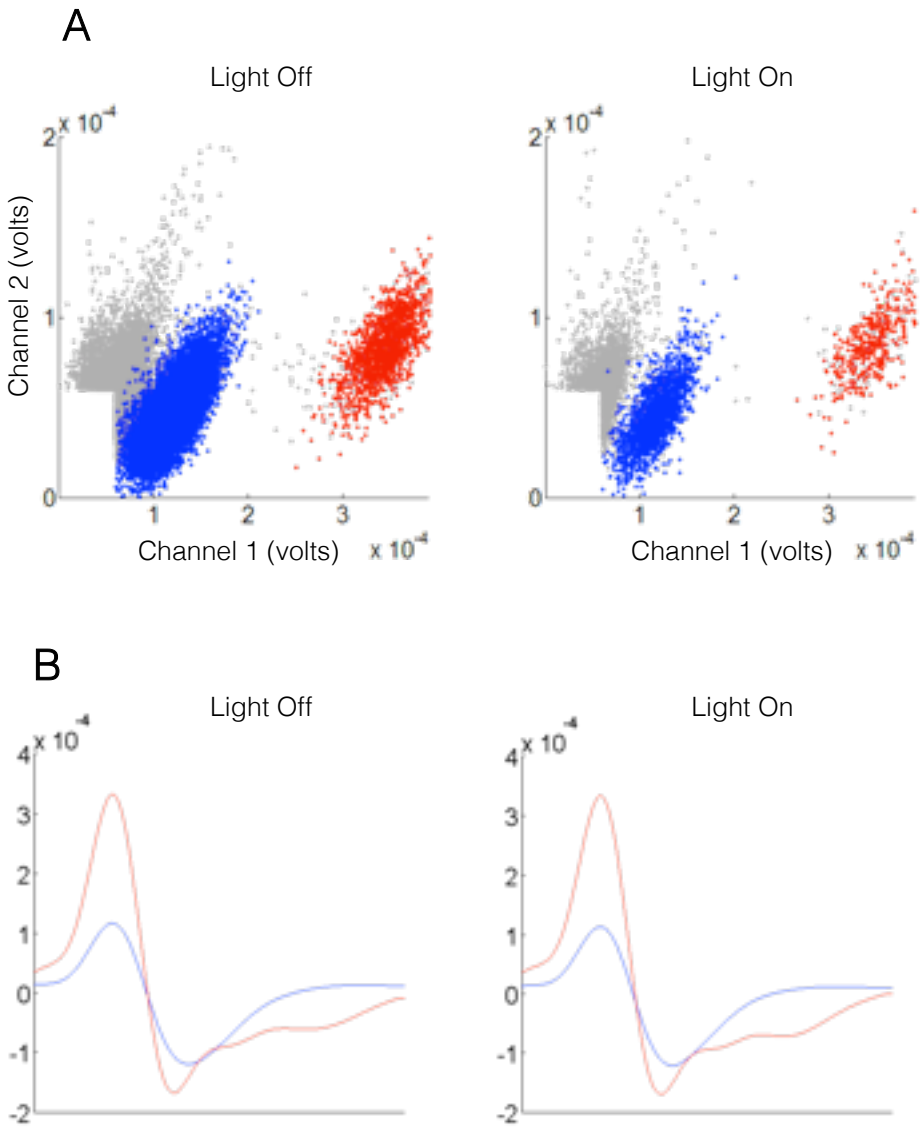

Figure 4.1. Individual mPFC Unites Clustered from Fiber-Coupled Stereotrodes.

(A) Multiple individual units clustered from stereotrode recordings in mPFC in the absence and presence of illumination.

(B) Mean waveforms from cells in (A)

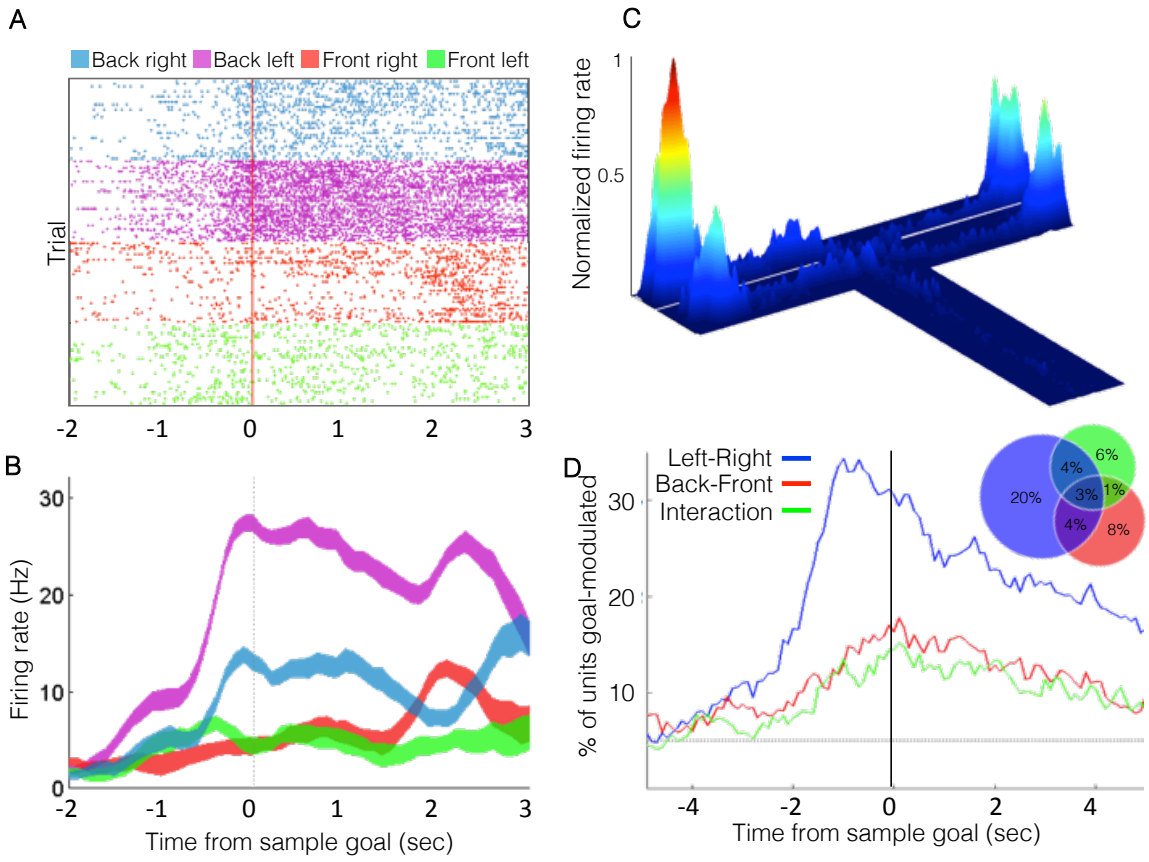

Figure 4.2 mPFC Cells Encode Goal Location Both Categorically and Globally

(A) A rastor plot of spikes fired by a cell across trials, sorted by sample goal, temporally aligned to arrival at sample goal.

(B) Mean and SEM traces of firing rates from all trials for the cell from (A). The cell shows location selectivity, firing preferentially in the Back Right goal.

(C) Place map for the same cell for the full recording session. Goal-selective cells tended to fire more at the preferred goal than at the other goals, and more at all goals than in the rest of the environment.

(D) Percentage of cells that were goal-selective according to left/right, back/front, and combined spatial dimensions. 2-way repeated measures ANOVAs were performed on binned spike rates (500ms windows, 100ms overlap) at successive peri-event time points. Dashed line represents chance percentage. Across the population, cells showed preference for each spatial dimension individually, as well as for the interaction, suggesting a mixed selectivity of location coding among mPFC cells. (Upper right) Venn diagram of overlap among cells from the left panel at time zero (arrival at goal). Percentages are out of all recorded units. While some goal-modulated units displayed pure selectivity for a single spatial dimension (left/right, 20%; back/front, 8%), others had mixed selectivity for both dimensions, either in isolation (4%) or with interaction (14%).

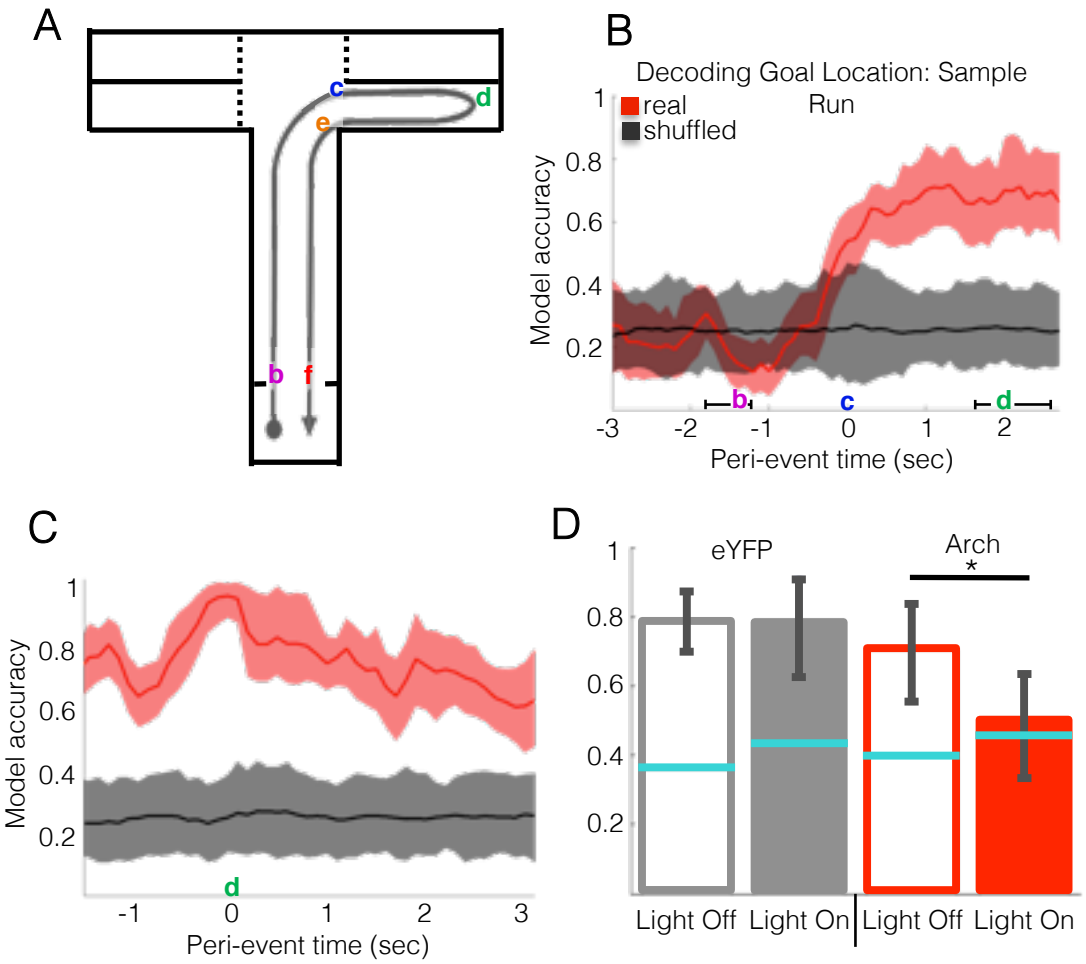

Figure 4.3 Hippocampal Input is Required for Spatial Encoding in mPFC Units.

(A) Schematic of Run Sequence. Spike data from all isolated mPFC cells was structured as peri-event spike histograms centered on key events during task running: Leaving start box (a), entering goal arm (b), reaching goal port (c), leaving goal arm (d), and returning to start box (e).

(B) Entering Sample Goal. Sample Goal identity was decoded from the mPFC population well above chance from the time the animal enters the intersection.

(C) Reaching Sample Goal. Decoding accuracy peaks at 0.96 upon arrival at the reward port.

(D) vHPC-mPFC Terminal Inhibition Reduces Sample Goal Representation. Decoding accuracy for Sample Goal upon arrival at the reward port was impaired by vHPC-mPFC terminal inhibition (269 Arch cells, 285 EYFP cells; N = 100 permutations; t = 0.48, p = 0.64 for EYFP; t = 161.2, p = 1.2×10^{-121} for Arch). Error bars represent 95% confidence intervals for real data, blue lines represent upper bounds of 95% confidence intervals for shuffled data.

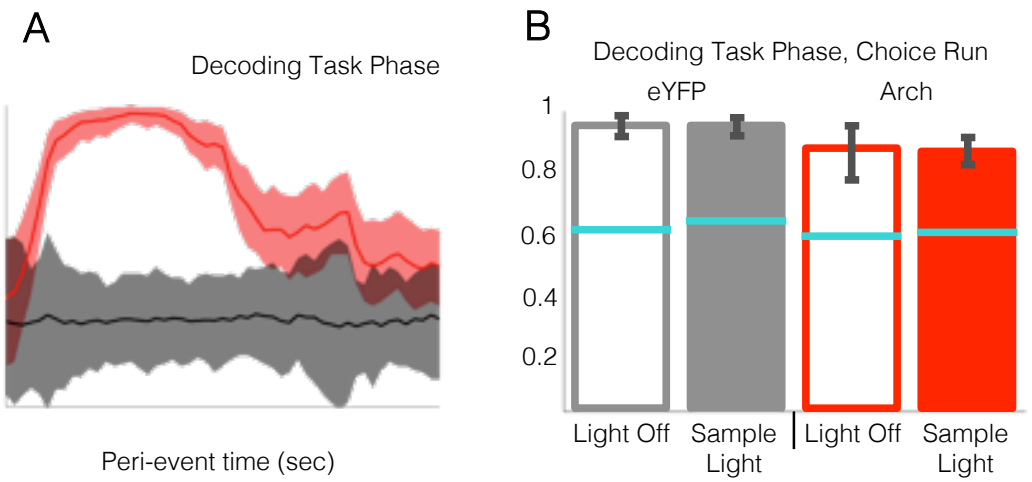

Figure 4.4 Hippocampal Input is Not Required for Episodic Encoding in mPFC Units.

(A) Task phase (sample vs. choice) was decoded with near perfect accuracy (0.98), revealing a memory trace for the preceding task phase (previous trial's choice run for sample, and current trial's sample run for choice), which peaked 1.2s prior to leaving the start box, concurrent with the opening of the start box doors (a).

(B) Terminal inhibition did not affect encoding of episodic memory. When trained on trials with no light and tested on choice runs from Sample Light trials, accuracy remained high for both populations (0.96 and 0.95 for EYFP cells, 0.87 and 0.87 for Arch cells).

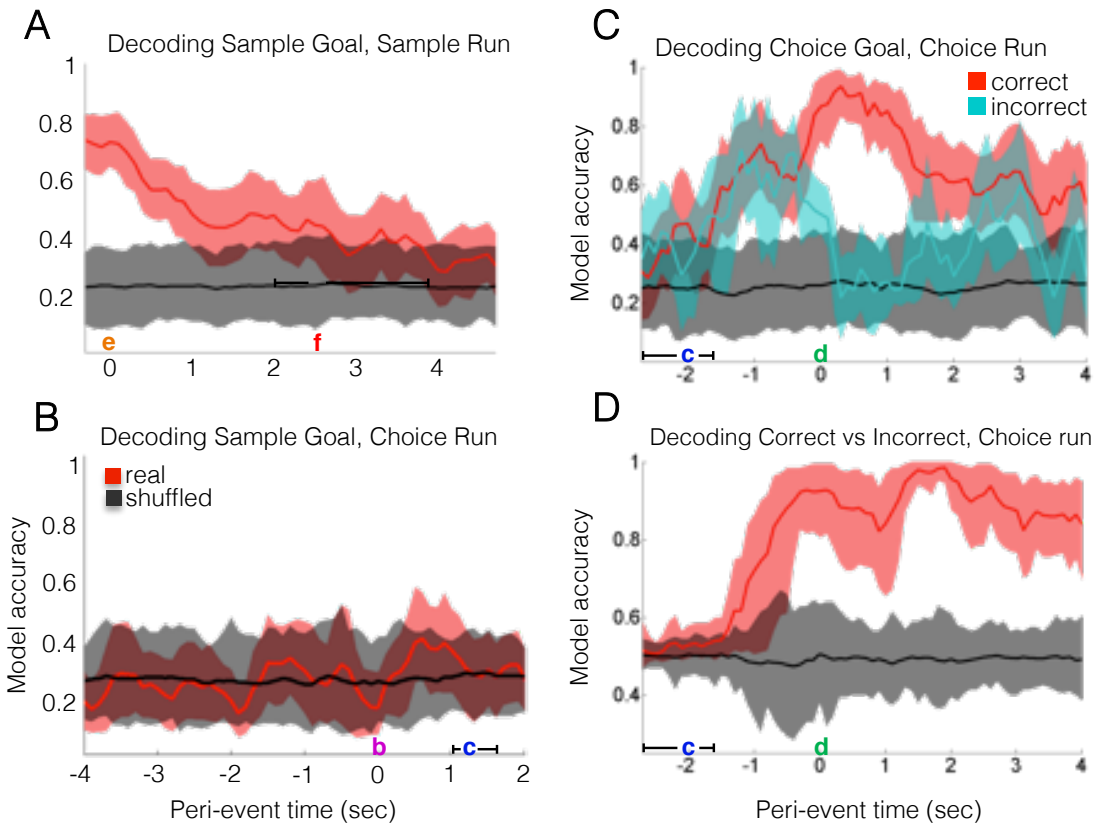

Figure 4.5 mPFC Cells Encode Choice Goal Location, and Not Sample Goal Location, During Choice Runs.

(A) Decoding accuracy declined as the animal leaves the Sample Goal and returns to the Start Box.

(B) Decoding Sample Goal location during subsequent Choice run. Using the linear decoder, previously visited location was not detectable above chance accuracy. Histograms aligned to departure from start box.

(C) Decoding Choice Goal during Choice run, correct VS incorrect trials. Location decoded was chosen goal, (i.e., the mouse's current location) rather than correct goal. Model accuracy reached 0.93 upon arrival at the

goal on correct trials. On incorrect trials, model accuracy was similar to that from correct trials during goal approach but dropped to chance levels upon reaching the goal.

(D) Decoding choice accuracy (correct VS incorrect) during choice trials. Model accuracy was nearly perfect, peaking at 0.99 at 1.9 seconds following arrival at the goal.

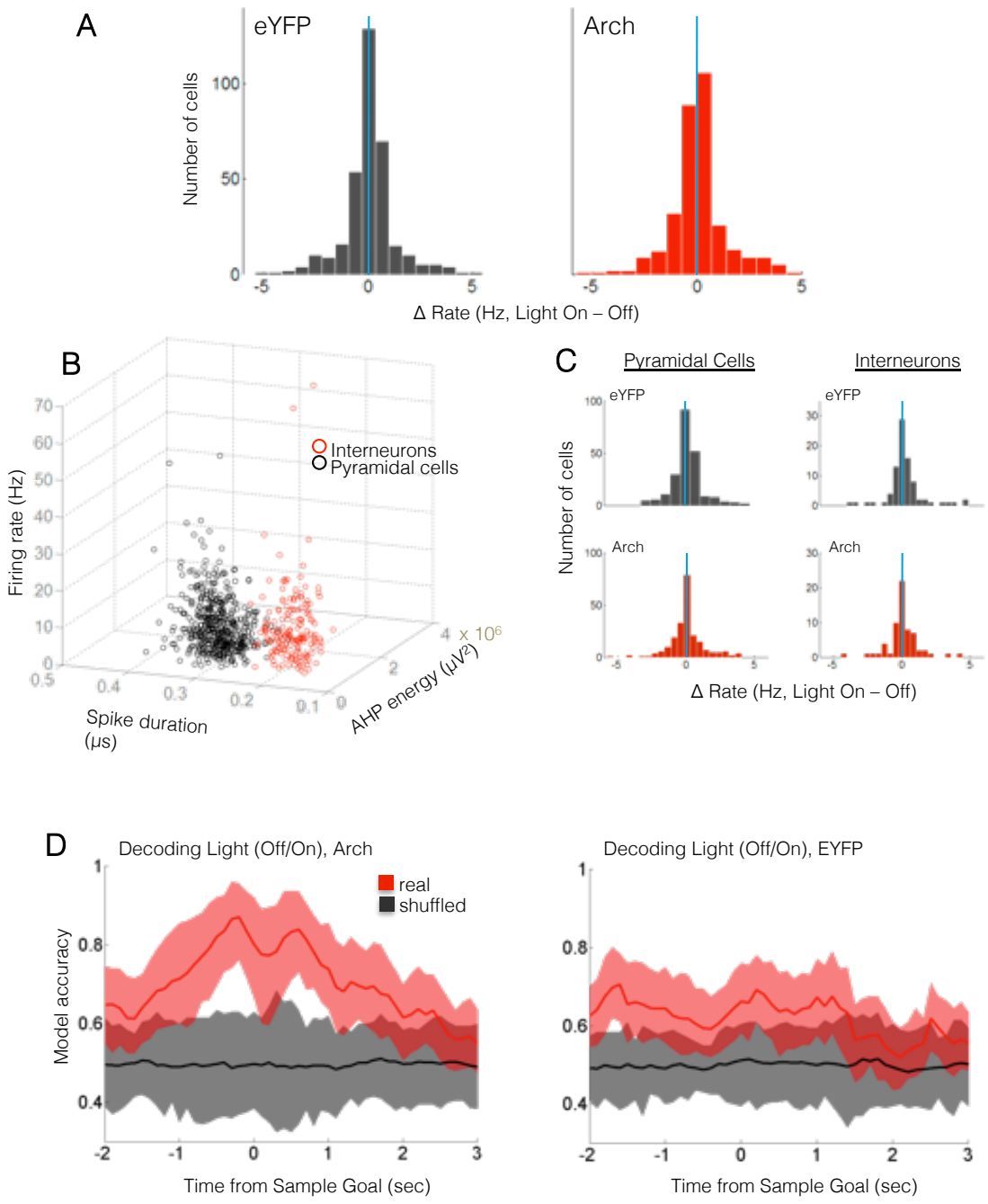

Figure 4.6 vHPC-mPFC Terminal Inhibition Changes the mPFC Population-wide Activity Profile but Not Overall Firing Rate

A. Terminal inhibition does not affect overall spike rate among mPFC cells. Firing rate during outbound running (points a-c from 5A) was unaffected by

terminal field illumination in Arch or EYFP-injected animals (N = 474 cells, sign rank z = -0.23, p = 0.82; N = 418, z = -0.97, p = 0.33, respectively).

B. Waveform features used to separate putative cell types. Spike duration was defined as the peak-to-trough time, while afterhyperpolarization (AHP) energy was taken as the area over the curve following the second zero-crossing. Spike duration yielded the clearest separation.

C. mPFC spike rates remain unaffected when sorted by putative cell type. Putative FS and non-FS cells, sorted by spike width, showed no effect of terminal illumination on spike rate (EYFP Non-FS: sign rank z = -1.7, p = 0.095, EYFP FS: z = -1.6, p = 0.11; Arch Non-FS: z = -2.7, p = 0.79; Arch FS: z = -0.49, p = 0.62).

D. mPFC Population Activity Encodes vHPC Terminal Inhibition. Using a maximum margin linear classifier, light presence was decoded from peristimulus spike histograms temporally aligned to goal arrival (500ms windows, 100ms overlap). Shaded areas indicate 95% confidence intervals across model iterations. The presence of light was decoded above chance for both EYFP-injected and Arch-injected animals, though with considerably higher accuracy in the Arch group. EYFP peak accuracy was 0.7 (200ms post to goal arrival), while Arch peak accuracy was 0.87 (200ms prior to goal arrival), and decoding accuracy at both timepoints was significantly higher for the Arch group (414 EYFP cells, 378 Arch

cells, N = 100 model iterations, t = -122, p = 10.0×10^{-110} first timepoint, t = -24.7, p = 4.6×10^{-44} second timepoint).

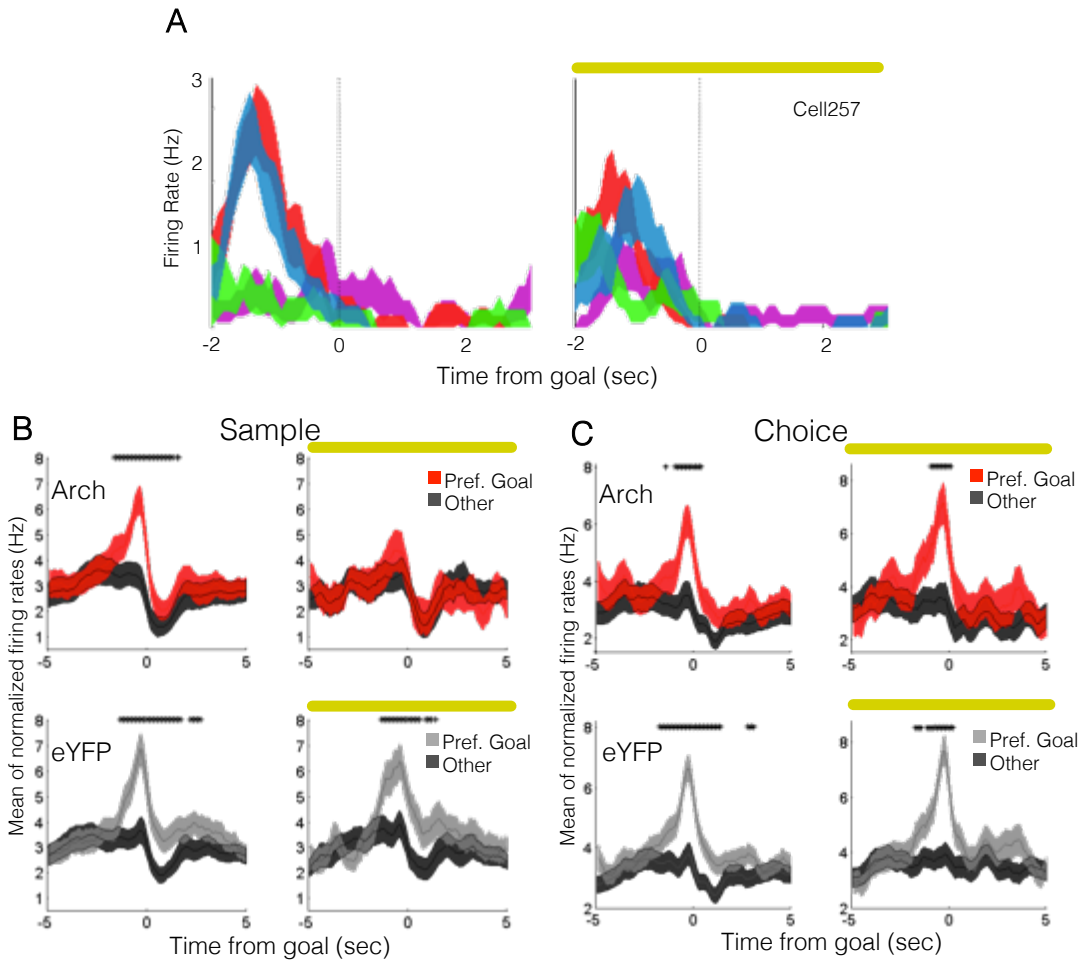

Figure 4.7 mPFC Units Show Hippocampal-dependent Location Selectivity During Encoding but Not Retrieval

(A) Example of selectivity modulation by terminal inhibition. (Left Panel) On Sample runs with no light, firing rate is greater in left than in right goals. (Right Panel) During *Sample On* trials, selectivity is degraded.

(B) Terminal inhibition eliminates firing rate differences in preferred VS non-preferred goal during encoding. Traces indicate mean +/-SEM of normalized firing rate (bin FR – session FR) for cells with high location selectivity, defined as those with model weights in the upper quintile at the

time of goal arrival (note that even for non-preferred goals, firing rate is higher than session mean). On Sample runs with no light, cells from both EYFP (Upper Left) and Arch animals (Lower Left) show elevated firing rates in preferred goal relative to non-preferred goal (black asterisks mark timepoints with Bonferroni-corrected significance). In *Sample Light* runs, cells from EYFP animals maintain elevated firing in the preferred goal (Upper Right), while cells from Arch animals show no significant firing rate difference (N = 78 EYFP cells, 67 Arch cells, Sign rank $p < 0.0005$).

(C) Terminal inhibition does not affect firing rate differences in preferred VS non-preferred goal during retrieval. As in Sample runs, cells from both EYFP (Upper Left) and Arch animals (Lower Left) show elevated firing in the preferred Choice goal during Choice runs. In *Choice On* trials, firing in cells from both EYFP and Arch animals remained significantly elevated (N = 145 EYFP cells, 77 Arch cells, Sign rank $p < 0.0005$).

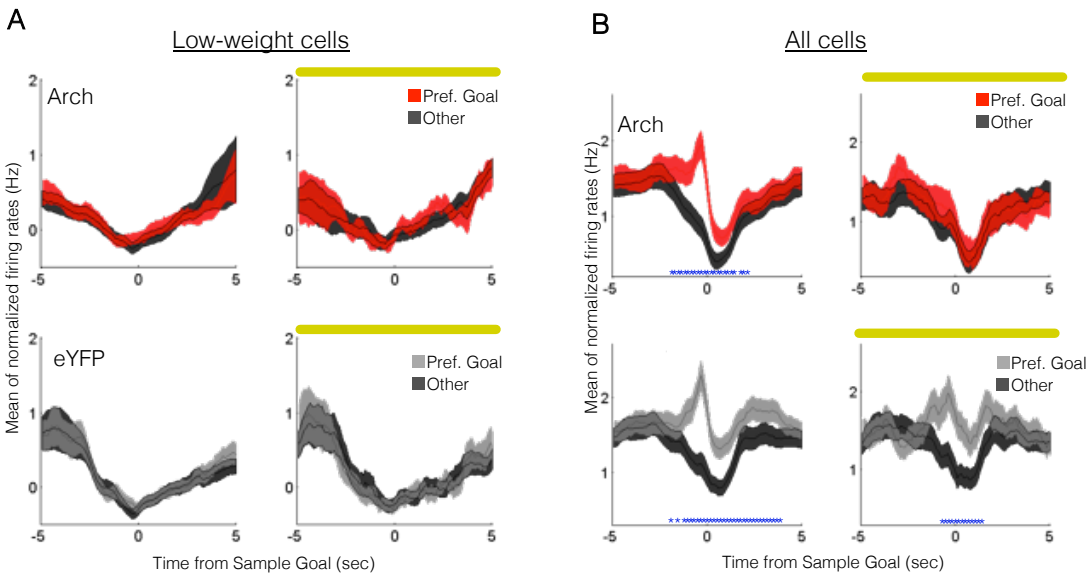

Figure 4.8 Effect of mPFC Illumination on Goal-Selective Firing in mPFC

(A) Low-weighted cells, as identified using the classifier, show no difference in firing between the goal with the highest weight relative to the other goals. Moreover, in the sample goal these cells fire at rates not different than their session mean rates. Traces indicate mean +/-SEM of normalized firing rate (bin FR – session FR).

(B) Terminal inhibition eliminates firing rate differences in preferred VS non-preferred goal during encoding across all cells. On sample runs with no light, cells from both EYFP (Upper Left) and Arch animals (Lower Left) show elevated firing rates in preferred goal relative to non-preferred goal (red asterisks mark time points with Bonferroni-corrected significance). In *Sample Light* runs, cells from EYFP animals maintain elevated firing in the preferred goal (Upper Right), while cells from Arch animals show no

significant firing rate difference (N = 358 EYFP cells, 325 Arch cells, Sign rank $p < 0.0005$).

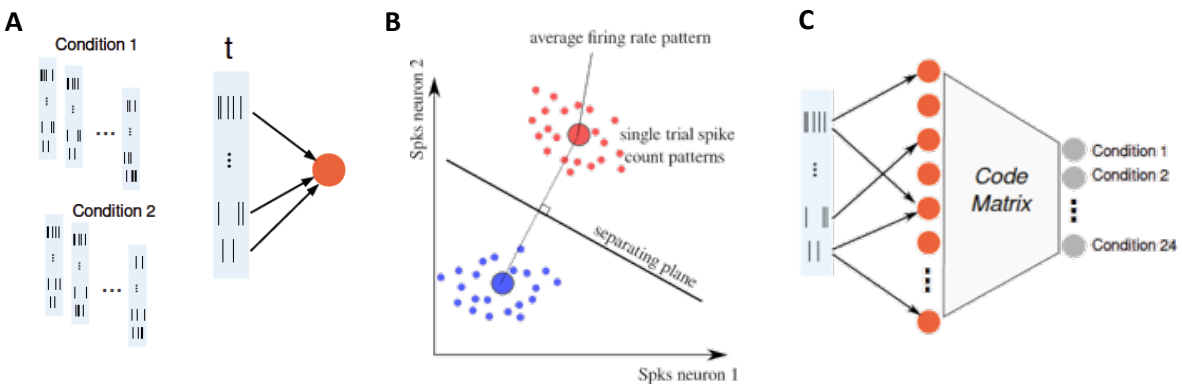

Figure 4.9 Schematic of decoder training and testing (Rigotti, Barak et al. 2013)

(A) For half of all session trials, binned spike rates for each peristiumulus time bin *t* are used to train a decoder to discriminate between condition pairs. A perceptron is generated for each condition pair.

(B) Separation boundaries are drawn in N-dimensional space, where N is the number of recorded neurons. Support vectors are established to maximize the distance between the trial-averaged spike rates in this space.

(C) The classifier is tested on spike rates from all trials not used for training. A code matrix is applied to the population rates, weighting neurons with strong class discrimination higher than those with weak class discrimination. Outputs from all perceptrons are collapsed into a single multi-class prediction.

Chapter 5: Gamma but not theta oscillations mediate vHPC-mPFC input during spatial working memory

5.1 Introduction

Rhythmic oscillations in aggregate postsynaptic potentials (typically referred to as local field potentials or LFP) and in neuronal spiking have long been hypothesized to facilitate the temporal coordination of activity across distant assemblies of neurons (Milner 1974, von der Malsburg 1981, Gray and Singer 1989, Buzsaki 2006). Oscillations in two specific frequency bands in particular, the theta and gamma bands (4-12Hz and 30-70Hz, respectively) have been associated with effective cognitive processing in both hippocampal and cortical regions. Synchronization of theta oscillations between dHPC and mPFC are associated with successful working memory performance and have been hypothesized to synchronize via vHPC (Jones and Wilson 2005, Siapas, Lubenov et al. 2005, Sigurdsson, Stark et al. 2010, O'Neill, Gordon et al. 2013). Gamma oscillations in primate mPFC have been shown to modulate the timing of cue-sensitive neurons (Siegel, Warden et al. 2009), and gamma oscillations in hippocampus are associated with the successful execution of spatial working memory in the T-maze (Yamamoto, Suh et al. 2014). Using multisite recordings in dHPC, vHPC, and mPFC, we examined the role of theta and gamma synchrony in the hippocampal-prefrontal pathway and its relevance to spatial working memory.

5.2 mPFC Units are Not Directionally Modulated by vHPC Theta Oscillations

LFPs recorded from dHPC, vHPC and mPFC exhibit prominent theta (4-12Hz) and gamma (30-70Hz) rhythms (Figure 5.2). Synchrony in these frequency ranges can be used as a measure of functional connectivity and has been linked by prior studies to working memory (Jones and Wilson 2005, Sigurdsson, Stark et al. 2010, Yamamoto, Suh et al. 2014). To assay functional connectivity, the degree to which spiking in one brain region synchronizes with LFP oscillations in a second brain region was examined using Rayleigh's test, a measure of the *significance* of phase non-uniformity, and pairwise phase consistency (PPC), a measure of the *magnitude* of phase non-uniformity. To determine the temporal directionality of synchronous activity, we performed lag analysis, in which phase-locking was measured at various temporal shifts; preferential phase-locking at a nonzero We first examined theta and found that a large subset of mPFC cells significantly phase-locked to theta in both dHPC and vHPC during runs toward goals in the T-maze (49% and 40% at zero lag, respectively Figure 5.3A,D). Surprisingly, despite the anatomical unidirectionality of vHPC-mPFC projection, mPFC cells did not phase-lock preferentially to vHPC theta of the past. mPFC cells that significantly phaselock are equally strongly phaselocked to vHPC Theta of the past and future, indicating a lack of temporal directionality (N = 189 cells, z = 2.05, p = 0.98). Moreover, examination of the mean PPC value among phase-locked cells revealed no temporal directionality, further supporting the conclusion that mPFC cells are not influenced by vHPC theta. If any directionality did exist, it

appeared as a non-significant trend toward preferred phase-locking of mPFC cells to vHPC theta of the future.

5.3 mPFC Units are Directionally Modulated by dHPC Theta Oscillations

Unlike with vHPC theta, mPFC cells preferentially phase-locked to dHPC theta of the past (Figure 5.3D-F), as has been reported in previous work (Siapas, Lubenov et al. 2005, Sigurdsson, Stark et al. 2010), supporting the idea that theta-frequency input from the dHPC influences mPFC spike timing. Among mPFC cells that significantly phase-lock to dHPC Theta (Bonferonni-corrected significance within the -200 to 200ms lag window), a higher number phase-lock maximally at lags at which mPFC spiking corresponds with the dHPC signal of the past (N=160 cells, Sign rank $z = -4.4$, $p = 6 \times 10^{-6}$). Examination of the mean PPC value across lags for mPFC cells phase-locked to dHPC theta also revealed a lag, mean PPC value peaking with dHPC theta from 20-25ms in the past.

5.4 vHPC Units are Driven by mPFC Theta of the Past

To better resolve the directional relationship between theta and spiking in the vHPC-mPFC pathway, phase-locking in the reverse direction was analyzed: vHPC cells to mPFC theta. Here a temporal directionality *was* revealed, with vHPC cells phase-locking preferentially to mPFC theta of the past (Figure 5.4), meaning that vHPC spike timing is predicted by mPFC theta phase.

vHPC cells that significantly phase-lock do so maximally at negative lags, indicating that vHPC spiking follows mPFC Theta (N = 51 cells, z = -5.03, p = $2.4x10^{-7}$). Moreover, examination of mean PPC value among vHPC cells phase-locked to mPFC theta also revealed temporal directionality, with vHPC cells phase-locking maximally to mPFC theta from 30-35ms in the past.

This finding suggests that vHPC-mPFC input likely does not entrain mPFC theta-patterned activity, but rather that mPFC theta influences vHPC activity through an indirect pathway. Consistent with this conclusion, vHPC-mPFC terminal inhibition did not affect phase-locking of mPFC cells to either vHPC or dHPC theta (Figure 5.3G).

5.5 vHPC Gamma Robustly and Coherently Modulates Local Output

The surprising result that mPFC theta oscillations drive vHPC spiking motivated us to look at other frequency ranges for a signature of directional modulation in the monosynaptic vHPC-mPFC pathway. We therefore examined gamma oscillations in the vHPC and their role in driving local and downstream spike activity.

Measuring phase-locking of vHPC units to local gamma, we did find robust phase-locking, with 21% of cells significantly phase-locking to local gamma. These cells phase-locked preferentially to local gamma at a zero lag, as measured by the lag at which the most cells were significantly phase-locked, the lag at which phase-locked cells had their maximal PPC value, and lag with the

greatest mean PPC value (Figure 5.5). Moreover, phase-locked vHPC cells showed a preferred overall gamma phase – when spikes pooled from all phase-locked vHPC cells were tested for circular non-uniformity, it was found that the population fired preferentially at the falling phase (180-360 degrees) of gamma cycles phase (N=25653 spikes, Rayleigh's $z = 23.5$ $p = 25.9 \times 10^{-11}$).

5.6 vHPC Gamma Directionally Modulates mPFC Spiking

A subset of mPFC cells significantly did phase-lock to vHPC gamma (8% at zero lag; Figure 5.6A), although a greater number of cells were phase-locked at lags in which vHPC gamma preceded mPFC spiking (Figure 5.6B). Moreover, mPFC cells phase-locking to vHPC gamma did so maximally at lags in which vHPC led. Moreover, a higher number of cells maximally phase-locked at lags less than zero, indicating the cells follow vHPC-gamma phase (N = 43 cells, Sign rank, $z = -2.2$, $p = 0.014$). These findings are consistent with the hypothesis that gamma-frequency inputs from the vHPC influence mPFC spike timing (Figure 5.6C-E).

Optogenetic inhibition of vHPC-mPFC terminals reduced the overall strength of gamma phase-locking (Figure 5.7A), indicating that the observed synchrony is likely mediated by direct vHPC-mPFC input. Terminal inhibition decreases phase-locking of mPFC cells to vHPC-gamma. Cells from Arch animals decreased in PPC value between Light Off and Light On runs, while cells

from EYFP animals showed no change (N = 140 cells, Signed rank z = -3.9, p = $8.7x10^{-5}$; N = 222 cells, z = -1.83, p = 0.07, respectively).

This directional vHPC-mPFC synchrony was not incidental to behavior; rather, it correlated with the effective encoding of task-related cues. PPC values were higher during sample than choice runs, suggesting that phase-locking is associated with the encoding phase of the trial (Figure 5.7B), in contrast to theta-synchrony, which has been shown to correlate with retrieval (Sigurdsson, Stark et al. 2010). Phase-locking is greater during encoding than retrieval. PPC value decreased between Sample and Choice runs (N = 458 cells z = -3.2, p = 0.0016).

Additionally, phase-locking was stronger during sample runs of correct trials than of incorrect trials (Figure 5.7C), suggesting that it may support more effective encoding of location cues. Phase-locking during encoding is greater in correct than in incorrect trials (N = 270 cells, z = -4.2, p = $3.5x10^{-5}$).

5.7 Discussion

Our data demonstrate that entrainment of mPFC spikes to vHPC gamma oscillations is a physiological signature of task-critical long-range signal propagation. We find that inhibition of the direct hippocampal input disrupts gamma-frequency synchrony between the vHPC and the mPFC, without affecting theta-frequency synchrony. These data suggest that the direct hippocampal-to-prefrontal pathway carries information about goal location to the mPFC, and that this information transfer involves coordination of activity in the gamma-frequency

range. vHPC gamma oscillations entrain local output in a phase-coherent manner, which influences mPFC spiking at putatively monosynaptic delays. This phenomenon is subtle – at the lag with greatest phase-locking, fewer than 10% of mPFC cells were significantly phase-locked to vHPC gamma. Nevertheless, the observed correlation between vHPC-mPFC gamma synchrony and effective encoding suggests that gamma synchrony could be a behaviorally-relevant marker of effective long-range functional connectivity (Yamamoto, Suh et al. 2014).

The finding that mPFC theta activity temporally led vHPC theta, and that theta synchrony between the two structures did not appear to depend upon vHPC-mPFC afferents, ran counter to our initial hypotheses. Prior work had shown that dHPC theta leads mPFC theta (Siapas, Lubenov et al. 2005, Sigurdsson, Stark et al. 2010), that theta waves travel from dHPC to vHPC (Lubenov and Siapas 2009, Patel, Fujisawa et al. 2012), and that silencing of vHPC activity affects dHPC-mPFC theta synchrony (O'Neill, Gordon et al. 2013), supporting the idea that the vHPC theta-patterned activity might directly entrain mPFC theta. Nonetheless, inhibition of the direct hippocampal input did not reduce vHPC-mPFC theta synchrony. The inhibition described here was incomplete (on the order of 40-50%). It is possible, therefore, that a more complete disruption of the direct input would have had a detectable effect on theta synchrony. However, the observable effects on both gamma frequency and behavioral performance suggest that, were theta synchrony to depend on this

input, the methods described here should have detected it. Moreover, the observation that mPFC leads vHPC in the theta range further supports the notion that the unidirectional vHPC-to-mPFC pathway does not play a role in this synchrony.

As to what circuit mediates hippocampal-prefrontal synchrony, two hypotheses are of particular interest. First, one or more upstream structures could entrain both mPFC and vHPC to a theta rhythm at separate latencies, such that theta-patterned activity reaches mPFC before vHPC. Alternatively, the mPFC theta-patterned output could entrain the vHPC theta signal by way of some intermediary structure. The first hypothesis is perhaps the better-supported of the two, particularly if one considers the dHPC as the putative upstream structure. Traveling waves of theta activity along the dorso-ventral axis of hippocampal Ca1 result in vHPC theta that lags dHPC theta by ~90° (50-60ms; (Patel, Fujisawa et al. 2012)), while in our current data set mPFC theta lags dHPC theta by 20-25ms, and vHPC lags mPFC by 30-35ms. Therefore, dHPC theta could be relayed to mPFC via an intermediary (for example, the midline thalamic nuclei) and to vHPC via dorso-ventral propagation, reaching mPFC first and offsetting mPFC and vHPC theta from one another. The alternative hypothesis, while plausible – mPFC could generate theta that propagates to vHPC via intermediaries (entorhinal, thalamic, striatal, amygdalar) – has scant data to recommend it.

5.8 Methods

Recording and Spike Sorting

Recordings were amplified, band-pass flitered (1-1000Hz LFPs, 600-6000Hz spikes), and digitized using the Neuralynx Digitcal Lynx system. LFPs were collected at a rate of 2kHz, while spikes were detected by online thresholding and collected at 32kHz. Units were initially clustered using Klustakwik (Ken Harris), sorted according to the first two principal components, voltage peak, and energy from each channel. Clusters were then accepted, merged, or eliminated based on visual inspection of feature segregation, waveform distinctiveness and uniformity, stability across recording session, and ISI distribution.

Phase-locking Analysis

Phase-locking of spikes to oscillatory phase of LFPs was performed using pairwise phase consistency (Vinck, Battaglia et al. 2012), which, unlike other commonly used measures of phase-locking, is unbiased by spike number (Vinck, van Wingerden et al. 2010). Nevertheless, to ensure a representative estimate of spike phase, we set a threshold of 100 spikes for all analysis; in comparisons of phase-locking across conditions (Figures 6G and 7F-H), only cells which fired 100 spikes in each condition were included. LFP signal was digitally band-pass filtered (4-12Hz for theta, 30-70Hz for gamma) using a zero-phase-delay filter

(filter0 provided by K. Harris and G. Buzsaki, order = sample frequency). The phase component calculated by a Hilbert transform, and a corresponding phase was assigned to each spike.

To compute PPC value, first, mean circular distance is evaluated as:

$$\hat{D} \equiv \frac{2}{N(N-1)} \sum_{j=1}^{N-1} \sum_{k=(j+1)}^{N} d\left(\theta_j, \theta_k\right)$$

To ensure a value that had adequate dynamic range to serve as a functional measure of relative phase-locking, mean phase difference was normalized to obtain the PPC value:

$$\hat{D}^{\star} = \frac{\pi - 2\hat{D}}{\pi}$$

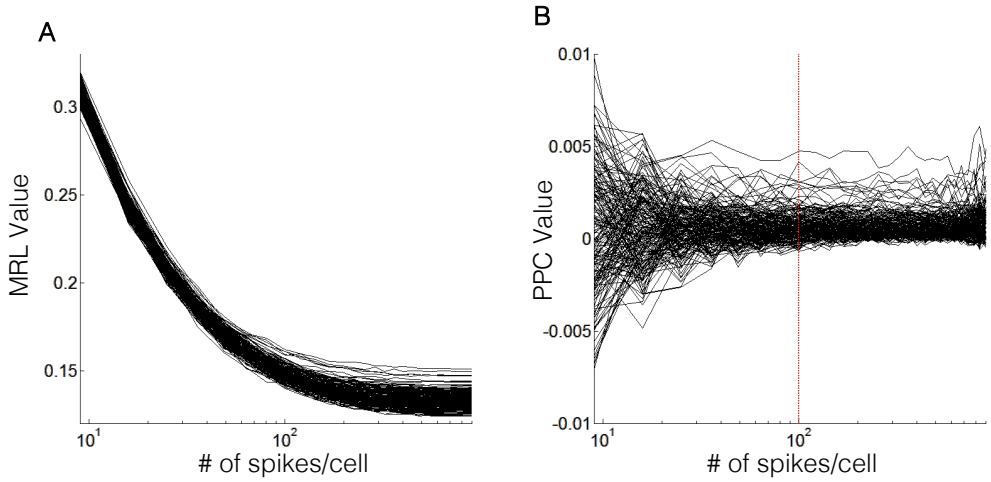

Figure 5.1 Comparison of Sample-Size Effects on MRL Value and PPC Value

A. All recorded units with >1000 spikes (N = 621) subsampled at increments between 10 and 1000 spikes. Mean resultant length (MRL), the sum of all spike phases around a unit circle, is strongly sample-biased, with higher values resulting from analysis of smaller spike subsets.

B. Same cells analyzed at sample subsamplings as (A), but for pairwise phase consistency values. Analysis at each subsampling size for each cell was performed 100 times, with the mean value plotted here. Unlike with MRL, PPC shows no sample bias, although subsamplings with fewer spikes yield more variable PPC values. We therefore set a cutoff for all

analyses, accepting only cells with 100 spikes for each condition in each analysis.

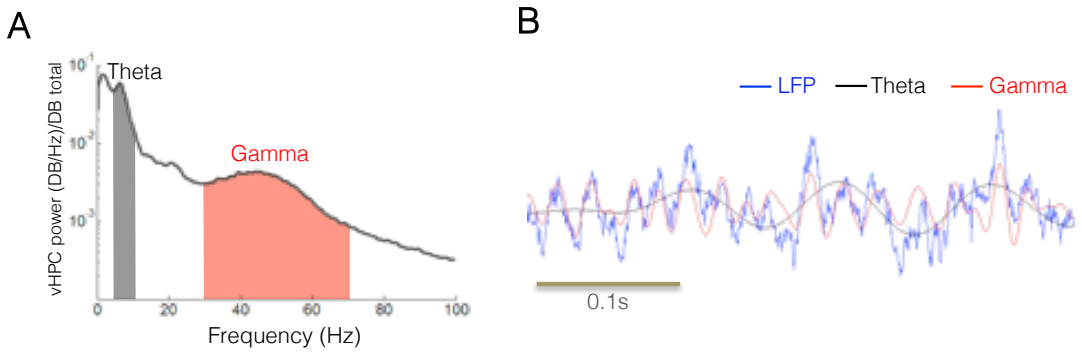

Figure 5.2 Theta and Gamma Activity Bands Are Clearly Visible in the LFP of vHPC During SWM

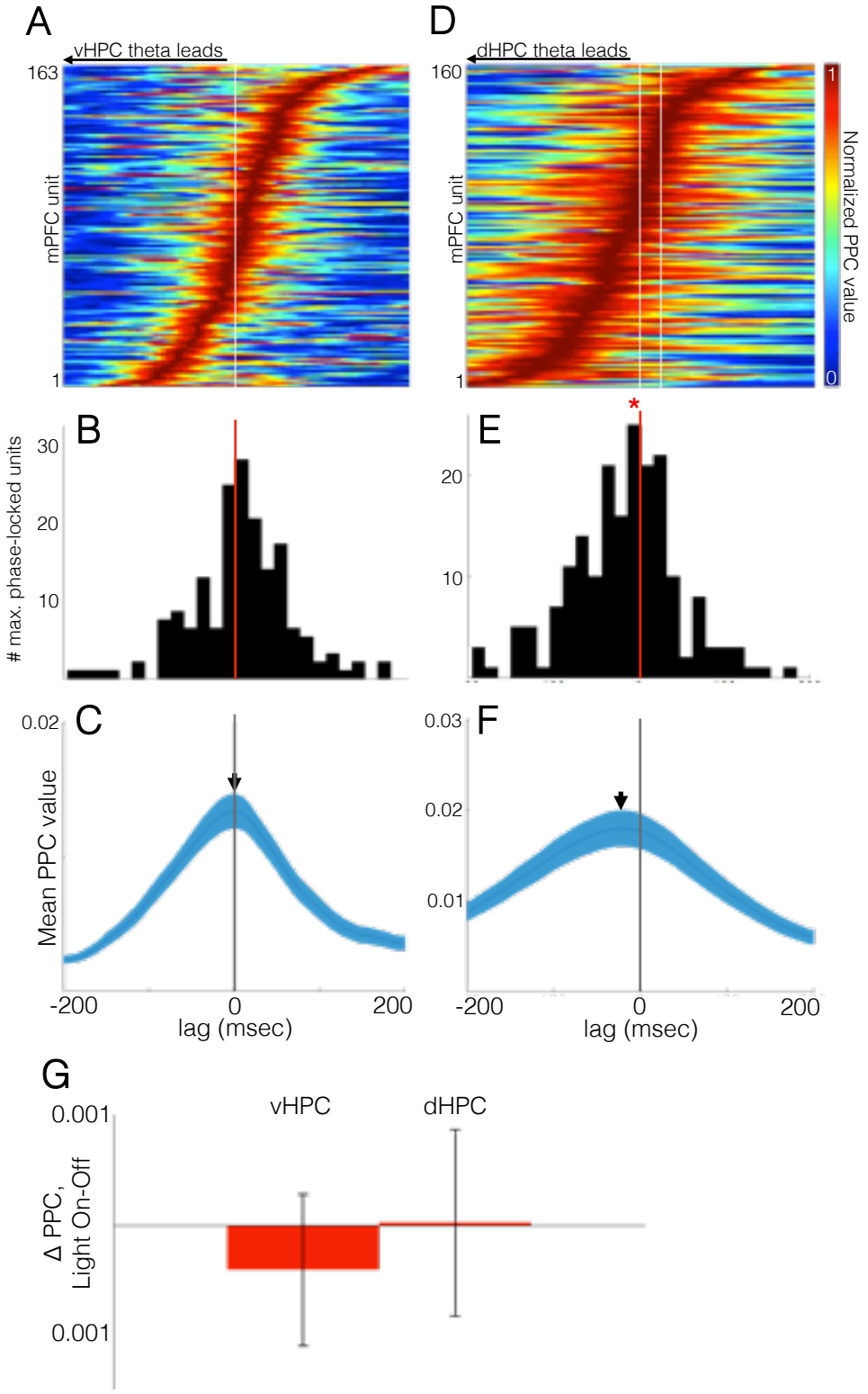

Figure 5.3 mPFC Spiking is Modulated by Theta Activity in dHPC but not vHPC

(A) Pseudocolor plot of relative strength of mPFC phaselocking to vHPC Theta at lags from -200ms to 200ms.

(B) mPFC cells that significantly phaselock are equally strongly phaselocked to vHPC Theta of the past and future, indicating a lack of temporal directionality (N = 189 cells, z = 2.05, p = 0.98)

(C) Mean PPC value among significantly phaselocked cells is maximal at a lag of zero, indicating a lack of temporal directionality.

(D) Pseudocolor plot of relative strength of mPFC phaselocking to dHPC Theta at temporal offsets (lags) from -200ms to 200ms. Warmer colors indicate higher PPC values, negative values along the x-axis indicate lags in which the dHPC Theta signal is aligned to mPFC spikes of the future.

(E) mPFC cells that significantly phaselock to dHPC Theta (Bonferonni-corrected significance within the -200 to 200ms lag window), tend to phaselock maximally at negative lags (N=160 cells, Sign rank z = -4.4, p = $6x10^{-6}$) at which mPFC spiking corresponds with the dHPC signal of the past.

(F) The mean PPC value among significantly phaselocked cells is also greatest at negative lags.

(G) Phaselocking of mPFC cells to dHPC Theta and vHPC Theta is not affected by vHPC-mPFC terminal inhibition (N=140 cells, Sign rank z = -1.3, p = 0.2; z = -1.4, p = 0.12).

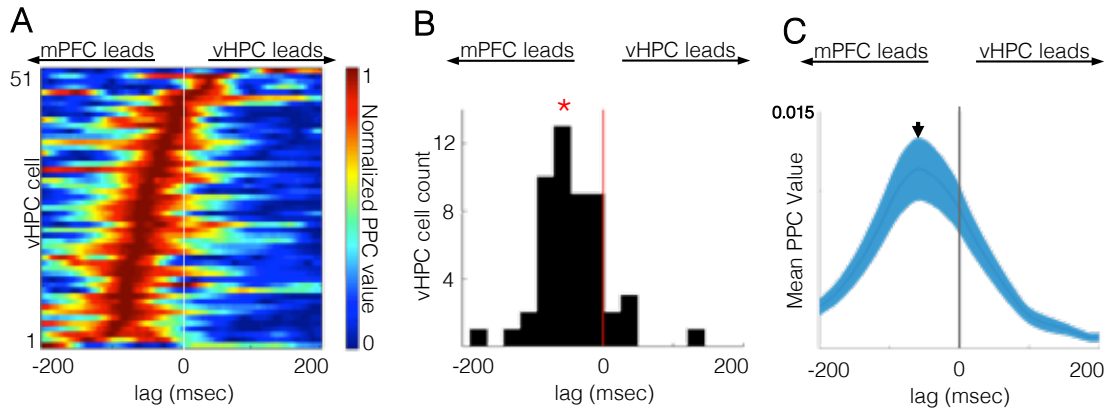

Figure 5.4 vHPC Spikes Are Modulated by mPFC Theta Activity

(A) Pseudocolor plot of relative strength of vHPC phaselocking to mPFC Theta at lags from -200ms to 200ms.

(B) vHPC cells that significantly phaselock do so maximally at negative lags, indicating that vHPC spiking follows mPFC Theta (N = 51 cells, z = -5.03, $p = 2.4 \times 10^{-7}$).

(C) Mean PPC value among significantly phaselocked cells is maximal negative lags, indicating that vHPC spiking follows mPFC.

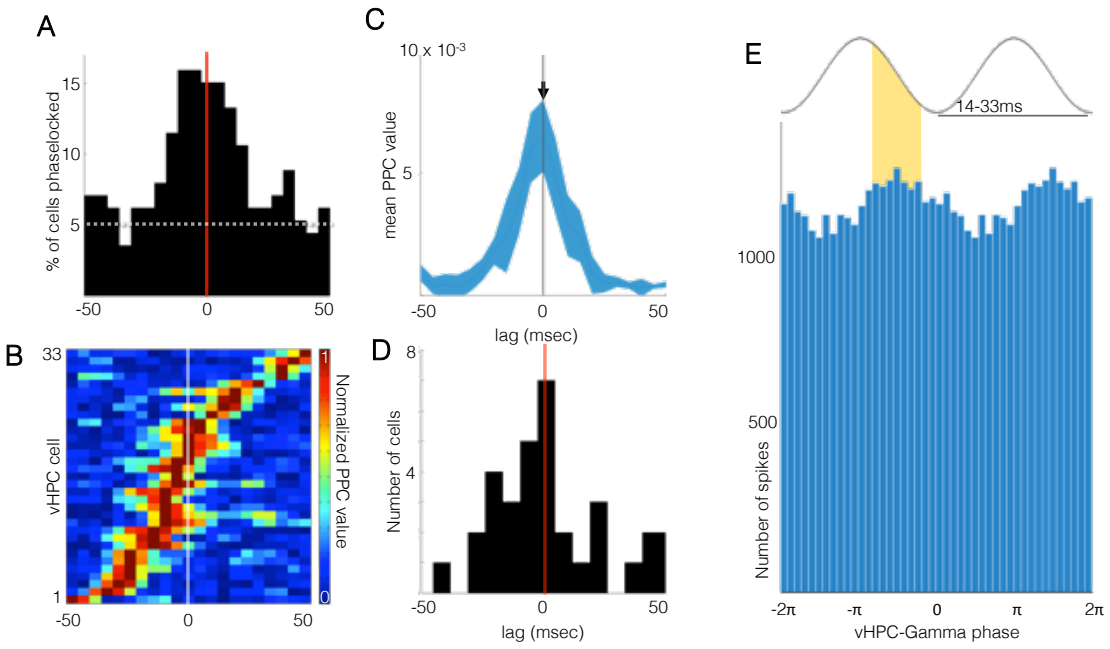

Figure 5.5 vHPC Gamma Modulates vHPC Output.

(A) vHPC cells phase-lock maximally to the vHPC-gamma rhythm at a lag of zero (p-value from Rayleigh's test < 0.05, dashed line indicates chance rate).

(B) Pseudocolor plot of normalized PPC values, sorted by lag of maximal phaselocking, for significantly phaselocked vHPC cells. Cells with Bonferroni-corrected significance within the -40 to 40ms lag window (Rayleigh test, $p < 0.0029$) were included.

(C) Mean normalized PPC value for the population shown in (B).

(D) Histogram of cells with maximum PPC value at each lag. Most cells maximally phase-locked at a lag of zero, with no significant difference from zero across the population ($t = 0.19$, $p = 0.85$).

(E) vHPC spikes show preferred gamma phase. Pooled spikes from significantly phase-locked vHPC cells were modulated by vHPC gamma phase (N=25653 spikes, Rayleigh's $z = 23.5$ $p = 25.9 \times 10^{-11}$, PPC=0.002), with peak spiking in the descending phase of the gamma cycle. The cirve is an idealized LFP whose gamma phase corresponds with the gamma (30-70Hz) phases of the spikes in the histogram below. The peak of this waveform corresponds with positive extracellular voltage, while the trough corresponds with negative voltage. The yellow bar marks the falling face of the wave, where vHPC spiking is highest. Note that spikes and LFPs were both recorded from stereotrodes in the stratum pyramidal and that this gamma phase would likely differ from that recorded in SLM, as in Figure 7.

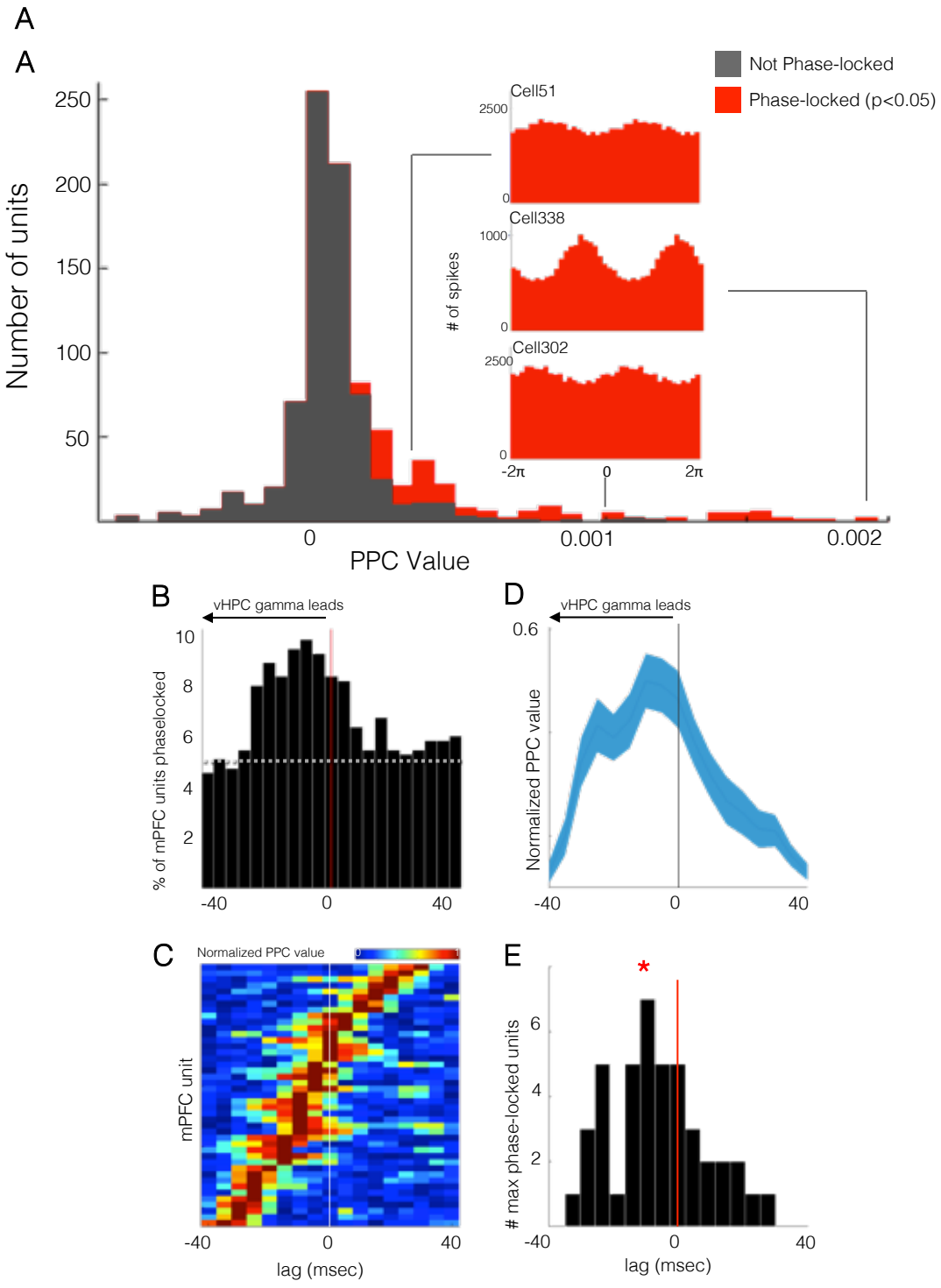

Figure 5.6 mPFC Spiking is Modulated by the vHPC Gamma Rhythm.

(A) Distribution of PPC values for all units from spikes recorded at all times. Non-phase-locked units (Rayleigh's $p > 0.05$) in grey, and phase-locked units (Rayleigh's $p < 0.05$) in red. Insets show vHPC gamma phase histograms from example phase-locked mPFC units (Cell51: Rayleigh's $z = -3.24$, $p < 0.001$, PPC value = 0.0003; Cell338: $z < -6$, $p < 0.0001$, PPC value = 0.002; Cell324: $z = -2.8$, $p = 0.002$, PPC value = 0.001).

(B) Percentage of mPFC units significantly phase-locked (p-value from Rayleigh's test < 0.05, dashed line indicates chance rate) to vHPC gamma across a range of lags.

(C) Pseudocolor plot of normalized PPC values, sorted by lag of maximal phase-locking, for mPFC units with Bonferroni-corrected significance within the -40 to 40ms lag window (Rayleigh test, $p < 0.0029$).

(D) Mean normalized PPC value for the population shown in C.

(E) Distribution of lags at peak phase-locking strength. Distribution was significantly shifted towards a vHPC lead (N = 43 units, Sign rank, $z = -2.2$, $p = 0.014$).

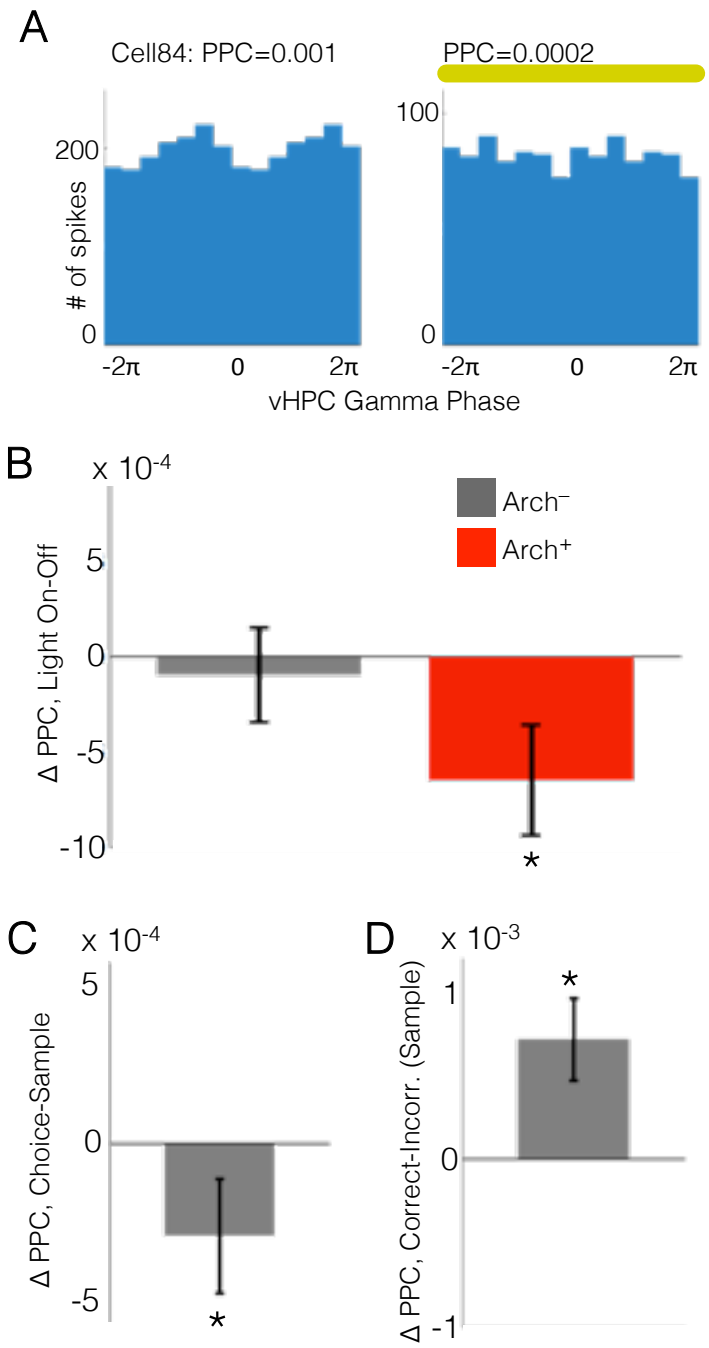

Figure 5.7 mPFC-vHPC Gamma Phase-locking is Mediated by Monosynaptic Input and by Behavior

(A) vHPC gamma phase histogram of spikes from an example mPFC unit from an $Arch^+$ animal during all Light Off runs (Rayleigh's p = 0.03, PPC = 0.001) and Light On runs (Rayleigh's p = 0.3, PPC = 0.0002). This cell shows a drop in PPC value of 0.0008, similar to the population mean shown in (**B**).

(B) Terminal inhibition decreases phase-locking of mPFC units to vHPC-gamma. Units from $Arch^+$ animals decreased in PPC value between Light Off and Light On runs, while units from $Arch^-$ animals showed no change. Mean and SEM shown for each (N = 140 units, Signed rank z = -3.9, p = $8.7x10^{-5}$; N = 222 units, z = -1.83, p = 0.07, respectively).

(C) Phase-locking is greater during encoding than retrieval. PPC value decreased between Sample and Choice runs. Mean and SEM shown (N = 458 units z = -3.2, p = 0.0016).

(D) Phase-locking during encoding is greater in correct than in incorrect trials. Mean and SEM shown (N = 270 units, z = -4.2, p = $3.5x10^{-5}$).

Chapter 6: Discussion of Findings

6.1 Summary of principal findings

Here we have built upon previous work showing a critical dependence of spatial working memory upon the joint activity of the vHPC and mPFC by demonstrating that direct input from vHPC to mPFC during the encoding of spatial cues, but not during maintenance or retrieval, is critical for successful SWM. We have also shown that this effect is input selective, as inhibition of input from NRe, another major source of glutamatergic drive to the mPFC, does not impair SWM performance during encoding. This effect was repeated across two cognitively similar yet structurally distinct behavioral paradigms with parallel results, bolstering the principal conclusion that vHPC-mPFC is selectively critical for encoding of SWM-related spatial cues.

This behavioral finding was further supported by concurring results from analysis of multiple single units within mPFC. These units exhibited location-selective firing properties, in that many cells fired preferentially near the maze goals, and of these cells many (several times higher numbers than chance) selectively coded for one or more spatial feature. As this coding scheme proved to be inhomogeneous and distributed, analysis of location selectivity was assessed using a maximum margin linear classifier to decode goal location from population rate vectors. This analysis revealed near perfect decoding of sample goal across the pseudosimultaneously recorded population, with accuracy peaking upon arrival at the sample goal. When the classifier was trained on trials with no illumination and tested on trials with illumination, there was a significant

decrease in model accuracy for cells from Arch-expressing animals, not for cells from opsin-negative controls.

The dependence of task-related cue encoding on vHPC input appeared to apply selectively to spatial information. Task phase was decoded from spike vectors at time bins concurrent with the opening of the doors at the beginning of sample and choice runs, a moment at which the decoding of task phase necessarily depended upon a memory trace from the preceding run. When task phase was decoded from choice runs following an illuminated sample run, there was no loss of model accuracy, indicating that vHPC input is not required for nonspecific (in this case episodic) cues and that the pathway is instead selective for spatial information.

Using the same classifier, we were able to decode the presence of light from cells in both control and Arch mice, although model accuracy for control mice only exceeded chance in several time bins, while for Arch cells it remained well above chance (and above values for control cells) throughout the approach to the goal. This was the case despite a lack of overall change in firing rate for cells in general, or for putative pyramidal cells or interneurons. Thus, while there was no nonspecific effect of terminal inhibition on firing rate, across the population there was a change in the pattern of firing rates that could be decoded.

Using cell weights extracted from the classifier after training, we identified the preferred goal for each cell – the goal at which firing was most different from

firing in the other 3 goals upon approach to the goal. Here we found that cells with high overall goal selectivity had higher firing rates (normalized to their overall rates) at the goals than cells with low goal selectivity. We found that goal preference across all cells, and particularly for highly selective cells, was observed as an elevation in firing rate upon reaching the goal, and that inhibition of vHPC input abolished this firing rate increase. Furthermore, this elevation in firing rate was present also during approach to the choice goal, but during this task phase it unaffected by vHPC input. Thus, goal selective firing of mPFC units was vHPC dependent only during cue encoding, and not during retrieval.

Having determined that vHPC-mediated excitation is required for mPFC spatial encoding, we then sought to identify a signature for long-range functional connectivity in the form of oscillatory synchrony. vHPC and mPFC exhibited pronounced theta and gamma oscillations, and synchrony in both frequency ranges was examined. While nearly half of mPFC cells were significantly phase-locked to vHPC theta oscillations, lag analysis revealed that they were not more strongly phase-locked to vHPC theta phases of the past than of the future, this despite a replication of previous studies showing preferential phase-locking to dHPC theta phases of the past. Moreover, when an inverse analysis was performed, examining phase-locking of vHPC units to mPFC theta, again strong phase-locking was found, but here vHPC units were preferentially phase-locked to mPFC theta of the past, a paradoxical finding in light of the unidirectionality of the vHPC-mPFC anatomical projection. In line with this indication that mPFC

leads vHPC in the theta range and not vice versa, vHPC-mPFC terminal inhibition had no effect on the strength of vHPC-mPFC phase-locking.

Units of the mPFC also phase-locked to vHPC activity in the gamma range, albeit not as strongly; whereas ~40% of mPFC units were phase-locked to vHPC theta, between 8 and 10% of mPFC units were phase-locked to vHPC gamma. Nevertheless, this phase-locking exhibited directionality consistent with entrainment of mPFC units by vHPC gamma-patterned output via the direct anatomical vHPC-mPFC projection. This was further supported by the finding that vHPC units were themselves robustly modulated by local vHPC gamma rhythms. This modulation was coherent across vHPC units, as phase-locked units exhibited preferred gamma phase. In further support of the idea that vHPC-mPFC gamma synchrony is driven by direct vHPC-mPFC input, phase-locking strength decreased with terminal inhibition. This phase-locking was seen to correlate with effective encoding of spatial cues, as phase-locking was significantly higher during sample runs than choice runs, and higher during sample runs of correct trials than of incorrect trials.

6.2 Role of vHPC-mPFC input in SWM – specificity vs generality

The findings presented here represent a targeted sampling of the behavioral space in which the vHPC-mPFC pathway is likely to operate. The interaction of these structures is thought to play critical roles in anxiety (Adhikari, Topiwala et al. 2010, Adhikari, Topiwala et al. 2011), the regulation of fear

memories (Sotres-Bayon, Sierra-Mercado et al. 2012), and the development of object-context associations (Komorowski, Garcia et al. 2013). The finding of the necessity vHPC-mPFC input for SWM encoding is therefore merely a single piece in a larger puzzle which further experiments involving targeted circuit manipulations and further behavioral controls may elucidate and, hopefully, situate within a more coherent and comprehensive model for the purpose and role of this pathway.

While the present findings implicate the vHPC-mPFC pathway in the encoding of spatial cues with no indication of a requirement for maintaining or retrieving those cues, the lack of evidence herein for the role of this pathway in maintenance and/or retrieval does not conclude an exhaustive search. In the first experiment (involving the 2-goal T-maze), intratrial delay was adjusted for each animal according to overall performance in order to reduce inter-animal variance and to prevent ceiling and overtraining effects. Thus, the period of delay between encoding and retrieval was not experimentally varied. In the second experiment 2 delays were used, 10 and 20 seconds, and performance was not impaired by vHPC-mPFC terminal inhibition during retrieval at either delay. These delays were chosen in consideration of previous work implicating the mPFC itself in SWM performance in tasks with delays of <20 seconds (Rogers, Wright et al. 1992, Shaw and Aggleton 1993, Sloan, Good et al. 2006, Izaki, Takita et al. 2008). However, it is possible that the vHPC-mPFC input may become essential for maintenance and/or retrieval at longer delays. While it would be difficult to test

this hypothesis in the 4-goal task, in which performance was considerably lower than in the 2-goal task and in which longer delays may introduce behavioral floor effects, longer delays could feasibly be introduced in the 2-goal task.

These results demonstrate a requirement for vHPC-mPFC input in spatial working memory, and while analysis of mPFC unit representation of non-spatial task features did not reveal a requirement for vHPC input for encoding of episodic cues, further work would have to be done before concluding that the pathway is truly selective for spatial encoding. Working memory-dependent tasks employing olfactory, auditory, or touch-screen cues during vHPC-mPFC terminal inhibition would shed additional light of the spatial specificity or multimodal generality of working memory-related information transmitted across the vHPC-mPFC synapse. Such findings could serve to extend the implications of vHPC-mPFC connectivity beyond the rodent model by making use of behavioral paradigms better suited for translation into primate and clinical models.

While the criticality of vHPC-mPFC input for SWM encoding has been demonstrated, the vHPC may not be the exclusive source of SWM-related spatial cues in the mPFC. The nucleus accumbens, entorhinal cortex, and thalamic midline nuclei also may encode spatial information important for the mPFC encoding of SWM-related cues. Therefore, before placing special emphasis on the vHPC input for SWM, further experiments must be performed to silence input from these other structures, to determine the relative importance of this source of spatial information to the mPFC.

6.3 vHPC-mPFC Connectivity and Working Memory: Implications for Schizophrenia

The finding of criticality of the vHPC-mPFC pathway for encoding of cues related to SWM leads to a specific translational question. This question can further be parsed into more precise hypotheses that are experimentally tractable. The first is that the encoding phase of working memory is specifically disrupted in schizophrenia. If it is the case that such disruptions are exclusively a function of encoding, we expect working memory deficits in leading candidate models for schizophrenia to be delay-independent, as the relevant processing impairment would occur prior to the maintenance/retrieval phase. Second, location encoding should be disrupted in mPFC cells in rodent models of schizophrenia. Third, hippocampal-prefrontal gamma-range synchrony should be disrupted in schizophrenia models. These hypotheses can be readily tested by applying *in vivo* recording techniques to further genetic models of schizophrenia predisposition with finer-grained resolution. For example, the 22 genes affected by the 22q11.2 microdeletion are being parsed and individually tested for their respective contributions to the overall long-range connectivity deficit seen in the full deletion. By extending the application of both genetic tools and *in vivo* recording techniques, the relevance of the circuit perturbations used in the work presented here for the pathophysiology of schizophrenia can be assessed. Moreover, application of optogenetics to interrogated circuits within these genetic models (such as, for example, optogenetically driving long-range inputs and

observing the robustness of response in mutant animals) can yield further insights into the potential relevance of this circuit to the pathophysiology of schizophrenia.

References

Abbott, L. and P. Dayan (1999). "The effect of correlated variability on the accuracy of a population code." Neural Comput. **11**: 91–101.

Acker, L. and e. al. (2012). In vivo measurements of light propagation and brain heating: Implications for optogenetics. Society for Neuroscience.

Adhikari, A., M. Topiwala and J. Gordon (2010). "Synchronized activity between the ventral hippocampus and the medial prefrontal cortex during anxiety." Neuron **65**(2): 257-269.

Adhikari, A., M. Topiwala and J. Gordon (2011). "Single units in the medial prefrontal cortex with anxiety-related firing patterns are preferentially influenced by ventral hippocampal activity." Neuron **71**(5): 898-910.

Andersen, P. and E. I. Moser (1995). "Brain temperature and hippocampal function." Hippocampus **5**(6): 491-498.

Andrade, J. (2001). Working Memory in Context Sussex, Psychology.

Anlauf, J. and M. Biehl (1989). "The AdaTron: An Adaptive Perceptron Algorithm." Europhys. Lett. EPL **10**: 687–692.

Argyelan, M., T. Ikuta, P. DeRosse, R. Braga, K. Burdick, M. John, P. Kingsley, A. Malhotra and P. Szeszko (2014). "Resting-state FMRI connectivity impairment in schizophrenia and bipolar disorder." Schizophr Bull. **40(1)**: 100-110.

Aronov, D. and M. Fee (2011). "Analyzing the dynamics of brain circuits with temperature: design and implementation of a miniature thermoelectric device." Journal of Neuroscience Methods **197**(1): 32-47.

Arriaga, G., E. Zhou and E. Jarvis (2012). "Of Mice, Birds, and Men: The Mouse Ultrasonic Song System Has Some Features Similar to

Humans and Song-Learning Birds." PLoS One **DOI: 10.1371/journal.pone.0046610**.

Atkinson, R. and R. Shiffrin (1971). "The control of short-term memory." Scientific American: 82-90.

Baddeley, A. (2003). "Working Memory: Looking back and looking forward." Nature Reviews Neuroscience **4**(October).

Baddeley, A. (2003). "Working memory: looking back and looking forward." Nature Reviews Neuroscience **4**: 829-839.

Baddeley, A. and G. Hitch (1974). Working Memory. Recent advances in learning and motivation. G. Bower. New York, Academic Press. **8:** 47–90.

Baeg, E., Y. Kim, K. Huh, I. Mook-Jung, H. Kim and M. Jung (2003). "Dynamics of Population Code for Working Memory in the Prefrontal Cortex. ." Neuron **40**(1): 177–188.

Baldeweg, T., S. Spence, S. Hirsch and J. Gruzelier (1998). "γ-band electroencephalographic oscillations in a patient with somatic hallucinations. ." The Lancet **352**(9128).

Barak, O. and M. Rigotti (2011). "A Simple Derivation of a Bound on the Perceptron Margin Using Singular Value Decomposition." Neural Comput. **2011**(1935–1943).

Barbey, A., M. Koenigs and J. Grafman (2013). "Dorsolateral prefrontal contributions to human working memory." Cortex **49**(5): 1195-1205.

Bassett, D., B. Nelson, B. Mueller, J. Camchong and K. Lim (2012). "Altered resting state complexity in schizophrenia." Neuroimage. **59(3)**: 2196-2207.

Belfort, G., Y. Lin, P. Monahan and E. Boyden (2010). "High-performance genetically targetable optical neural silencing by lightdriven proton pumps." Nature **463**: 98–102.

Belforte, J., V. Zsiros, E. Sklar, Z. Jiang, G. Yu, Y. Li, E. Quinlan and K. Nakazawa (2010). "Postnatal NMDA receptor ablation in corticolimbic interneurons confers schizophrenia-like phenotypes." Nat Neurosci. **13(1)**: 76-83.

Boyden, E., F. Zhang, E. Bamberg, G. Nagel and K. Deisseroth (2005). "Millisecond-timescale, genetically targeted optical control of neural activity." Nat Neuroscience **8**(9): 1263-1268.

Brenner, C., O. Sporns, P. Lysaker and B. O'Donnell (2003). "EEG synchronization to modulated auditory tones in schizophrenia, schizoaffective disorder, and schizotypal personality disorder." Am. J. Psychiatry **160**: 2238–2240.

Burgess, N. and J. O'Keefe (2003). "Neural representations in human spatial memory." TRENDS in Cognitive Sciences **145**(1): 1-3.

Burton, B., V. Hok, E. Save and B. Poucet (2009). "Lesion of the ventral and intermediate hippocampus abolishes anticipatory activity in the medial prefrontal cortex of the rat." Behav Brain Res **199**: 222–234.

Buzsaki, G. (2006). Rhythms of the Brain. Oxford, University Press.

Buzsaki, G. and X. Wang (2012). "Mechanisms of Gamma Oscillations." Annu. Rev. Neurosci. **35**: 203–225.

Caputi, A., S. Melzer, M. Michael and H. Monyer (2013). "The long and short of GABAergic neurons." Curr Opin Neurobiol **23**(2): 179-186.

Cardin, J., M. Carlén, K. Meletis, U. Knoblich, F. Zhang, K. Deisseroth, L. Tsai and M. CI (2009). "Driving fast-spiking cells induces gamma rhythm and controls sensory responses." Nature **459(7247)**: 663-667.

Chai, X., S. Whitfield-Gabrieli, A. Shinn, J. Gabrieli, C. Nieto, J. McCarthy, B. Cohen and D. Ongür (2011). "Abnormal medial prefrontal cortex resting-state connectivity in bipolar disorder and schizophrenia." Neuropsychopharmacology. **36(10)**: 2009-2017.

Chang, X., H. Shen, L. Wang, Z. Liu, W. Xin, D. Hu and D. Miao (2014). "Altered default mode and fronto-parietal network subsystems in patients with schizophrenia and their unaffected siblings." Brain Res. **1562**: 87-99.

Cho, R., R. Konecky and C. Carter (2006). "Impairments in frontal cortical gamma synchrony and cognitive control in schizophrenia. ." Proc. Natl Acad. Sci. **103**: 19878–19883.

Christie, I. and e. al. (2012). "fMRI response to blue light delivery in the native brain: Implications for combined optogenetic fMRI studies." Neuroimage **66C**: 634-641.

Conklin, H., C. Curtis, J. Katsanis and W. Iacono (2000). "Verbal working memory impairment in schizophrenia patients and their first-degree relatives: evidence from the digit span task." Am J Psychiatry **157**(2): 275-277.

Curley, A., D. Arion, D. Volk, J. Asafu-Adjei, A. Sampson, K. Fish and D. Lewis (2011). "Cortical deficits of glutamic acid decarboxylase 67 expression in schizophrenia: clinical, protein, and cell type-specific features." Am J Psychiatry. **168(9)**: 921-929.

Curtis, C. and M. D'Esposito (2004). "The effects of prefrontal lesions on working memory performance and theory." Cogn Affect Behav Neurosci **4**(4): 528-539.

Davis, K., D. Stewart, J. Friedman, M. Buchsbaum, P. Harvey, P. Hof, J. Buxbaum and V. Haroutunian (2003). "White matter changes in schizophrenia: evidence for myelin-related dysfunction." Arch Gen Psychiatry. **60(5)**: 443-456.

de Zubicaray, G., K. McMahon, S. Wilson and S. Muthiah (2001). "Brain Activity During the Encoding, Retention, and Retrieval of Stimulus Representations." Learn. Mem **8**: 243-251.

Del Pino, I., C. García-Frigola, N. Dehorter, J. Brotons-Mas, E. Alvarez-Salvado, M. Martínez de Lagrán, G. Ciceri, M. Gabaldón, D. Moratal, M. Dierssen, S. Canals, O. Marín and B. Rico (2013). "Erbb4 deletion from fast-spiking interneurons causes schizophrenia-like phenotypes." Neuron **79(6)**: 1152-1168.

Dickerson, D., A. Wolff and D. Bilkey (2010). "Abnormal long-range neural synchrony in a maternal immune activation animal model of schizophrenia." J Neurosci. **30(37)**: 12424-12431.

Dietterich, T. and B. Ghulum (1991). "Error-correcting output codes: A general method for improving multiclass inductive learning programs." AAAI: 572-577.

Donato, F., S. Rompani and P. Caroni (2010). "Parvalbumin-expressing basket-cell network plasticity induced by experience regulates adult learning." Nature **504(7479)**: 272-276.

Dudchenko, P. (2004). "An overview of the tasks used to test working memory in rodents." Neurosci Biobehav Rev **28**(7): 699-709.

Euston, D., A. Gruber and B. McNaughton (2012). "The role of medial prefrontal cortex in memory and decision making." Neuron **76**(6): 1057-1070.

Fanselow, M. and H. Dong (2010). "Are The Dorsal and Ventral Hippocampus functionally distinct structures?" Neuron **65**(1): 7.

Fejgin, K., J. Nielsen, M. Birknow, J. Bastlund, V. Nielsen, J. Lauridsen, H. Stefansson, S. Steinberg, H. Sorensen, T. Mortensen, P. Larsen, I. Klewe, S. Rasmussen, K. Stefansson, T. Werge, P. Kallunki, K. Christensen and M. Didriksen (2013). "A Mouse Model that Recapitulates Cardinal Features of the 15q13.3 Microdeletion Syndrome Including Schizophrenia- and Epilepsy-Related Alterations." Biol Psychiatry. **S0006-3223(13)00767-1**.

Fénelon, K., J. Mukai, B. Xu, P. Hsu, L. Drew, M. Karayiorgou, G. Fischbach, A. Macdermott and J. Gogos (2011). "Deficiency of Dgcr8, a gene disrupted by the 22q11.2 microdeletion, results in altered short-term plasticity in the prefrontal cortex." Proc Natl Acad Sci **108(11)**: 4447-4452.

Friston, K. J. (1999). "Schizophrenia and the disconnection hypothesis." Acta Psychiatr. Scand. Suppl. **395**: 68–79.

Fujisawa, S., A. Amarasingham, M. Harrison and G. Buzsáki (2008). "Behavior-dependent short-term assembly dynamics in the medial prefrontal cortex." Nat Neurosci. **11**(7): 823-833.

Funahashi, S., C. Bruce and P. Goldman-Rakic (1989). " Mnemonic coding of visual space in the monkey's dorsolateral prefrontal cortex." J. Neurophysiol **61**: 331–349.

Fuster, J. (1973). "Unit activity in prefrontal cortex during delayed-response performance: Neuronal correlates of transient memory." J.Neurophysiol **36**: 61–78.

Fuster, J. and G. Alexander (1971). "Neuron activity related to short-term memory." Science **17**: 652–654.

Gandal, M., J. Edgar, K. Klook and S. Siegel (2012). "Gamma synchrony: Towards a translational biomarker for the treatment-resistant symptoms of schizophrenia." Neuropharmacology **62**(3): 1504-1518.

Gradinaru, V., F. Zhang, C. Ramakrishnan, J. Mattis, R. Prakash, I. Diester, I. Goshen, K. Thompson and K. Deisseroth (2010). "Molecular and Cellular Approaches for Diversifying and Extending Optogenetics." Cell **141**: 154-165.

Gray, C. and W. Singer (1989). "Stimulus-specific neuronal oscillations in orientation columns of cat visual cortex." PNAS **86**: 1698-1702.

Grützner, C., M. Wibral, L. Sun, D. Rivolta, W. Singer, K. Maurer and P. Uhlhaas (2013). "Deficits in high- (>60 Hz) gamma-band oscillations during visual processing in schizophrenia." Front Hum Neurosci. **7**: 88.

Guidotti, A., J. Auta, J. Davis, V. Di-Giorgi-Gerevini, Y. Dwivedi, D. Grayson, F. Impagnatiello, G. Pandey, C. Pesold, R. Sharma, D. Uzunov and E. Costa (2000). "Decrease in reelin and glutamic acid decarboxylase67 (GAD67) expression in schizophrenia and bipolar disorder: a postmortem brain study." Arch Gen Psychiatry. **57(11)**: 1061-1069.

Haenschel, C., R. Bittner, J. Waltz, F. Haertling, M. Wibral, W. Singer, D. Linden and E. Rodriguez (2009). "Cortical oscillatory activity is critical for working memory as revealed by deficits in early-onset schizophrenia." J Neurosci. **29(30)**: 9481-9489.

Hakak, Y., J. Walker, C. Li, W. Wong, K. Davis, J. Buxbaum, V. Haroutunian and A. Fienberg (2001). "Genome-wide expression analysis reveals dysregulation of myelination-related genes in chronic schizophrenia." Proc Natl Acad Sci **98(8)**: 4746-4751.

Han, X. (2012). "Optogenetics in the Nonhuman Primate." Progress in Brain Research **196**: 215-233.

Harvey, P., M. Green, R. Keefe and D. Velligan (2004). "Cognitive Functioning in Schizophrenia: A Consensus Statement on Its Role in the Definition and Evaluation of Effective Treatments for the Illness." Journal of Clinical Psychiatry **65**(3): 361-372.

Hashimoto, T., D. Volk, S. Eggan, K. Mirnics, J. Pierri, Z. Sun, A. Sampson and D. Lewis (2003). "Gene expression deficits in a subclass of GABA neurons in the prefrontal cortex of subjects with schizophrenia." J Neurosci. **23(15)**: 6315-6326.

Hok, V., E. Save, P. Lenck-Santini and B. Poucet (2005). "Coding for spatial goals in the prelimbic/infralimbic area of the rat frontal cortex." Proc Natl Acad Sci **102**(12): 4602-4607.

Hoover, W. and R. Vertes (2007). "Anatomical analysis of afferent projections to the medial prefrontal cortex in the rat." Brain Struct Funct **212**: 149–179.

Hoover, W. and R. Vertes (2007). "Anatomical analysis of afferent projections to the medial prefrontal cortex in the rat." Brain Struct Funct **212**(149–179).

Horst NK, L. M. (2012). "Working with memory: evidence for a role for the medial prefrontal cortex in performance monitoring during spatial delayed alternation." J Neurophysiol. **108(12)**: 3276-3288.

Hou, X., K. Ni, Yang JM and X. Li (2014). "Neuregulin 1/ErbB4 enhances synchronized oscillations of prefrontal cortex neurons via inhibitory synapses." Neuroscience **261**: 107-117.

Hyman, J., E. Zilli, A. Paley and M. Hasselmo (2010). "Working Memory Performance Correlates with Prefrontal-Hippocampal Theta Interactions but not with Prefrontal Neuron Firing Rates." Front Integr Neurosci. **4**(2).

Hymana, J., L. Maa, E. Balaguer-Ballesterb, D. Durstewitzb and J. Seamansa (2012). "Contextual encoding by ensembles of medial prefrontal cortex neurons." PNAS **109**(13): 5086–5091.

Izaki, Y., M. Takita and T. Akema (2008). "Specific role of the posterior dorsal hippocampus-prefrontal cortex in short-term working memory." Eur J Neurosci **27**(11): 3029-3034.

James, W. (1890). Principles of Psychology. New York, Holt.

Jay, T., A. Thierry, L. Wiklund and J. Glowinski (1992). "Excitatory amino acid pathway from the hippocampus to the prefrontal cortex. Contribution of AMPA receptors in hippocampo-prefrontal cortex transmission." Eur. J. Neurosci **4**: 1285–1295.

Jay, T. and M. Witter (1991). "Distribution of hippocampal CA1 and subicular afferents in the prefrontal cortex of the rat studied by means of anterograde transport of Phaseolus vulgaris leucoagglutinine." J. Comp. Neurol **313**: 574–586.

Jay, T. and M. Witter (1991). "Distribution of hippocampal CA1 and subicular afferents in the prefrontal cortex of the rat studied by means of anterograde transport of Phaseolus vulgaris leucoagglutinine." J. Comp. Neurol **313**(574–586).

Jeneson, A., K. Mauldin and L. Squire (2010). "Intact Working Memory for Relational Information after Medial Temporal Lobe Damage." J Neurosci **30**(41): 13624-13629.

Jensen, O., J. Gelfand, J. Kounios and J. Lisman (2002). "Oscillations in the alpha band (9-12 Hz) increase with memory load during retention in a short-term memory task." Cereb. Cortex **12**(8): 877-882.

Jensen, O. and C. Tesche (2002). "Frontal theta activity in humans increases with memory load in a working memory task." Eur J Neurosci **15**: 1395-1399.

Jo, Y., E. Park, I. Kim, S. Park, H. Kim, H. Kim and J. Choi (2007). "The Medial Prefrontal Cortex Is Involved in Spatial Memory Retrieval under Partial-Cue Conditions." The Journal of Neuroscience **27**(49): 13567-13578.

Johansson, J. (2010). "Spectroscopic method for the determination of the absorption coefficient in brain tissue." BIOMEDO **15**(5): 57005-57009.

Jones, M. and M. Wilson (2005). "Theta rhythms coordinate hippocampal-prefrontal interactions in a spatial working memory task. ." PLoS Biol. **2**: e402.

Jones, M. and M. Wilson (2005). "Theta Rhythms Coordinate Hippocampal–Prefrontal Interactions in a Spatial Memory Task." PLoS Biology **3**(12): 402.

Joseph, J. and P. Barone (1987). "Prefrontal unit activity during a delayed oculomotor task in the monkey." Exp. Brain Res. **67**: 460–468.

Jung, M., Y. Qin, B. McNaughton and C. Barnes (1998). "Firing characteristics of deep layer neurons in prefrontal cortex in rats performing spatial working memory tasks." Cereb Cortex **8**(5): 437-450.

Jung, M., S. Wiener and B. McNaughton (1994). "Comparison of spatial firing characteristics of units in dorsal and ventral hippocampus of the rat." J Neurosci **14**(12): 7347-7356.

Keinath, A., M. Wang, E. Wann, R. Yuan, J. Dudman and I. Muzzio (2014). "Precise spatial coding is preserved along the longitudinal hippocampal axis." Hippocampus **[Epub ahead of print]**.

Kim, J. A. and B. W. Connors (2012). "High temperatures alter physiological properties of pyramidal cells and inhibitory interneurons in hippocampus." Front Cell Neurosci **6**: 27.

Kjelstrup, K., T. Solstad, V. Brun, T. Hafting, S. Leutgeb, M. Witter, E. Moser and M. Moser (2008). "Finite scale of spatial representation in the hippocampus." Science **321**(5885): 140-143.

Klauer, K. and Z. Zhao (2004). "Double dissociations in visual and spatial short-term memory." Journal of Experimental Psychology: General **133**: 355–381.

Komorowski, R., C. Garcia, A. Wilson, A. Hattori, M. Howard and E. H (2013). "Ventral hippocampal neurons are shaped by experience to represent behaviorally relevant contexts." J Neurosci. **33**(18): 8079-8087.

Komorowski, R., C. Garcia, A. Wilson, S. Hattori, M. Howard and H. Eichenbaum (2013). "Ventral hippocampal neurons are shaped by experience to represent behaviorally relevant contexts." J Neurosci **26**(18): 4852-4859.

Krauth, W. and M. Mezard (1987). "Learning algorithms with optimal stability in neural networks." J. Phys. Math. Gen. **20**: L745–L752.

Krishnan, G., W. Hetrick, C. Brenner, A. Shekhar, A. Steffen and B. O'Donnell (2009). "Steady state and induced auditory gamma deficits in schizophrenia. ." Neuroimage **47**: 1711–1719

Kubicki, M., R. McCarley, C. Westin, Park HJ, S. Maier, R. Kikinis, F. Jolesz and M. Shenton (2007). "A review of diffusion tensor imaging studies in schizophrenia." J Psychiatr Res. **41(1-2)**: 15-30.

Kurihara, M., J. Dunlop, N. Bandon, Z. Hughes, A. Randall and J. Brown (2013). Altered hippocampal-medial prefrontal cortex connectivity In vitro and In vivo in a transgenic Disc1 mouse model of psychiatric disease. Soc Neurosci

Kwon, J., B. O'Donnell, G. Wallenstein, R. Greene, Y. Hirayasu, P. Nestor, M. Hasselmo, G. Potts, M. Shenton and R. McCarley (1999). "Gamma frequency-range abnormalities to auditory stimulation in schizophrenia." Arch Gen Psychiatry. **56(11)**: 1001-1005.

Lazarewicz, M., R. Ehrlichman, C. Maxwell, M. Gandal, L. Finkel and S. Siegel (2010). "Ketamine modulates theta and gamma oscillations." J Cogn Neurosci. **22(7)**: 1452-1464.

Lee, I. and R. Kesner (2003). "Time-Dependent Relationship between the Dorsal Hippocampus and the Prefrontal Cortex in Spatial Memory." The Journal of Neuroscience **23**(4): 1517.

Lewis, D., A. Curley, J. Glausier and D. Volk (2012). "Cortical parvalbumin interneurons and cognitive dysfunction in schizophrenia." Trends Neurosci. **35(1):**: 57-67.

Light, G., J. Hsu, M. Hsieh, K. Meyer-Gomes, J. Sprock, N. Swerdlow and D. Braff (2006). "Gamma band oscillations reveal neural network cortical coherence dysfunction in schizophrenia patients." Biol Psychiatry. **60(11)**: 1231-1240.

Lim, K., M. Hedehus, M. Moseley, A. de Crespigny, E. Sullivan and A. Pfefferbaum (1999). "Compromised white matter tract integrity in schizophrenia inferred from diffusion tensor imaging." Arch Gen Psychiatry. **56(4)**: 367-374.

Lin, J., S. Sann, K. Zhou, S. Nabavi, C. Proulx, R. Malinow, Y. Jin and R. Tsien (2013). "Optogenetic Inhibition of Synaptic Release with Chromophore-Assisted Light Inactivation (CALI)." Neuron **79**: 241-253.

Logie, R. (1995). Visuo-spatial working memory. UK, Lawrence Eribaum Associates.

Lubenov, E. and A. Siapas (2009). "Hippocampal theta oscillations are travelling waves." Nature **459**: 534-539.

Machens, C., R. Romo and C. Brody (2010). "Functional, But Not Anatomical, Separation of “What” and “When” in Prefrontal Cortex." J. Neuroscience **30**(1): 350-360.

Marder, E. (2011). "Variability, compensation, and modulation in neurons and circuits." PNAS **108**: 15542-15548.

Meyers, E., D. Freedman, G. Kreiman, E. Miller and T. Poggio (2008). "Dynamic population coding of category information in inferior temporal and prefrontal cortex." J. Neurophysiol **100**: 1407–1419.

Miller, E. (2013). "The “working” of working memory." Dialogues Clin Neurosci. **15**(4): 411–418.

Milner, P. (1974). "A model for visual shape recognition." Psychological Review **81**(6): 521-535.

Miyake, A. and P. Shah (1999). Models of Working Memory: Mechanisms of Active Maintenance and Executive Control. New York, Cambridge University Press.

Moser, E., I. Mathiesen and P. Andersen (1993). "Association between brain temperature and dentate field potentials in exploring and swimming rats." Science **259**(5099): 1324-1326.

Moser E, M. I., Andersen P (1993). "Association between brain temperature and dentate field potentials in exploring and swimming rats." Science **26**(259(5099)): 1324-1326.

Moser, E. I. and P. Andersen (1994). "Conserved spatial learning in cooled rats in spite of slowing of dentate field potentials." J Neurosci **14**(7): 4458-4466.

Niki, H. (1974). "Differential activity of prefrontal units during right and left delayed response trials." Brain Res. **70**: 346–349.

Niki, H. and M. Watanabe (1976). "Prefrontal unit activity and delayed response: relation to cue location versus direction of response." Brain Res. **105**(1): 79-88.

O'Keefe, J., N. Burgess, J. Donnett, K. Jeffery and E. Maguire (1998). "Place cells, navigational accuracy, and the human hippocampus." Philos Trans R Soc Lond B Biol Sci **353**(1373): 1333–1340.

O'Keefe, J. and J. Dostrovsky (1971). "The hippocampus as a spatial map. Preliminary evidence from unit activity in the freely-moving rat." Brain Res **1971**(34): 1.

O'Neill, P., J. Gordon and T. Sigurdsson (2013). "Theta oscillations in the medial prefrontal cortex are modulated by spatial working memory and synchronize with the hippocampus through its ventral subregion." J Neurosci **33**(35): 14211-14224.

Oh, S. (2014). "A mesoscale connectome of the mouse brain." Nature **508**: 207–214.

Pajevic, S., P. Basser and R. Fields (2013). "Role of myelin plasticity in oscillations and synchrony of neuronal activity." Neuroscience **S0306-4522(13)00947-0**.

Park, S. and P. Holzman (1992). "Schizophrenics show spatial working memory deficits." Arch Gen Psychiatry. **49**(12): 975-982.

Patel, J., S. Fujisawa, A. Berényi, S. Royer and G. Buzsáki (2012). "Traveling theta waves along the entire septotemporal axis of the hippocampus." Neuron **75**(3): 410-417.

Pennes, H. (1948). "Analysis of tissue and arterial blood temperatures in the resting human forearm." Journal of Applied Physiology **1**(2): 93-122.

Ponce, C., S. Lomber and R. Born (2008). "Using temperature to analyse temporal dynamics in the songbird motor pathway." Nature **11**(2): 216-223.

Poucet, B., C. Thinus-Blanc and R. Muller (1994). "Place cells in the ventral hippocampus of rats." Neuroreport **5**(16): 2045-2048.

Rajagovindan, R. and M. Ding (2008). "Decomposing Neural Synchrony: Toward an Explanation for Near-Zero Phase-Lag in Cortical Oscillatory Networks." PLOS One **3(11)**: e3649.

Rigotti, M., O. Barak, M. Warden, X. Wang, N. Daw, E. Miller and S. Fusi (2013). "The importance of mixed selectivity in complex cognitive tasks." Nature **497**: 585–590.

Rogers, D., P. Wright, J. Roberts, C. Reavill, A. Rothaul and J. Hunter (1992). "Photothrombic lesions of the frontal cortex impair the performance of the delayed non-matching to position task by rats." Behavioural Brain Research **49**(1): 231-235.

Rosenblatt, F. (1962). Principles of neurodynamics: perceptrons and the theory of brain mechanisms, Spartan.

Royer, S., A. Sirota, J. Patel and G. Buzsaki (2010). "Distinct Representations and Theta Dynamics in Dorsal and Ventral Hippocampus." The Journal of Neuroscience **30**(5): 1777–1787.

Ruediger, S., D. Spirig, F. Donato and P. Caroni (2012). "Goal-oriented searching mediated by ventral hippocampus early in trial-and-error learning." Nat Neurosci. **15**(11): 1563-1571.

Rutter, L., F. Carver, T. Holroyd, S. Nadar, J. Mitchell-Francis, J. Apud, D. Weinberger and R. Coppola (2009). "Magnetoencephalographic gamma power reduction in patients with schizophrenia during resting condition." Hum. Brain Mapp. **30**: 3254–3264

Shaw, C. and J. Aggleton (1993). "The effects of fornix and medial prefrontal lesions on delayed non-matching-to-sample by rats." Behavioural Brain Research **54**(1): 91-102.

Siapas, A., E. Lubenov and M. Wilson (2005). "Prefrontal phase locking to hippocampal theta oscillations." Neuron **46**: 141–151.

Siegel, M., M. R. Warden and E. K. Miller (2009). "Phase-dependent neuronal coding of objects in short-term memory." PNAS **106**(50): 21341–21346.

Sigurdsson, T., K. Stark, M. Karayiorgou and J. Gogos (2010). "Impaired hippocampal-prefrontal synchrony in a genetic mouse model of schizophrenia." Nature **464(7289)**: 763-767.

Sigurdsson, T., K. Stark, M. Karayiorgou, J. Gogos and J. Gordon (2010). "Impaired hippocampal-prefrontal synchrony in a genetic mouse model of schizophrenia." Nature **464**(7289): 763-767.

Singer., P. J. U. W. (2010). " Abnormal neural oscillations and synchrony in schizophrenia. ." Nature Reviews Neuroscience **11**: 100-113.

Sloan, H., M. Good and S. Dunnett (2006). "Double dissociation between hippocampal and prefrontal lesions on an operant delayed matching task and a water maze reference memory task." Behavioural Brain Research **171**(1): 116-126.

Sohal, V., F. Zhang, O. Yizhar and K. Deisseroth (2009). "Parvalbumin neurons and gamma rhythms enhance cortical circuit performance." Nature **459(7247)**: 698-702.

Sotres-Bayon, F., D. Sierra-Mercado, E. Pardilla-Delgado and G. Quirk (2012). "Gating of fear in prelimbic cortex by hippocampal and amygdala inputs." Neuron **76**(4): 804-812.

Spellman, T. and J. Gordon (2014). "Synchrony in schizophrenia: a window into circuit-level pathophysiology." Current Opinion in Neurobiology **30**: 17-23.

Spencer, K., P. Nestor, R. Perlmutter, M. Niznikiewicz, M. Klump, M. Frumin, M. Shenton and R. McCarley (2004). "Neural synchrony indexes disordered perception and cognition in schizophrenia." Proc. Natl Acad. Sci. **101(49)**: 17288–17293.

Spencer, K., M. Niznikiewicz, P. Nestor, M. Shenton and R. McCarley (2009). "Left auditory cortex gamma synchronization and auditory hallucination symptoms in schizophrenia." BMC Neurosci. **10**: 85

Spencer, K. M., D. Salisbury, M. Shenton and R. McCarley (2008). "Gamma-band auditory steady-state responses are impaired in first episode psychosis." Biol. Psychiatry **64**: 369–375.

Sreenivasan, K., C. Curtis and M. D'Esposito (2014). "Revisiting the role of persistent neural activity during working memory." Trends Cogn Sci. **18**(2): 82-89.

Stachniak, T., A. Ghosh and S. Sternson (2014). "Chemogenetic Synaptic Silencing of Neural Circuits Localizes a Hypothalamus/Midbrain Pathway for Feeding Behavior." Neuron **82**(4): 797-808.

Stuber, G., D. Sparta, A. Stamatakis, W. van Leeuwen, J. Hardjoprajitno, S. Cho, K. Tye, K. Kempadoo, F. Zhang, K. Deisseroth and A. Bonci (2011). "Excitatory transmission from the amygdala to nucleus accumbens facilitates reward seeking." Nature **475**: 377–380.

Sun, Z., F. Wang, L. Cui, J. Breeze, X. Du, X. Wang, Z. Cong, H. Zhang, B. Li, N. Hong and D. Zhang (2003). "Abnormal anterior cingulum in patients with schizophrenia: a diffusion tensor imaging study." Neuroreport **14(14)**: 1833-1836.

Takita, M., M. Kuramochi, Y. Izaki and M. Ohtomi (2007). "In vivo temporal property of GABAergic neural transmission in collateral feed-forward inhibition system of hippocampal-prefrontal pathway." Brain Res **30**(1150): 69-73.

Thompson, S., L. Masukawa and D. Prince (1985). "Temperature dependence of intrinsic membrance properties and synaptic potentials in hippocampal Ca1 neurons in vitro." The Journal of Neuroscience **5**(3): 817-824.

Thompson, S. M., L. M. Masukawa and D. A. Prince (1985). "Temperature dependence of intrinsic membrane properties and synaptic potentials in hippocampal CA1 neurons in vitro." J Neurosci **5**(3): 817-824.

Tierney, P., E. De´gene` tais, A. Thierry, J. Glowinski and Y. Gioanni (2004). "Influence of the hippocampus on interneurons of the rat prefrontal cortex." European Journal of Neuroscience **20**: 514–524.

Tomassy, G., D. Berger, H. Chen, N. Kasthuri, K. Hayworth, A. Vercelli, H. Seung, J. Lichtman and P. Arlotta (2014). "Distinct profiles of myelin distribution along single axons of pyramidal neurons in the neocortex." Science **344(6181)**: 319-324.

Tye, K., R. Prakash, S. Kim, L. Fenno, L. Grosenick, H. Zarabi, K. Thompson, V. Gradinaru, C. Ramakrishnan and K. Deisseroth (2011). "Amygdala circuitry mediating reversible and bidirectional control of anxiety." Nature **471**: 358–362.

Uranova, N., D. Orlovskaya, O. Vikhreva, I. Zimina, N. Kolomeets, V. Vostrikov and V. Rachmanova (2001). "Electron microscopy of oligodendroglia in severe mental illness." Brain Res Bull. **55(5)**: 597-610.

Uranova, N., V. Vostrikov, D. Orlovskaya and V. Rachmanova (2004). "Oligodendroglial density in the prefrontal cortex in schizophrenia and mood disorders: a study from the Stanley Neuropathology Consortium." Schizophr Res. **67(2-3)**: 269-275.

Venkataraman, A., T. Whitford, C. Westin, P. Golland and M. Kubicki (2012). "Whole brain resting state functional connectivity abnormalities in schizophrenia." Schizophr Res. **139(1-3)**: 7-12.

Vicente, R., L. Golloc, C. Mirassoc, I. Fischerd and G. Pipaa (2008). "Dynamical relaying can yield zero time lag neuronal synchrony despite long conduction delays." Proc Natl Acad Sci **105 no. 44**: 17157–17162.

Vierling-Claassen, D., P. Siekmeier, S. Stufflebeam and N. Kopell (2008). "Modeling GABA alterations in schizophrenia: a link between impaired inhibition and altered gamma and beta range auditory entrainment." J Neurophysiol. **99(5**: :2656-2671.

Vinck, M., F. Battaglia, T. Womelsdorf and C. Pennartz (2012). "Improved measures of phase-coupling between spikes and the Local Field Potential." J Comput Neurosci **33**: 53–75.

Vinck, M., M. van Wingerden, T. Womelsdorf, P. Fries and C. Pennartz (2010). "The pairwise phase consistency: a bias-free measure of rhythmic neuronal synchronization." Neuroimage **55**(1): 112-122.

Volgushev, M., T. R. Vidyasagar, M. Chistiakova and U. T. Eysel (2000). "Synaptic transmission in the neocortex during reversible cooling." Neuroscience **98**(1): 9-22.

Volgushev, M., T. R. Vidyasagar, M. Chistiakova, T. Yousef and U. T. Eysel (2000). "Membrane properties and spike generation in rat visual cortical cells during reversible cooling." J Physiol **522 Pt 1**: 59-76.

von der Malsburg, C. (1981). The correlation theory of brain function. Internal Report 81-2, Dept. of Neurobiology. Göttingen, Germany, Max-Planck-Institute for Biophysical Chemistry.

Wang, G. and J. Cai (2006). "Disconnection of the hippocampal–prefrontal cortical circuits impairs spatial working memory performance in rats." Behavioural Brain Research **175**(2): 329-336.

Wang, G.-W. and J.-X. Cai (2006). "Disconnection of the hippocampal–prefrontal cortical circuits impairs spatial working memory performance in rats." Behavioural Brain Research **175**(2): 329-336.

Wilson, T., O. Hernandez, R. Asherin, P. Teale, M. Reite and D. Rojas (2008). "Cortical gamma generators suggest abnormal auditory circuitry in early-onset psychosis." Cereb Cortex. **18(2)**: 371-378.

Woo, T., J. Miller and D. Lewis (1997). "Schizophrenia and the parvalbumin-containing class of cortical local circuit neurons." Am J Psychiatry. **154(7)**: 1013-1015.

Yamamoto, J., J. Suh, D. Takeuchi and S. Tonegawa (2014). "Successful execution of working memory linked to synchronized high-frequency gamma oscillations." Cell **157**(4): 845-857.

Yizhar, O., L. Fenno, T. Davidson, M. Mogri and K. Deisseroth (2011). "Optogenetics in Neural Systems." Neuron **71**(1): 9-34.

Yong Sang, J., E. Park, I. Kim, S. Park, H. Kim, H. Kim and J. Choice (2007). "The Medial Prefrontal Cortex Is Involved in Spatial Memory Retrieval under Partial-Cue Conditions." The Journal of Neuroscience **27**(49): 13567-13578.

Appendix A

Repeated Cortico-striatal stimulation generates persistent OCD-like Behavior

(Note: This work was performed principally in collaboration with Susanne Ahmari, M.D./Ph.D., at Columbia Univerisity. The establishment of the stimulation protocol was developed, and the behavioral results were obtained, in the labs of Dr. Ahmari and Dr. Rene Hen. The *in vivo* electrophysiological recordings, and the analyses thereof, were performed in the lab of Dr. Joshua Gordon.)

Repeated Cortico-Striatal Stimulation Generates Persistent OCD-Like Behavior

Susanne E. Ahmari *et al.*

Science **340**, 1234 (2013);
DOI: 10.1126/science.1234733

Collectively, these results demonstrate that (i) lethal synergy of influenza virus and bacterial coinfection can result from loss of tolerance to infection-induced tissue damage, (ii) morbidity and mortality of coinfection can be independent of pathogen burden or excessive inflammatory response, and (iii) promoting tissue repair can, in principle, rescue coinfected animals from morbidity and mortality, even without affecting pathogen burden. Finally, our influenza–*L. pneumophila* coinfection model demonstrates the distinction between resistance and tolerance as separate host defense strategies that can both contribute to morbidity and mortality of infectious disease.

References and Notes

1. L. Råberg, D. Sim, A. F. Read, *Science* **318**, 812 (2007).
2. L. Råberg, A. L. Graham, A. F. Read, *Philos. Trans. R. Soc. London Ser. B Biol. Sci.* **364**, 37 (2009).
3. D. S. Schneider, J. S. Ayres, *Nat. Rev. Immunol.* **8**, 889 (2008).
4. R. Medzhitov, D. S. Schneider, M. P. Soares, *Science* **335**, 936 (2012).
5. C. Beadling, M. K. Slifka, *Curr. Opin. Infect. Dis.* **17**, 185 (2004).
6. J. A. McCullers, *Clin. Microbiol. Rev.* **19**, 571 (2006).
7. J. M. Hament, J. L. Kimpen, A. Fleer, T. F. Wolfs, *FEMS Immunol. Med. Microbiol.* **26**, 189 (1999).
8. V. T. Peltola, J. A. McCullers, *Pediatr. Infect. Dis. J.* **23** (suppl.), S87 (2004).
9. M. Iannuzzi *et al.*, *J. Med. Case Rep.* **5**, 520 (2011).
10. A. Shahangian *et al.*, *J. Clin. Invest.* **119**, 1910 (2009).
11. A. R. Iverson *et al.*, *J. Infect. Dis.* **203**, 880 (2011).
12. K. Sun, D. W. Metzger, *Nat. Med.* **14**, 558 (2008).
13. A. Didierlaurent *et al.*, *J. Exp. Med.* **205**, 323 (2008).
14. K. H. Berger, R. R. Isberg, *Mol. Microbiol.* **7**, 7 (1993).
15. D. B. Mendel *et al.*, *Antimicrob. Agents Chemother.* **42**, 640 (1998).
16. T. Ichinohe, *Expert Rev. Vaccines* **9**, 1315 (2010).
17. A. García-Sastre, C. A. Biron, *Science* **312**, 879 (2006).
18. T. Ren, D. S. Zamboni, C. R. Roy, W. F. Dietrich, R. E. Vance, *PLoS Pathog.* **2**, e18 (2006).
19. A. B. Molofsky *et al.*, *J. Exp. Med.* **203**, 1093 (2006).
20. D. S. Zamboni *et al.*, *Nat. Immunol.* **7**, 318 (2006).
21. K. A. Archer, C. R. Roy, *Infect. Immun.* **74**, 3325 (2006).
22. R. Spõrri, N. Joller, U. Albers, H. Hilbi, A. Oxenius, *J. Immunol.* **176**, 6162 (2006).
23. N. L. La Gruta, K. Kedzierska, J. Stambas, P. C. Doherty, *Immunol. Cell Biol.* **85**, 85 (2007).
24. J. S. M. Peiris, K. P. Y. Hui, H.-L. Yen, *Curr. Opin. Immunol.* **22**, 475 (2010).
25. N. Schmitz, M. Kurrer, M. F. Bachmann, M. Kopf, *J. Virol.* **79**, 6441 (2005).
26. T. Decker, M. Müller, S. Stockinger, *Nat. Rev. Immunol.* **5**, 675 (2005).
27. M. F. Fontana, S. Shin, R. E. Vance, *Infect. Immun.* **80**, 3570 (2012).
28. D. K. Bhalla, *J. Toxicol. Environ. Health B Crit. Rev.* **2**, 31 (1999).
29. L. M. Crosby, C. M. Waters, *Am. J. Physiol. Lung Cell. Mol. Physiol.* **298**, L715 (2010).
30. H. R. Wong, J. R. Wispé, *Am. J. Physiol.* **273**, L1 (1997).
31. L. A. Monticelli *et al.*, *Nat. Immunol.* **12**, 1045 (2011).

Acknowledgments: We thank S. Holley and C. Annicelli for technical assistance; T. Ichinohe, M. Linehan, and A. Iwasaki for viral strains and advice; T. Ren, M. Fontana, R. Vance, K. Archer, S. Shin, and C. Roy for *L. pneumophila* strains and advice; M. Gillum for assistance with experiments; and M. Mueller and C. Lassnig for mouse infection infrastructure. The data presented in the manuscript are tabulated in the main paper and in the supplementary materials. This work was supported by the Howard Hughes Medical Institute (R.M.), NIH grants R01 046688 and AI R01 055502 (R.M.), the Ellison Foundation (R.M.), the New England Regional Center of Excellence (R.M.), and FWF (Austrian Science Fund) grant P25235-B13 (A.M.J.). A.M.J. was a Berger Foundation fellow of the Damon Runyon Cancer Research Foundation. The authors have no conflicts of interest.

Supplementary Materials

www.sciencemag.org/cgi/content/full/science.1233632/DC1
Supplementary Text
Figs. S1 to S6
References (*32*, *33*)

4 December 2012; accepted 15 April 2013
Published online 25 April 2013;
10.1126/science.1233632

Repeated Cortico-Striatal Stimulation Generates Persistent OCD-Like Behavior

Susanne E. Ahmari,[1,2,3,4]* Timothy Spellman,[5] Neria L. Douglass,[1,2] Mazen A. Kheirbek,[1,2] H. Blair Simpson,[1,3,4] Karl Deisseroth,[6] Joshua A. Gordon,[1,2] René Hen[1,2]

Although cortico-striato-thalamo-cortical (CSTC) circuit dysregulation is correlated with obsessive compulsive disorder (OCD), causation cannot be tested in humans. We used optogenetics in mice to simulate CSTC hyperactivation observed in OCD patients. Whereas acute orbitofrontal cortex (OFC)–ventromedial striatum (VMS) stimulation did not produce repetitive behaviors, repeated hyperactivation over multiple days generated a progressive increase in grooming, a mouse behavior related to OCD. Increased grooming persisted for 2 weeks after stimulation cessation. The grooming increase was temporally coupled with a progressive increase in light-evoked firing of postsynaptic VMS cells. Both increased grooming and evoked firing were reversed by chronic fluoxetine, a first-line OCD treatment. Brief but repeated episodes of abnormal circuit activity may thus set the stage for the development of persistent psychopathology.

OCD is characterized by intrusive distressing thoughts (obsessions) and/or repetitive mental or behavioral acts (compulsions) and is a leading cause of illness-related disability (*1*, *2*). Although the pathophysiology underlying OCD is unclear, multiple lines of evidence implicate dysregulation within cortico-striato-thalamo-cortical (CSTC) circuits (*3*–*6*). Specifically, functional imaging studies suggest that hyperactivity in orbitofrontal cortex (OFC) and ventromedial striatum (VMS) is associated with OCD pathology (*5*, *7*, *8*). Furthermore, successful treatments are associated with reductions in hyperactivity (*9*, *10*). However, it is not known if OFC-VMS hyperactivity can directly cause OCD symptoms, because increased activity could represent adaptive, homeostatic, or unrelated processes compensating for other primary abnormalities. We therefore used an optogenetic strategy to directly test whether hyperstimulation of glutamatergic OFC-VMS projections leads to OCD-like behaviors in mice.

A Cre-inducible adenovirus-associated vector (AAV) carrying the gene encoding channelrhodopsin (ChR2) fused to enhanced yellow fluorescent protein (EYFP) [pAAV-Ef1a-DIO-ChR2 (H134R)-EYFP; referred to as DIO-ChR2] (*11*) was stereotactically injected into OFC of EMX-Cre transgenic mice to ensure specific ChR2 expression in cortical glutamatergic neurons (Fig. 1A) (*12*). Cortical Cre expression led to sustained expression of ChR2-EYFP (Fig. 1B). Unilateral 473-nm stimulation through chronic fiber-optic implants in OFC yielded lateralized increased activation of the immediate early gene c-*fos* ($P < 0.009$) (Fig. 1, C and D), which demonstrated in vivo cellular activation by laser stimulation. Two weeks postinjection, EYFP staining was seen in OFC cell bodies and axons projecting to VMS (Fig. 1E), which indicated targeting of OFC-VMS projections. In vitro recordings in cortico-striatal slices demonstrated VMS field responses after 473-nm laser stimulation of OFC axon terminals in striatum (Fig. 1F). To verify adequate stimulation of ChR2-expressing OFC-VMS terminals in vivo, we implanted stereo opto-electrodes (optrodes) into VMS that permit combined fiber-optic stimulation and 32-channel simultaneous recording of multiple single units (Fig. 1G). In awake behaving mice, in vivo recordings demonstrated robust VMS field responses after 473-nm laser stimulation of OFC axon terminals in striatum (Fig. 1, H and I), which showed

[1]Department of Psychiatry, Columbia University College of Physicians and Surgeons, New York, NY 10032, USA. [2]Division of Integrative Neuroscience, New York State Psychiatric Institute, New York, NY 10032, USA. [3]Division of Clinical Therapeutics, New York State Psychiatric Institute, New York, NY 10032, USA. [4]Anxiety Disorders Clinic and OCD Research Program, New York State Psychiatric Institute, New York, NY 10032, USA. [5]Department of Physiology, Columbia University College of Physicians and Surgeons, New York, NY 10032, USA. [6]Departments of Psychiatry and Bioengineering, Stanford University School of Medicine, Stanford, CA 94305, USA.

*Corresponding author. E-mail: sea2103@columbia.edu

feasibility of activation of specific cortical-VMS projections.

Because patients with OCD have hyperactivity in OFC-striatal circuits (*3*–*6*), we predicted that direct elevation of OFC-VMS activity would lead to increases in OCD-related behaviors including grooming, anxiety, and prepulse inhibition (PPI) deficits (*13*). We injected DIO-ChR2 into the left OFC of EMX-Cre mice and implanted fiber-optic probes unilaterally in left VMS (Fig. 2A). After waiting 3 to 4 weeks for surgical recovery and stable viral expression, we habituated mice to the open field and fiber-optic stimulation apparatus. We then repeatedly elevated activity in OFC-VMS projections by stimulating for 5 min at 10 Hz for five consecutive days (10 ms, 1 to 5 mW) (*14*). Grooming behavior was recorded with digital video and scored by blind raters for 5 min before (Pre), during (Stim), and after (Post) stimulation (Fig. 2B). Whereas acute OFC-VMS stimulation did not produce grooming, a small but significant progressive increase in grooming time was noted during the prestimulation period on consecutive days (Fig. 2C) [repeated measures analysis of variance (ANOVA), main effect: $P < 0.048$; $F = 4.43$; Fisher's protected least significant difference (PLSD): for day 3, $P < 0.03$; for day 5, $P < 0.047$]. Because the prestimulation measurement on days 2 to 5 served as a 24-hour time stamp for effects of stimulation the day before, this suggested that repeated stimulation led to chronic circuit changes that ultimately resulted in sustained, stimulation-independent OCD-like behavior. Although it is possible that stress from handling contributed to the grooming increase in the prestimulation period, stress was minimized by habituation to fiber-optic tethering daily for a week before data collection and was identical for controls and ChR2+ mice. To resolve the time-course of the grooming increase, we examined a new cohort an hour after stimulation ($Groom_{1\ hour\ post}$) (Fig. 2D). We observed a dramatic progressive increase in grooming over consecutive days using this measure (main effect: $P < 0.02$; $F = 7.32$) (Fig. 2E). Although total grooming time increased, there was not a significant increase in stereotyped syntactic grooming chains in ChR2+ animals on day 5 of stimulation (table S1). No differences in grooming time were observed between controls and ChR2+ animals on day 1 of stimulation, which indicated that ChR2 expression without laser stimulation did not lead to an increase in grooming. Notably, increased grooming persisted even

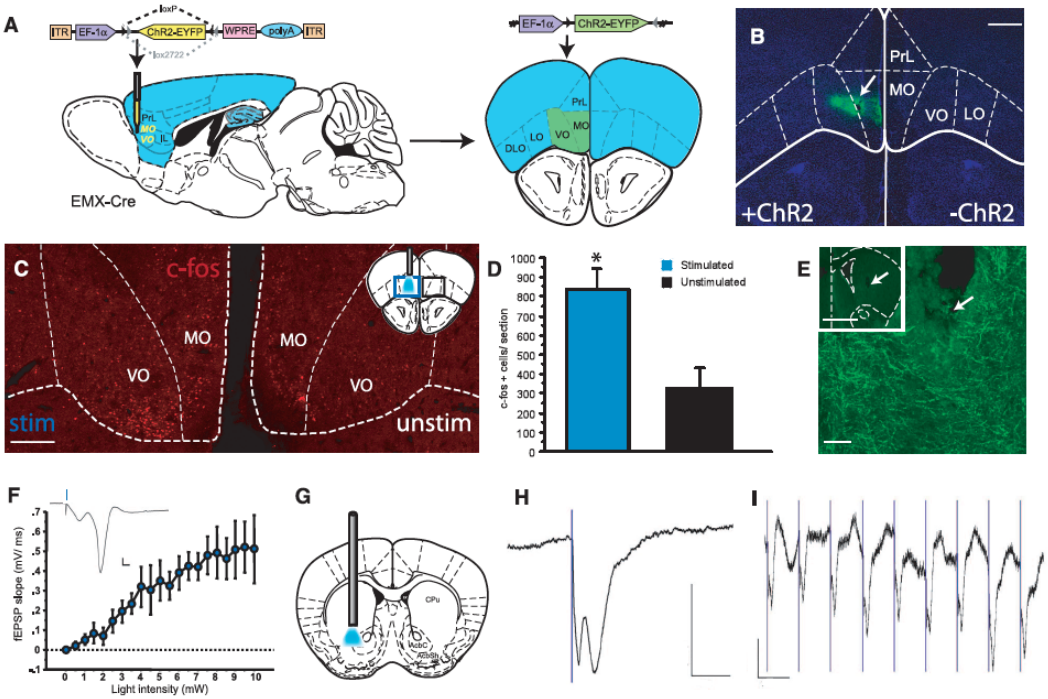

Fig. 1. Injection of ChR2-EYFP AAV into OFC leads to functional ChR2 expression in projections from OFC to VMS. **(A)** Schematic diagram of DIO-ChR2 injections. (Left) Reference sagittal section indicates injection position in ventromedial OFC (VO/MO) of EMX-Cre mice (2.6 mm AP, 1.7 mm DV, 0.5 mm ML). Blue shading: Cre expression in cortex and hippocampus. (Right) Cre-expressing glutamatergic cells in OFC irreversibly invert the ChR2-EYFP open reading frame, which leads to cell type–specific ChR2-EYFP expression (green shading). EF-1α, elongation factor 1α; ITR, inverted terminal repeat; WPRE, woodchuck hepatitis virus posttranslational regulatory element; DLO, dorsolateral orbitofrontal cortex; LO, lateral orbitofrontal cortex; PrL, prelimbic cortex. **(B)** Confocal image of YFP-immunostaining shows unilateral ChR2 expression at OFC injection site. Scale bar, 500 μm. **(C)** c-Fos immunostaining demonstrates 473-nm light–induced activation of OFC in awake behaving mice through chronic fiber-optic implant. (Inset) Reference coronal section. Blue square, stimulated; black, unstimulated. **(D)** Quantification of c-Fos–positive cells in stimulated versus unstimulated OFC ($P < 0.009$) ($n = 4$ controls; 4 ChR2 mice; five sections each). **(E)** Targeting of OFC-VMS projections evidenced by axonal YFP staining under fiber-optic implant site (arrow). Scale bar, 100 μm. (Inset) Low magnification. Scale bar, 500 μm. **(F)** Extracellular field recordings from striatal slices. Increased population spike amplitude with increasing laser power. (Inset) Individual population spike after 0.1-ms light pulse (3 mW); calibration bars: vertical 0.5 mV, horizontal 1 ms. $n = 4$ slices from each of three animals. **(G)** Schematic diagram of stereo-optrode implant in VMS. (Stereotaxic coordinates: 0.98 mm AP, 3.5 mm DV, 1.25 mm ML). CPu, caudate putamen; AcbC, accumbens core; AcbSh, accumbens shell. **(H)** In vivo recordings in awake behaving animals show field responses to 473-nm stimulation of VMS terminals. Mean response to 20 flashes delivered at 0.5 Hz. Calibration bar: vertical 0.5 mV, horizontal 20 ms. **(I)** Raw responses to train of 10 flashes at 10 Hz. Calibration bar: vertical 0.5 mV, horizontal 100 ms.

in the absence of stimulation up to 2 weeks later ($P < 0.03$) (Fig. 2F).

Acute OFC-VMS stimulation led immediately to a large but transient increase in locomotion compared with controls; no differences were observed pre- or poststimulation (fig. S1A). To ensure that increased grooming was not simply a consequence of increased locomotion, we injected DIO-ChR2 and implanted fiber optics in motor cortex (M2) of EMX-Cre mice (fig. S1B). The 5-day stimulation paradigm described above led to increased locomotion (fig. S1C) but not to increased grooming (fig. S1D), which suggested that increased grooming was not simply a side effect of overall increased activity. To determine the specificity of OFC-VMS pathway hyperactivation in induction of persistent grooming, we injected AAV-ChR2 into infralimbic and prelimbic cortex (IL/PrL) (fig. S2A) and stimulated IL/PrL–VMS projections using our 5-day stimulation paradigm. Repeated stimulation of IL/PrL–VMS projections did not lead to a progressive increase in grooming behavior (fig. S2, B to D).

Other OCD-associated behavioral measures were tested after completion of the 5-day stimulation paradigm. No differences were seen in PPI (*13*) or anxiety levels (in open field and elevated plus maze) compared with testing before stimulation (fig. S3); in addition, no changes in open field anxiety were observed during acute stimulation (fig. S4). Together, these results suggest that repeated stimulation of OFC-VMS projections led to specific induction of repetitive behavior.

We next examined electrophysiologic changes correlated with the progressive grooming increase using VMS stereo-optrodes (Fig. 3A and fig. S5). In awake behaving mice, recordings of multiple single units in the VMS were obtained during the 15-min stimulation protocol and 1 hour post grooming assessment (Fig. 3B). Light-evoked responses were observed in individual units in response to 10 Hz stimuli (Stim) or 0.1 Hz probe pulses (used to measure light-evoked activity during pre-, post-, and 1 hour poststimulation) over 5 days of repeated stimulation. Cells displayed a range of responses to light pulses, including activation (Fig. 3C), suppression (Fig. 3D), and no effect (Fig. 3E); we therefore used each cell's stimulation-induced change in firing rate (expressed as a *Z*-score; see supplementary methods) to assess responsiveness to afferent stimulation. Across 5 days of stimulation, mean responses increased both during stimulation and 1 hour poststimulation (Fig. 3F; $R = 0.21$ and 0.28; $P < 0.002$ and < 0.001, respectively). *Z*-scores were greater on day 5 than on day 1, which indicated increased evoked firing (at 10 Hz: $P < 0.02$; at 0.1 Hz: $P < 0.004$). Thus, repeated hyperstimulation led to a marked progressive increase in light-evoked firing paralleling the increase in repetitive behavior.

Finally, we determined whether a medication regimen used to treat OCD would reverse the increases in repetitive behavior and evoked VMS activity. After 7-day grooming induction, we initiated fluoxetine treatment (18 mg/kg body weight per day) while continuing daily stimulation (Fig. 4A). Fluoxetine was chosen because serotonin reuptake inhibitors (SRIs) are the only proven monotherapy for OCD (*15*). Although there was no effect of fluoxetine after 1 week, 2 weeks of treatment led to a reversal of grooming behavior to control levels (Fig. 4B) (main effect: $P < 0.009$, $F = 9.53$; Fisher's PLSD: baseline versus week 2,

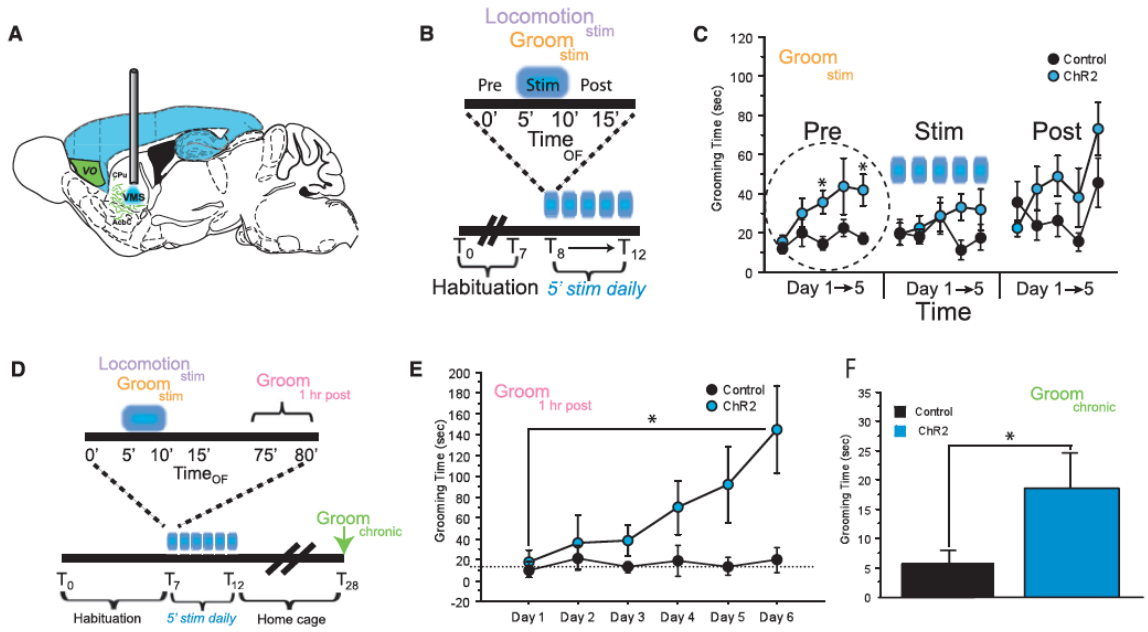

Fig. 2. Brief repeated hyperstimulation of OFC-VMS projections leads to progressively increased grooming behavior. (**A**) Localization of viral injection and fiber-optic implant. ChR2 (green) is expressed in ventromedial OFC. Fiber-optic implant is placed into VMS to stimulate ChR2 in axon terminals projecting from OFC. (**B**) Time line for chronic stimulation of OFC-VMS projections. After habituation to the tethering procedure for 7 days (T_1 to T_7), mice underwent the stimulation protocol. $Time_{OF}$ = Time in open field. (**C**) Grooming behavior over five consecutive days of stimulation. Total time grooming was assessed for 5 min before (Pre), during (Stim), and after stimulation (Post) for five consecutive days. Data are grouped into Pre, Stim, and Post categories for days 1 to 5 to facilitate examination of changes in behavior over time. Stimulation (10 Hz) led to a significant increase in grooming time in ChR2 animals before stimulation (Pre) (main effect: $P < 0.048$, $F = 4.43$; post hoc test: day 3, $^*P < 0.03$; day 5, $^*P < 0.047$; $n = 8$ ChR2 mice, 7 controls). (**D**) Time line for examination of chronic impact of stimulation. (**E**) After 6 days of stimulation, ChR2+ animals had significantly elevated grooming during $Groom_{1\ hour\ post}$ (main effect $^*P < 0.02$; $F = 7.32$; n count: ChR2 = 6; control = 5). (**F**) Two weeks after repeated stimulation (T_{28}), ChR2+ animals continued to demonstrate significantly increased grooming ($Groom_{chronic}$ $^*P < 0.03$; one-tailed t test), although absolute grooming time was decreased compared with times immediately after stimulation paradigm (T_{12}).

$P < 0.003$). This delayed response is consistent with the delayed onset of effective SRI treatment in OCD patients. We also repeated this experiment using a vehicle control group (Fig. 4C). Again, 2 weeks of fluoxetine led to reversal of induced grooming (Fig. 4D). Moreover, in a separate cohort of stereo-optrode–implanted animals, the increase in light-evoked activity induced by repeated 10 Hz stimulation was normalized after chronic fluoxetine (Fig. 4, E and F).

Repeated hyperactivation of OFC-VMS projections generates a progressive increase in grooming, temporally linked to a cumulative increase in VMS light-evoked firing. Acute stimulation of the OFC-VMS pathway was not sufficient to produce OCD-relevant excessive grooming (*3*, *16*–*18*). The behavioral change was persistent, becoming stimulation-independent within 6 days. Although classic theories suggest that abnormal repetitive behaviors, including OCD symptoms, directly result from hyperactivity in CSTC loops (*19*–*21*), causation has been difficult to prove. Though genetic and pharmacologic manipulations of norepinephrine and dopamine can lead to transient increases in repetitive behaviors (*22*), the interventions were not limited to specific circuits, and associated electrophysiologic changes were observed in multiple brain regions. Our optogenetic system permits activation of specific cortico-striatal circuits and genetic definition of the activated cell-type as cortical glutamatergic projection neurons.

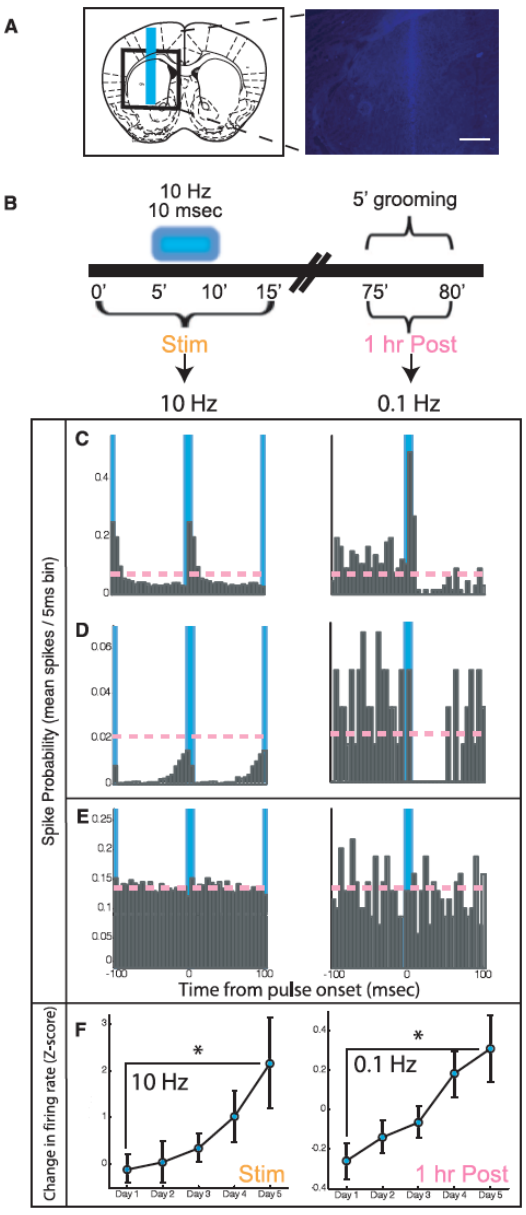

Fig. 3. Repeated daily stimulation of OFC-VMS projections leads to increased evoked firing. (A) (Left) Schematic diagram of stereo-optrode implant site. (Right) Placement visualized via implanting a stereo-optrode dipped in Hoechst stain (1:1000). Scale bar, 500 μm. **(B)** Stimulation protocol used for in vivo recording. **(C to E)** Representative peristimulus spike histograms (5-ms time bins) of three neurons recorded during 10 Hz stimulation (left) and 0.1 Hz probe pulses (1 hour poststimulation on right). Baseline spontaneous firing rate for each cell is shown as pink dashed line. Cells exhibited varied stimulus responsiveness, including evoked activation (C), evoked suppression (D), and no response (E). **(F)** Light-evoked firing (measured by peristimulus *z*-scores) across 5 days of stimulation both during 10 Hz stimulation (Stim) and during 0.1 Hz probe pulses 1 hour after stimulation (1 hour post) (*$P < 0.021$ and $P < 0.004$). Negative *Z*-scores for 0.1 Hz on days 1 and 2 indicate net suppression of evoked firing rate during $\text{Groom}_{1\ \text{hour post}}$ after the first two epochs of 10 Hz stimulation.

OCD is a heterogeneous disorder. Our study therefore may have greater relevance for particular OCD subtypes. For example, dimensional models of OCD have been proposed in which different types of obsessions and compulsions are associated with different circuits (*29*, *30*). Because our results suggest that repeated stimulation of OFC-VMS projections led to specific induction of repetitive grooming, our model may be of particular importance for OCD patients with predominant contamination concerns.

Our findings yield new insight into how psychopathology could develop. Only 5 min of stimulation per day was sufficient to lead to sustained significant behavioral effects. This raises the possibility that pathological changes, including compulsions in OCD, may result from small but repeated bursts of abnormal neuronal activity and also offers suggestions for new treatment approaches or refinements of existing therapies for disorders characterized by repetitive behaviors. For example, our data are consistent with recent clinical studies demonstrating efficacy of ventral capsule–ventral striatum deep brain stimulation in OCD (*31*, *32*), which is thought to act via inhibition of OFC hyperactivity. Optogenetic approaches could be used to dissect circuit mechanisms underlying deep brain stimulation and other treatments, with a goal of identifying new treatment targets.

Our in vivo electrophysiology data suggest a circuit-based mechanism for establishment of repetitive behaviors. Repeated hyperstimulation led to a marked progressive increase in light-evoked firing paralleling the increase in grooming, suggesting plasticity at OFC-VMS synapses that builds over consecutive days. We speculate that brief episodes of light-induced activity lead to long-lasting changes that prime OFC-VMS synapses, decreasing the activation threshold during subsequent bouts of stimulation. In turn, increased activity at OFC-VMS synapses may transmit information through the CSTC circuit (*23*–*25*) and lead to multiple downstream events that ultimately reinforce repetitive behaviors, including (i) plasticity in downstream structures such as thalamus and prefrontal cortex (*26*), and (ii) increased motivational saliency mediated by the ventral tegmental area (*22*). This mechanism would be consistent with the observed fluoxetine effects, since selective SRIs have been shown to reduce primary reward processing (*27*, *28*).

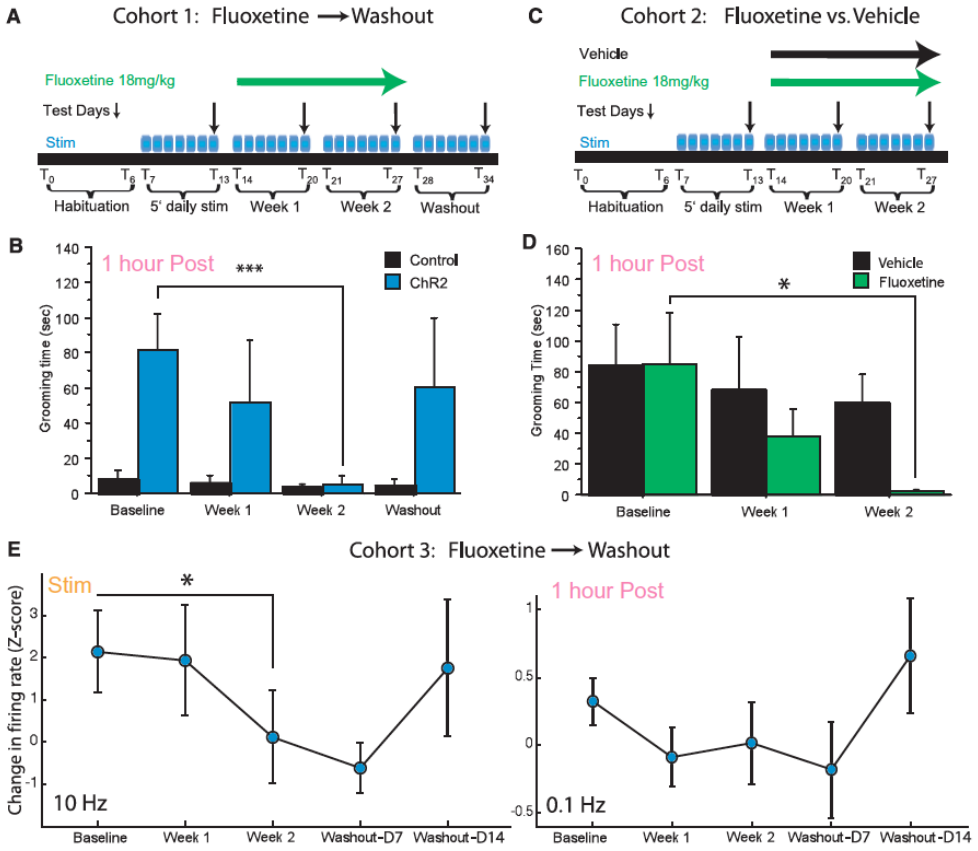

Fig. 4. Perseverative grooming and elevated evoked firing rate are resolved by chronic, but not acute, fluoxetine treatment. (**A**) Experimental time line for fluoxetine wash-out experiment. (**B**) Two weeks of fluoxetine treatment reduced grooming to level of controls. Main effect: $P < 0.009$; $F = 9.53$; Fisher's PLSD: baseline versus week 2, $^{***}P < 0.003$. Increased grooming was reestablished after a 1-week fluoxetine wash-out. Main effect: $P < 0.09$; $F = 3.58$. n values: ChR2^{+} mice = 8; controls = 7. (**C**) Experimental time line for fluoxetine versus vehicle experiment. (**D**) Two weeks of fluoxetine treatment reduced grooming to levels of vehicle-treated animals. Main effect: $P < 0.14$; $F = 2.59$; Fisher's PLSD: baseline versus week 2, $^{*}P < 0.04$. Fluoxetine: $n = 7$; vehicle: $n = 6$. (**E**) (Left) In stereotaxic optrode–implanted animals, peristimulus Z-scores for 10 Hz stimuli normalized after 2 weeks of fluoxetine ($P < 0.028$); after 2-week wash-out, Z-scores returned to pretreatment levels. (Right) Peristimulus Z-scores for 0.1 Hz probe pulses showed a nonsignificant decrease after fluoxetine treatment, which returned to pretreatment levels after wash-out.

References and Notes

1. C. J. L. Murray, A. D. Lopez, *The Global Burden of Disease: A Comprehensive Assessment of Mortality and Disability from Diseases, Injuries, and Risk Factors in 1990 and Projected to 2020*, Global burden of disease and injury series; vol. 1 (Harvard School of Public Health, Harvard Univ. Press, Cambridge, MA, 1996).
2. R. C. Kessler *et al.*, *Arch. Gen. Psychiatry* **62**, 593 (2005).
3. J. T. Ting, G. Feng, *Curr. Opin. Neurobiol.* **21**, 842 (2011).
4. R. Marsh, T. V. Maia, B. S. Peterson, *Am. J. Psychiatry* **166**, 664 (2009).
5. M. R. Milad, S. L. Rauch, *Trends Cogn. Sci.* **16**, 43 (2012).
6. C. Pittenger, M. H. Bloch, K. Williams, *Pharmacol. Ther.* **132**, 314 (2011).
7. S. Saxena, R. G. Bota, A. L. Brody, *Semin. Clin. Neuropsychiatry* **6**, 82 (2001).
8. J. Y. Rotge *et al.*, *Biol. Psychiatry* **65**, 75 (2009).
9. S. L. Rauch, C. R. Savage, N. M. Alpert, A. J. Fischman, M. A. Jenike, *Biol. Psychiatry* **42**, 446 (1997).
10. J. L. Abelson *et al.*, *Biol. Psychiatry* **57**, 510 (2005).
11. H. C. Tsai *et al.*, *Science* **324**, 1080 (2009).
12. J. A. Gorski *et al.*, *J. Neurosci.* **22**, 6309 (2002).
13. S. E. Ahmari, V. B. Risbrough, M. A. Geyer, H. B. Simpson, *Neuropsychopharmacology* **37**, 1216 (2012).
14. J. Mattis *et al.*, *Nat. Methods* **9**, 159 (2012).
15. L. M. Koran, G. L. Hanna, E. Hollander, G. Nestadt, H. B. Simpson; American Psychiatric Association, *Am. J. Psychiatry* **164** (suppl.), 5 (2007).
16. S. V. Shmelkov *et al.*, *Nat. Med.* **16**, 598, 1p, 602 (2010).
17. J. M. Welch *et al.*, *Nature* **448**, 894 (2007).
18. S. K. Chen *et al.*, *Cell* **141**, 775 (2010).
19. T. R. Insel, J. T. Winslow, *Psychiatr. Clin. North Am.* **15**, 813 (1992).
20. D. R. Rosenberg, M. S. Keshavan, *Biol. Psychiatry* **43**, 623 (1998).
21. L. R. Baxter Jr. *et al.*, *Am. J. Psychiatry* **145**, 1560 (1988).
22. K. Dzirasa *et al.*, *J. Neurosci.* **30**, 6387 (2010).
23. S. K. Bourne, C. A. Eckhardt, S. A. Sheth, E. N. Eskandar, *Front Integr Neurosci* **6**, 29 (2012).
24. A. M. Graybiel, S. L. Rauch, *Neuron* **28**, 343 (2000).
25. S. N. Haber, S. L. Rauch, *Neuropsychopharmacology* **35**, 1 (2010).
26. E. G. Antzoulatos, E. K. Miller, *Neuron* **71**, 243 (2011).
27. B. Abler, G. Grön, A. Hartmann, C. Metzger, M. Walter, *J. Neurosci.* **32**, 1329 (2012).
28. C. McCabe, Z. Mishor, P. J. Cowen, C. J. Harmer, *Biol. Psychiatry* **67**, 439 (2010).
29. D. Mataix-Cols *et al.*, *Arch. Gen. Psychiatry* **61**, 564 (2004).
30. J. F. Leckman *et al.*, *Depress. Anxiety* **27**, 507 (2010).
31. B. D. Greenberg *et al.*, *Mol. Psychiatry* **15**, 64 (2010).
32. P. P. de Koning, M. Figee, P. van den Munckhof, P. R. Schuurman, D. Denys, *Curr. Psychiatry Rep.* **13**, 274 (2011).

Acknowledgments: We thank H. B. Simpson and C. Kellendonk for critical discussions and reading of the manuscript and D. Flicker and M. Cloidt for behavioral scoring assistance. S.E.A. is supported by National Institute of Mental Health (NIMH) K08MH087718; the Louis V. Gerstner, Jr., Scholars Program; the Irving Institute for Clinical and Translational Research; the Gray Matters Foundation; the Leon Levy Foundation; and a Brain and Behavior Research Foundation NARSAD Young Investigator Award. M.A.K. is supported by